Dual-Stage Servo Control and Active Vibration Compensation in Magnetic Hard Disk Drives

by

Yunfeng Li

B.S. (Beijing University of Aeronautics and Astronautics) 1992
M.S. (Beijing University of Aeronautics and Astronautics) 1995

A dissertation submitted in partial satisfaction of the
requirements for the degree of
Doctor of Philosophy

in

Engineering - Mechanical Engineering

in the

GRADUATE DIVISION
of the
UNIVERSITY OF CALIFORNIA, BERKELEY

Committee in charge:
Professor Roberto Horowitz, Chair
Professor Masayoshi Tomizuka
Professor Ronald S. Fearing

Fall 2003

The dissertation of Yunfeng Li is approved:

Chair Date

Date

Date

University of California, Berkeley

Fall 2003

Dual-Stage Servo Control and Active Vibration Compensation in Magnetic Hard Disk Drives

by

Yunfeng Li

Abstract

Dual-Stage Servo Control and Active Vibration Compensation in Magnetic Hard Disk Drives

by

Yunfeng Li

Doctor of Philosophy in Engineering - Mechanical Engineering

University of California, Berkeley

Professor Roberto Horowitz, Chair

In order to sustain the continuing increase in storage density in magnetic hard disk drives (HDD), high bandwidth dual-stage actuator servo systems have been developed to improve the precision of read/write head positioning control. In this dissertation, robust and adaptive controller design methodologies and algorithms are developed for PZT-actuated suspension and MEMS microactuator based dual-stage servo systems. Active vibration control techniques using dual-stage multi-sensing servo systems to compensate for high-frequency structural vibrations are proposed.

A coupled MIMO plant model of a PZT-actuated suspension dual-stage actuator is identified using frequency response modal testing. A structured uncertainty model is established to represent both parametric uncertainty and unmodeled dynamics for robust control design and analysis. Dual-stage controllers are designed using a decoupled single-

input single-output (SISO) frequency shaping design technique and multi-variable robust controller design technique μ-synthesis. Experimental results are presented and compared.

An active vibration damping control scheme of using one PZT element as a vibration sensor and the other one as an actuator is proposed to damp the resonance modes of the PZT-actuated suspension dual-stage actuator. Vibration damping controller design using Kalman filter based state feedback control is described. Experimental results are presented demonstrating the effectiveness of the proposed control scheme in suppressing airflow excited structural vibrations.

For the controller design of a MEMS microactuator based dual-stage servo system, a decoupled design structure with microactuator inner-loop damping and a design methodology by discrete-time pole placement are proposed. A self-tuning control scheme is developed to compensate for the variations in the microactuator's resonance mode. An adaptive feedforward control technique is also developed for active vibration compensation using MEMS microactuator dual-stage servo systems. Simulation results are presented to verify the proposed control schemes.

Professor Roberto Horowitz
Dissertation Committee Chair

To my family

Contents

List of Figures

List of Tables

Acknowledgments

First and foremost, I express my sincerest gratitude to my research advisor, Professor Horowitz. His guidance, insights, encouragements, and support throughout my graduate career is essential to the construction of this dissertation. I would also like to express my thanks and appreciation to other committee members, Professor Tomizuka and Professor Fearing, for their time and valuable comments and suggestions while reviewing my dissertation.

My thanks also go to lab fellow students, Tsung-Lin Chen, Jongeun Choi, Carlo Cloet, Xinghui Huang, Stanley Kon, Martin Krucinski, Si-Hyung Lim, Kenn Oldham, Sungsu Park, Rene Sanchez, and Xiaotian Sun, and visiting scholars, Masahito Kobayashi and Hidehiko Numasato from Hitachi, Federico Marcassa and Professor Oboe from University of Padova, Professor Morales from University of Central Venezuela, and Keitaro Ohno from Fujitsu Laboratory. They all have helped me on many occasions both in my study and research. I have learned so much from them. They also made the lab a joyful and colorful place to work. Special thanks go to Masahito for teaching me the basics of disk drive servo control and implementations when I just joined the lab, Federico and Professor Oboe for their valuable contributions and collaborative research on active damping control, and Xinghui and Kenn for proofreading and editing the manuscript of the dissertation.

In addition, I would like to thank Alexei Sacks from Seagate, Robert Evans from Hutchinson Technology Inc., Edmund Fanslau from Read-Rite, and the other industrial participants in the Information Storage Industry Consortium (INSIC) servo team for their valuable feedback, suggestions, and help to my research. I would also like to thank Hany

Gross, Brian Thornton, and Professor Bogy at the Computer Mechanics Laboratory (CML) for their help with the experimental setup. This research is supported partly by CML, and partly by INSIC.

Finally, I thank my parents and my wife for their caring, love, understanding and support. Special thanks also go to my wife Hua for her help with some drawings and proofreading of the dissertation.

Chapter 1

Introduction

Since the first hard disk drive (HDD) was invented in the 1950s by IBM, disk drives' data storage areal density has been following Moore's law, doubling roughly every 18 months [1] [61]. Higher areal density requires more precise positioning control of the read/write head. Advanced servo technologies using dual-stage actuators and auxiliary sensors have been developed in recent years to achieve this objective. This dissertation focuses on controller design for dual-stage actuator servo systems and active vibration suppression control using auxiliary vibration sensors. In this chapter, an introduction of disk drive servo mechanics and servo control system is presented. Advanced dual-stage, multi-sensing servo systems are introduced. Previous research, the motivation and objectives of this dissertation are presented. Finally, the outline of the dissertation is listed.

1.1 Disk Drive Servo Control

1.1.1 Disk Drive Structure and Servo Mechanics

A disk drive stores data as magnetic patterns on disk media, which consists of a thin layer of magnetic materials coated on an aluminum or glass substrate. A data bit's value of one or zero is represented by the presence or absence of a magnetic transition (magnetization reverse), which can be set (written) or detected (read) by the write and read transducers as they move over it, as shown in Fig. 1.1. The write transducer is a thin-film coil which magnetizes the polarity of the media when electrical current passes through it. The read transducer is a magnetoresistive sensor, which changes its resistance with the change in the magnetic field.

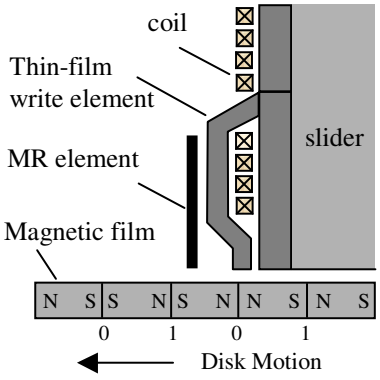

Figure 1.1: A diagram of read/write transducer and media.

Fig. 1.2 shows a schematic diagram of a disk drive. Data bits are stored in concentric circles called tracks on the disk surface. The read/write transducer is fabricated on the trailing edge of the slider, which flies over the spinning disk on an air-bearing surface (ABS). The ABS is a thin film of air that is moving at almost the same speed as the disk

underneath the slider. The slider is designed to have a profiled aerodynamic surface. It is lifted from the disk by the aerodynamic force of the ABS. A thin flexible structure called the suspension pushes down the slider to balance the uplifting aerodynamic force. The ABS has a very stiff dynamic behavior and maintains the slider at a constant flying height of 10-15 nanometers over contours of the disk surface in spite of undulation and roughness. The smaller the size of the data bit, the lower of the flying height must be.

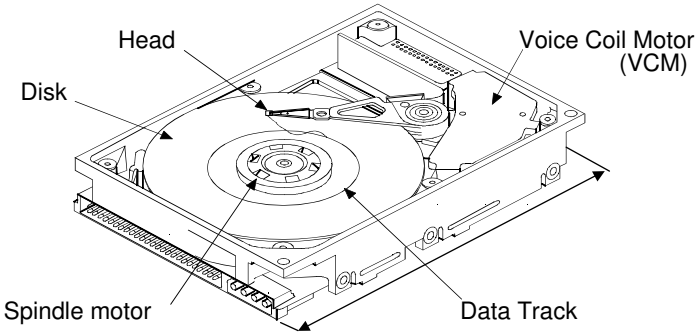

Figure 1.2: A schematic diagram of an HDD. (Courtesy of M. Kobayashi, HITACHI)

Fig. 1.3 shows a schematic diagram of the head-stack and actuator assembly in a disk drive. It consists of heads/sliders, suspensions, an E-block, a pivot, and a voice-coil motor (VCM). The suspensions are swaged onto the arms of the E-block, which lies between the VCM and the suspensions and contains the pivot point. The VCM is a rotary actuator. It moves the heads over the disks by rotating the E-block about the pivot. Traditional disk drive servo system is an un-collocated control system due to the existence of multiple mechanical resonance modes of the E-block and the suspensions, which are located between the VCM and the head.

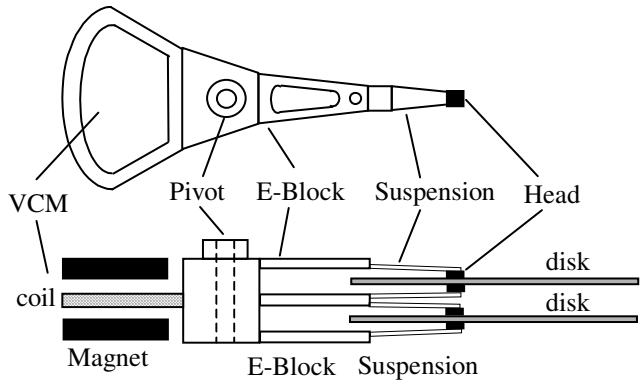

Figure 1.3: VCM actuator in an HDD.

1.1.2 Track Mis-Registration (TMR)

Because of disk slip, spindle rocking motion, and mechanical vibrations in the disk and spindle assembly, real data tracks are not perfectly centered ideal circles. The head itself moves due to various disturbances and mechanical vibrations in the head-stack and actuator assembly. Track Mis-Registration (TMR) is defined as the offset between the pass of the read head (read track) and the pass of the write head (written track) [61]. The definition of TMR has two aspects: write-to-read TMR, defined as the offset between the read track and the written track, and write-to-write TMR, defined as the difference between the nominal track pitch and the actual spacing between two adjacent written tracks. Write-to-read TMR can cause reading of erroneous information, while write-to-write TMR can cause loss of data due to encroachment of the adjacent tracks.

Neither write-to-read nor write-to-write TMRs can be measured directly. Instead, they are quantified by the servo TMR. Servo TMR is often simply called TMR and is defined by the statistical distribution of the deviation of the head from the servo track, which

is called the position error signal (PES). PES is obtained by reading encoded position information on the servo track by the head. Assuming that the PES is a Gaussian distribution, TMR can be represented by three-times standard deviation of the PES, $3\sigma_{PES}$.

Servo tracks are pre-written by the servo writer, which uses a laser interferometer position sensor and a push-pin to accurately control the head position. The position error introduced during servo writing, or the offset between the servo track and the ideal circle track, is called written-in TMR. Written-in TMR affects write-to-write TMR by squeezing adjacent tracks, as illustrated in Fig. 1.4.

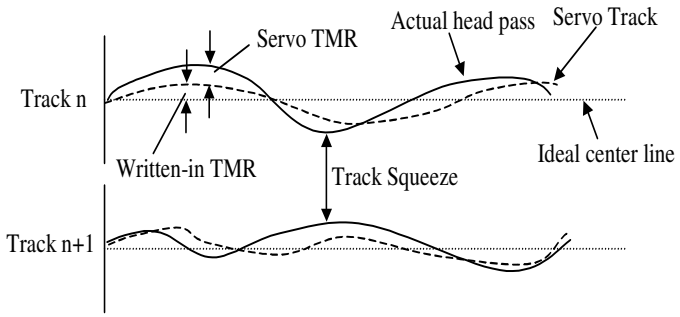

Figure 1.4: Illustration of Track-Mis-Registration

.

TMR can be divided into two main components: repeatable runout (RRO) and non-repeatable runout (NRRO). RRO is synchronous with spindle rotation. The spectral components of RRO appear at the spindle rotation frequency and its harmonics. For RRO, the radial motion at a given location on a track is the same for every revolution of the disk. The main cause of RRO is disk slip when there is a mismatch between the disk center and the spindle rotation axis. Written-in TMR is another main source of RRO.

NRRO is not synchronous with spindle rotation speed. Primary NRRO contributors include [11], [61]:

- Spindle runout, caused by the spindle bearing, tilting of the spindle, vibrations of the spindle and disk assembly, etc. Its spectral components are mainly located at low frequencies.
- Disk flutter, vibrations of the disk excited by air turbulence over its surface. Its spectral components are mainly located between 400 Hz and 1.5 kHz [36] [17].
- Arm torque disturbances due to airflow and spindle rotation. Runout due to arm torque disturbances is mainly at low frequency because of the low-pass characteristic of the actuator dynamics.
- Seek settling runout caused by residual mechanical vibrations and transient response induced by seek operations.
- Windage, caused by excitation of high frequency structural resonance modes of the head-stack and actuator assembly by the air turbulence.
- External vibrations and shocks.
- Bias forces due to the flexible cable, pivot friction, and airflow disturbance.
- PES demodulation and quantization noise, DAC quantization noise, etc.

The actual contributions to the NRRO from each of the above sources are related to a variety of factors, such as form factor, spindle rotation speed, number of disks, application environment, mechanical and servo designs, etc.

1.1.3 Position Error Signal (PES)

In order to perform closed-loop servo control, the head position relative to the track, or the position error signal (PES), must be made available to the control system. Modern disk drives use an embedded servo-sector method to obtain this signal, in which the disk surface is divided into data sectors and servo sectors. The servo sectors contain encoded position information and are patterned as radial spokes, as shown in Fig. 1.5a [29].

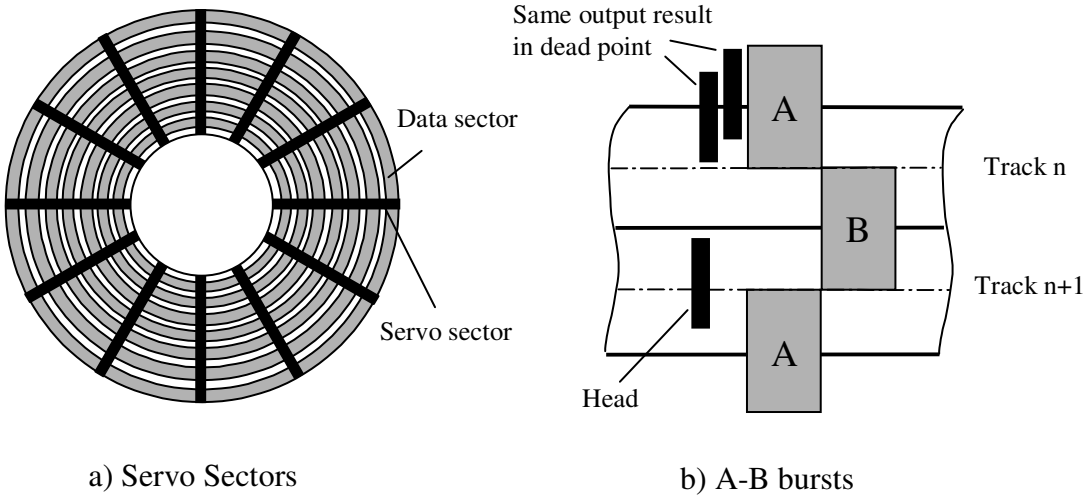

Figure 1.5: Servo sectors and A/B bursts pattern

.

The encoded position information includes track number, sector number and burst patterns. Burst patterns are used to derive the PES. Fig. 1.5b shows A/B bursts patterns. The width of the burst is one track and it is located between the centerlines of adjacent tracks. The read signal amplitude is proportional to the length of the part of the burst that

is covered by the head as it flies over. Thus head position can be determined by

$$PES = w\frac{A-B}{A+B}\,, \tag{1.1}$$

in which w is the width of the head, and A and B represent the signal magnitudes of A and B bursts, respectively. When the head is sitting on the center of the data track, PES equals zero. Since the read element is usually 20-30% narrower than the width of the data track, there are dead spots when the read element does not cross the centerlines. Modern disk drives use A/B/C/D four-burst patterns to eliminate dead spots and increase resolution.

Since the servo sectors are located at discrete locations, PES is a sampled digital signal and the disk drive control system is a digital control system. The sampling frequency is determined by the disk rotation speed and the number of servo sectors on a track. For example, a 7200-RPM disk drive with 180 servo sectors has a PES sampling frequency of 21.6 kHz. Given a disk rotation speed, higher PES sampling frequency requires more servo sectors and reduces storage efficiency.

1.1.4 Servo Control Architecture

A disk drive servo control system has two primary functions: seeking control and tracking control. In seeking control, the head is moved from track to track as quickly as possible to locate data. In tracking control, the head is kept as close as possible to the track center such that data bits can be reliably written or read. Seek time determines how fast data can be accessed, while tracking accuracy determines how densely data tracks can be partitioned. Modern disk drive servo control systems use a combination of feedback and feedforward control to achieve fast seeking and accurate tracking.

Fig. 1.6 shows a block diagram of the disk drive servo control system. $G_P(s)$ represents the disk drive actuator plant. C_{FB} and C_{FF} are the feedback and feedforward controllers, respectively. r denotes the reference input, which is zero in track-following mode and a desired position trajectory in seek mode. d_n, d_f, and d_p denote the measurement noise, the force disturbance, and the position disturbance (due to both track motion and head motion), respectively. r_{ff} is a reference input to the feedforward controller, which can be predetermined or measured by auxiliary sensors in real-time.

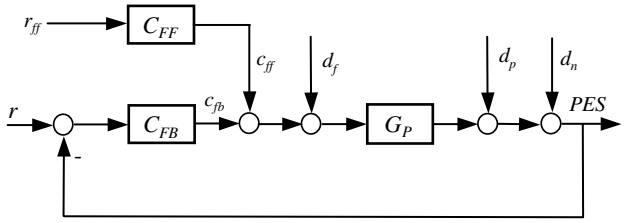

Figure 1.6: Disk drive servo control architecture.

In track-following mode, the PES can be written as

$$PES(k) = S(z)G_P(z)d_f(k) + S(z)d_p(k) + S(z)d_n(k) + C_{FF}(z)r_{ff}(k)\,, \tag{1.2}$$

where $S(z)$ is the closed-loop sensitivity function defined by

$$S(z) = \frac{1}{1 + C_{FB}(z)G_P(z)}\,. \tag{1.3}$$

The sensitivity function, also called the error rejection function, is the most basic function used to specify and evaluate the performance of disk drive servo control systems. Fig. 1.7 shows the frequency response of a typical sensitivity function. Its unity-gain frequency, at which the magnitude of the sensitivity function is one, is related to the bandwidth of the control system. Below this frequency, the sensitivity function attenuates disturbances

and noise. Above this frequency, it amplifies them. Since the major TMR sources are located in the low-frequency range, as discussed previously, the most effective way to minimize the PES and increase the tracking accuracy is to increase the servo control bandwidth. In general, bandwidth is limited by high-frequency resonance modes of the plant dynamics and/or the sampling frequency and the computational time delay [57].

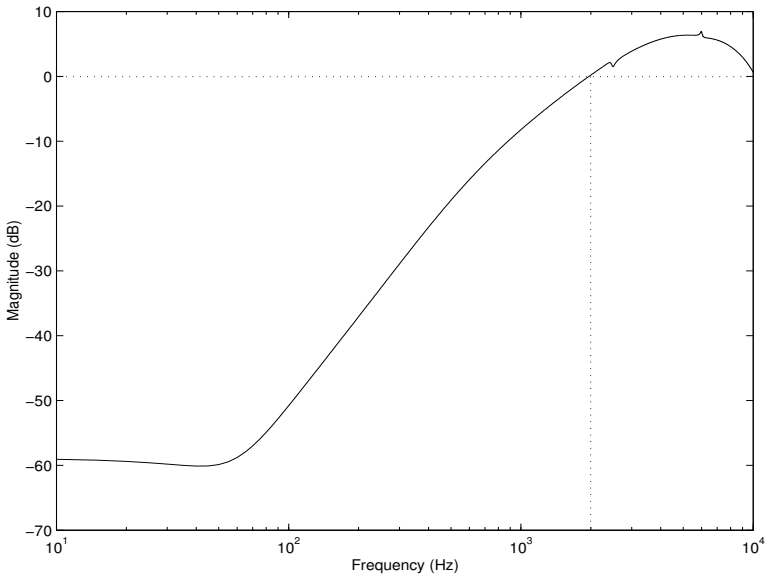

Figure 1.7: Sensitivity function frequency response.

There are several constraints in the feedback controller design. First, if not designed properly, the feedback controller may become unstable in the presence of plant model variations. There is a tradeoff between achieving better performance and maintaining robustness of the controller. Increasing the control bandwidth often results in reduced stability margins.

The second constraint is Bode's sensitivity integral theorem [6]. It states that for a continuous-time system, if the loop transfer function is asymptotically stable and has

relative degree of at least two, then

$$\int_0^\infty \log |S(j\omega)| d\omega = 0\,, \tag{1.4}$$

which means the magnitude of the sensitivity function $|S(j\omega)|$ cannot be less than one at all frequencies, and if it has more attenuation in certain frequency region, there must be less attenuation or larger amplification at other regions. There is a similar sensitivity integral constraint for discrete-time systems [39].

Feedforward control is very effective in cancelling certain disturbances that can be either determined a priori or measured in real-time. The main difference of feedforward control from feedback control is that the input signal to the feedforward controller, r_{ff} in Fig. 1.6, does not depend on the state of the system. One advantage of feedforward control is that there is no stability issue. The performance of feedforward control is also not constrained by Bode's integral theorem. The feedforward controller can be designed to be a zero-phase error tracking controller (ZPETC) if the plant model is known [56]. When the plant model is unknown or changes, the feedforward controller is often designed to be a finite-impulse response (FIR) filter, which can be adaptively tuned.

Feedforward control has been widely used in seek control and cancelling repetitive runout (RRO). In these two cases, u_{ff} can be either predetermined or estimated a priori. Acceleration feedforward control has been shown to be effective in cancelling external disturbances [59] [58] [47] [46]. In this case, external disturbances are measured in real-time by an accelerometer attached on the disk drive.

1.1.5 Storage Density Increase and Advanced Servo Control

Historically, increases in storage density have been achieved by almost equal increases in track density, the number of tracks encircling the disk, and bit density, the number of bits in each track. This trend is likely to change as storage density approaches the superparamagnetism limitation, which refers to the fact that the time a media grain retains information against thermal decay is reduced as its dimension shrinks [23] [37]. Increasing either bit density or track density reduces media grain size. However, higher bit density also requires reduced magnetic gap spacing, which in turn requires a thinner magnetic layer. Thus, for the same areal density increase, the media loses more thermal stability by increasing bit density than by increasing track density. It has been predicted that future areal storage density increases in HDDs will be achieved mainly through an increase in track density [23].

Increasing track density requires more precise positioning control of the read/write head. Advanced research of the HDD industry is now targeting an areal density of one terabit per square inch. For a predicted bit aspect ratio of 4:1, this translates to a linear bit density of 2M bits per inch (BPI), and a radial track density of 500K tracks per inch (TPI), which in turn implies a track width of 50 nm. A simple rule of thumb for servo control design in HDDs is that three-times the statistical standard deviation of the PES should be less than 1/10 of the track width. Thus, a servo precision of 5 nanometers in the 3σ value of the PES will be required to achieve such storage density.

Traditional disk drive servo systems utilize a single VCM to move the head and have some limitations. First, since the VCM/E-block/suspension actuator assembly is large

and massive as a unit, the speed at which the head can be controlled is limited. Furthermore, there are multiple mechanical resonance modes in the E-block arms and suspensions which lie between the VCM and the head. These resonance modes impose a limit to the achievable control bandwidth. Limited sampling frequency of the PES is another factor affecting the servo performance. Advanced servo technologies using dual-stage multi-sensing servo systems have been developed to overcome these limitations.

Besides storage density increases, spindle rotation speed is continuing to increase in order to achieve shorter latency and faster data transfer rate. Higher rotation speeds induce larger disturbances and air turbulence. For track densities as high as 500k TPI, air turbulence excited structural vibrations of the actuator assembly alone are enough to force the head off-track. These vibrations occur at frequencies higher than the expected servo control bandwidth and can not be attenuated by the conventional servo systems. Advanced servo systems using MEMS microsensors and microactuators are being developed to suppress turbulence excited structural vibrations.

1.2 Dual-Stage Multi-Sensing Servo Systems

1.2.1 Dual-Stage Actuator Servo Systems

One solution to overcoming the limitations of traditional servo system is to complement the VCM with a smaller, secondary mini/micro-actuator to form a dual-stage actuator servo system. The second-stage actuator can avoid the excitation of the arm and the suspension resonance modes, bypass the pivot friction, and reduce the driving inertia. The VCM does low bandwidth course positioning, while the second-stage actuator does high

bandwidth fine positioning.

Many configurations of dual-stage servo systems have been developed. They can be categorized into three groups: "actuated suspension", "actuated slider" and "actuated head", by the location the second-stage actuator is placed.

Actuated Suspension

In this approach, two actuators made from piezoelectric materials, such as PZT, are placed near the root of the suspension. They generate a push-pull action when driven differentially. A leverage mechanism is used to convert and amplify this small actuation displacements into large head motion [48] [44] [32] [33] [8]. Fig. 1.8 shows a schematic diagram of such a device.

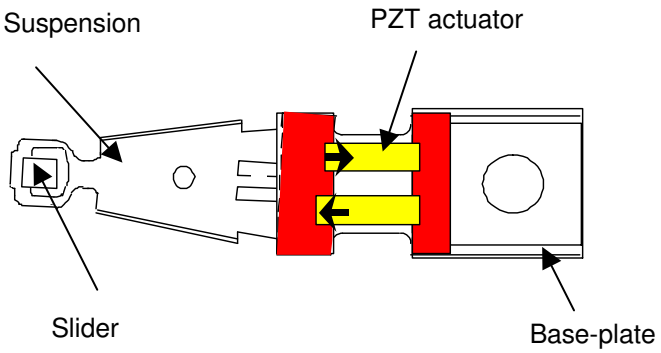

Figure 1.8: A schematic diagram of a PZT-actuated suspension (Courtsy of M. Kobayashi, HITACHI)

PZT-actuated suspensions can be easily integrated into a traditional single-stage servo system since the head gimbal assembly (HGA) interfaces are not changed. The major drawback of this approach is that the PZT actuators can still excite the arm and suspension resonance modes. Thus, the achievable bandwidth is still limited. Moreover, in order to

increase the actuation gain from the actuators to the lateral head motion and reduce driving voltage, PZT-actuated suspensions are usually designed to have a relatively low frequency sway mode. This makes these suspensions more susceptible to air turbulence excitations than their conventional counterparts.

The servo performance of actuated suspensions remains limited when compared to the next two approaches. However, this approach is expected to be the first to be deployed in commercial disk drives.

Actuated Slider

In this approach, a microactuator is placed between the slider and gimbal to position the slider/magnetic head. The resulting servo bandwidth of this approach can be higher than the previous approach because the secondary actuator bypasses the mechanical resonances of the arm and the suspension. This approach uses existing sliders and microactuators that can be batch fabricated, and thus could be cost effective. However, the size and mass of the microactuator are significant relative to those of current sliders, and this may interfere with slider flying stability. Therefore, current suspensions need to be re-designed to adopt this secondary actuator. Suitable driving forces in this approach include electrostatic, electromagnetic and piezoelectric [21] [42] [19] [53] [13] [35]. Fig. 1.9 shows a picture of a MEMS electrostatic microactuator and slider mounted on a suspension.

The main advantage of electrostatic microactuators that are designed and fabricated using MEMS technologies is that they have very clean dynamic responses. Thus dual-stage servo systems based on MEMS microactuator actuated-slider approach poten-

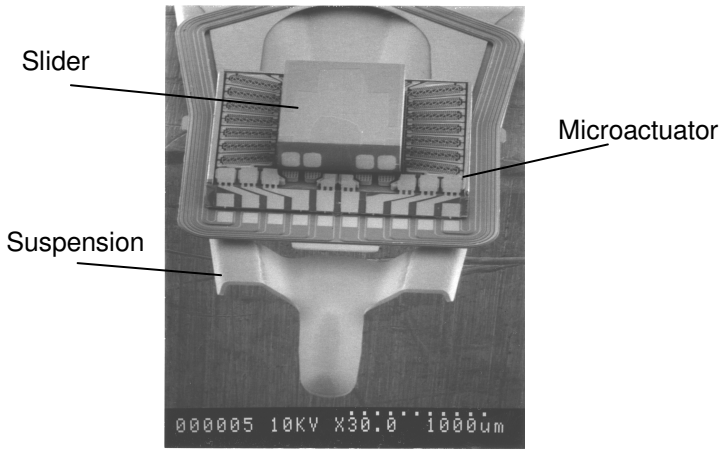

Figure 1.9: A MEMS electrostatic microactuator and slider mounted a suspension. (Courtesy of L.-S. Fan, IBM)

tially can achieve a much higher bandwidth than those based on actuated-suspension approach. Another advantage of MEMS microactuators is that capacitive position sensors can be integrated to the microactuator design. The main drawback of this approach is the increased complexity in integrating the microactuator with the gimbal and the slider. To further reduce this assembly task and improve the performance, some researchers have proposed microactuators that are either integrated with the gimbal structure [42] or the slider [27].

Actuated Head Elements

In this approach, the microactuator is designed to be an integrated part of the slider, actuating the magnetic head elements directly with respect to the rest of the slider body [15] [28] [43]. As these microactuators are very small, they only slightly increase the slider weight, and are thus capable of working with current suspension assemblies. Researchers have successfully demonstrated the integrated fabrication process for fabricat-

ing the electrostatic microactuators and magnetic heads within one piece of ceramic block (slider). The embedded electrostatic microactuator has its resonance close to 30 kHz and was able to position the magnetic head relative to the rest of the slider body by 0.5 μm [28] [43]. However, the integration of slider, actuator, and read/write head remains a challenge.

In this dissertation, we will discuss controller design of PZT-actuated suspension and MEMS microactuator actuated-slider dual-stage actuator servo systems .

1.2.2 Multi-Sensing Servo Systems

Another technique to overcome the limitations of traditional disk drive servo systems is multi-sensing servo control by adding auxiliary sensors. Two main applications have been investigated: resonance control by active damping and external disturbance rejection by acceleration feedfoward control.

As mentioned earlier, the control bandwidth of traditional single-stage servo systems is limited by the resonance modes of the head-stack and actuator assembly. By actively damping these resonance modes, the bandwidth of single-stage actuator servo systems can be expanded. The assembly butterfly mode is the biggest constraint to the control bandwidth because of its large resonance peak and low resonance frequency. Two sensing and control schemes have been developed for active damping control of the butterfly mode: accelerometers placed at the tip of the E-block arm [31], and strain sensors attached to the surface of the E-block [25].

Another application of multi-sensing servo is in external disturbance rejection using acceleration feeforward control [59] [58] [47] [46]. In this case, accelerometers are placed on the base plate of the disk drive to detect external disturbances. The output of the

accelerometer is applied to a feedforward controller which controls the actuator to cancel the effects of external disturbances before they affect the head position.

1.3 Research Objectives

Many controller design methodologies have been developed for dual-stage servo control systems. They can be largely classified into two categories: those based on decoupled or sequential single-input single-output (SISO) design methods, such as master-slave method, decoupled master-slave method [40], PQ method [51], and parallel design method [52], and those based on modern optimal control design methods, such as LQG [63], [55], LQG/LTR [24], [54], H_∞ [55], [49], and μ-synthesis [18], etc. A more detailed overview of these design methodologies is presented in Chapter 3, section 3.1.

Dual-stage actuator servo systems are multi-input multi-output (MIMO) systems. The servo control design for dual-stage disk drives faces new challenges in terms of plant dynamics variations and dynamics coupling between the two actuators. However, not much attention has been paid to these issues in previous work. The first objective of this dissertation is to develop new robust and adaptive controller design methodologies for dual-stage servo control design.

The plant dynamics of dual-stage actuators have unit-to-unit variations due to manufacturing tolerances in mass production, and they change with operating environment. Furthermore, there exists significant dynamic coupling in actuated suspension dual-stage actuators. Classical gain and phase margins computed one-loop-at-a-time cannot fully characterize and evaluate the stability and performance robustness of the dual-stage servo

control system since they cannot capture the effects of simultaneous and cross-coupling of variations. Continuing the work in [18], a truly coupled MIMO plant model with structured uncertainty was established for a PZT-actuated suspension dual-stage servo system. Robust control design and analysis based on μ-synthesis and analysis were developed. For controller design of a MEMS microactuors dual-stage servo system, an adaptive control scheme was developed to compensate for the variations in microactuator's resonance mode.

The second objective of this dissertation is to investigate the feasibility and control schemes of active vibration compensation using dual-stage multi-sensing servo systems to suppress air turbulence induced structural vibrations (windage). The adoption of dual-stage servo systems will change the paradigm of the PES spectrum. TMR contribution from windage vibrations become more important due to the increased attenuation of low-frequency disturbances and runout by the high bandwidth dual-stage servo system. The trend of further increasing the TPI and spindle rotation speed may require active compensation of the actuator structural vibrations.

In this dissertation, control schemes of combining dual-stage actuators and multi-sensing servo systems for active vibration compensation are investigated. Feedback damping control, which can be applied to actuated-suspension dual-stage servo systems, and feedforward control, which can be applied to actuated-slider/head dual-stage servo systems, are proposed to suppress the TMR due to windage vibrations.

1.4 Outline of the Dissertation

The dissertation is organized as follows. Chapters 2, 3 and 4 discuss modeling and controller design of a PZT-actuated suspension dual-stage servo system. Chapter 2 presents modeling of the system. The experimental setup is described. Frequency response modal testing to establish a coupled MIMO dual-stage plant modal is presented. Chapter 3 focuses on robust track-following controller design. Model uncertainty representations are described. Design and experimental results of decoupled SISO design and robust μ-synthesis design are presented and compared. Chapter 4 presents the feedback damping control of the PZT-actuated suspension dual-stage system using one PZT element on the PZT-actuated suspension as a vibration sensor.

Chapter 5 discusses adaptive control of MEMS microactuator dual-stage servo systems. A decoupled design structure with microactuator minor-loop damping and a design methodology by discrete-time pole placement are proposed. A self-tuning control scheme is developed to compensate for the variations in the microactuator's resonance mode. The formulation of adaptive feedforward control to compensate windage vibrations using MEMS microactuator is presented. Simulation results are presented to verify the proposed control schemes.

Chapter 6 concludes the dissertation by summarizing the results and major achievements. Recommendations of future work are discussed.

Chapter 2

Modeling of the PZT-Actuated Suspension Dual-Stage Actuator

This chapter presents the modeling of the PZT-actuated suspension dual-stage actuator. The basic actuator and sensor equations of the PZT-actuated suspension are derived. The experimental setup is described. Major vibration modes of the dual-stage actuator are analyzed. Modal testing to establish a coupled MIMO plant model of the dual-stage actuator is presented.

2.1 Actuator and Sensor Models of the PZT-Actuated Suspension

Constitutive Equations of Piezoelectric Sensors and Actuators

Direct piezoelectric effect refers to the generation of electrical charge on the surfaces of a segment of material when a force (stress) is applied. Analogously, converse piezoelectric effect refers to the change in strain for a free element (or stress for a clamped element) when an electrical field is applied. Piezoelectric materials can be made as sensors and actuators using these two effects. The basic electromechanical constitutive equations of a three-dimensional piezoelectric element can be written as [38]:

$$\mathbf{D} = \mathbf{d} \cdot \mathbf{T} + \mathbf{p} \cdot \mathbf{E}, \tag{2.1}$$

$$\mathbf{S} = \mathbf{s} \cdot \mathbf{T} + \mathbf{d} \cdot \mathbf{E}, \tag{2.2}$$

where

D: electric displacement vector (3 components), $Coulomb/m^2$;

d: piezoelectric coefficients tensor (3rd order, 27 components), $Coulomb/Newton$;

T: stress tensor (2nd order, 9 components), $Newton/m^2$;

p: permittivity tensor (2nd order, 9 components), $Farad/m$;

E: electric field intensity vector (3 components), $Volt/m$;

S: strain tensor (2nd order, 9 components), dimensionless;

s: elastic compliance tensor (4th order, 81 components), $m^2/Newton$.

Eq. (2.1) is referred to as the sensor equation and Eq. (2.2) is referred to as the actuator equation. They can be simplified using symmetric and isotropic properties of the

material. In particular, for a one-dimensional sensing/actuation piezoelectric element using 1-direction mechanical and 3-direction electrical relations, as shown in Fig 2.1, Eqs. (2.1) and (2.2) are simplified to the following scalar equations

$$D = d_{31}\sigma + \epsilon E\,, \tag{2.3}$$

$$\varepsilon = \frac{1}{Y}\sigma + d_{31}E\,, \tag{2.4}$$

where σ, ε, and Y are the mechanical stress, strain, and Young's modulus in the 1-direction, respectively; E, D and ϵ are the electric field intensity, electric displacement and permittivity in the 3-direction, respectively; d_{31} is the piezoelectric constant relating applied stress in the 1-direction and generated electric displacement in the 3-direction (or equivalently applied electric field in the 3-direction and generated strain in the 1-direction).

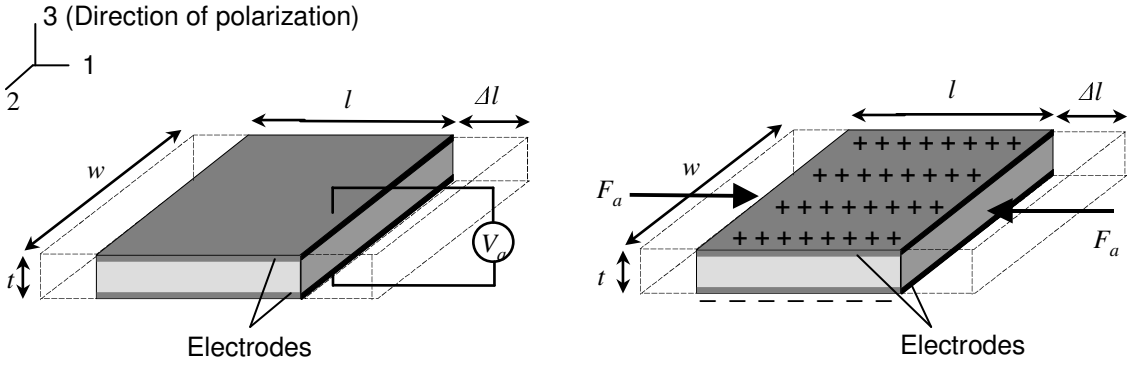

a) Actuator: applied voltage in 3-direction generates mechanical strain in 1-direction.

b) Sensor: applied force in 1-direction generates electrical charge in 3-direction.

Figure 2.1: Diagrams of piezoelectric sensor and actuator.

Typical piezoelectric materials used for sensor and actuator applications include Quartz, PZT (Lead Zirconate-Titanate), ZnO, and PVDF (Poly-Vinylidene Fluoride).

Piezoelectric Strain Sensors

Piezoelectric films can be used as strain sensors to detect structural vibrations. Consider a piezoelectric element subjected to applied forces as shown in Fig. 2.1b, from the sensor equation Eq. (2.3), the electric displacement in the 3-direction is (applied electrical field $E = 0$)

$$D = d_{31}\sigma = d_{31}Y\varepsilon. \tag{2.5}$$

The generated charge in the 3-direction is

$$Q = \int DdA = d_{31}Y\varepsilon wl\,, \tag{2.6}$$

where w and l are the width and length of the piezoelectric element, respectively.

The piezoelectric element itself is a capacitor with capacitance

$$C_P = \frac{\epsilon_r\epsilon_o wl}{t}\,, \tag{2.7}$$

where ϵ_r is the dielectric constant in the 3-direction, and ϵ_0 is the free space permittivity. An equivalent circuit of the piezoelectric sensor can be represented by a voltage source in series with a capacitor, as shown in Fig. 2.2. The open-circuit output voltage is

$$V_o = \frac{Q}{C_P} = \frac{d_{31}Yt}{\epsilon_r\epsilon_o}\varepsilon\,. \tag{2.8}$$

The output voltage is linear to the strain with a constant proportional to the thickness of the piezoelectric element.

The output of a piezoelectric sensor can be amplified by a charge or voltage amplifier [41]. Fig. 2.3a shows the circuit of a non-inverting voltage amplifier. The amplifier output is

$$V_{out} = \frac{Q}{C_P}\left(1 + \frac{R_2}{R_1}\right)\,. \tag{2.9}$$

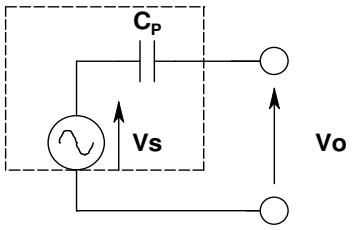

Figure 2.2: Equivalent circuit of the piezoelectric sensor.

To increase the voltage output, the cable should be as short as possible to reduce parasitic capacitance. Fig. 2.3b shows the circuit of a charge amplifier. The amplifier output is

$$V_{out} = -\frac{Q}{C_F}\,. \tag{2.10}$$

The main advantage of the charge amplifier is that the output voltage depends only on the feedback capacitance, but not the capacitance of the sensor and the cable. Therefore, longer cables can be used. Both kinds of amplifiers have high-pass characteristics. The time constant of the voltage amplifier is RC_P, while that of the charge amplifier is RC_F. [41]. Thus, piezoelectric sensors are usually not suited for sensing static or very low-frequency signals.

Actuator Model of the PZT-Actuated Suspension

A PZT-actuated suspension uses two PZT elements located between the base plate and the load beam of the suspension, as shown in Fig. 2.4a. The two PZT elements are polarized oppositely and connected in parallel. When a voltage is applied to them, one extends and the other contracts. The push-pull action rotates the load beam about a hinge and moves the head located at the tip of the load beam. Fig. 2.4b shows a simplified

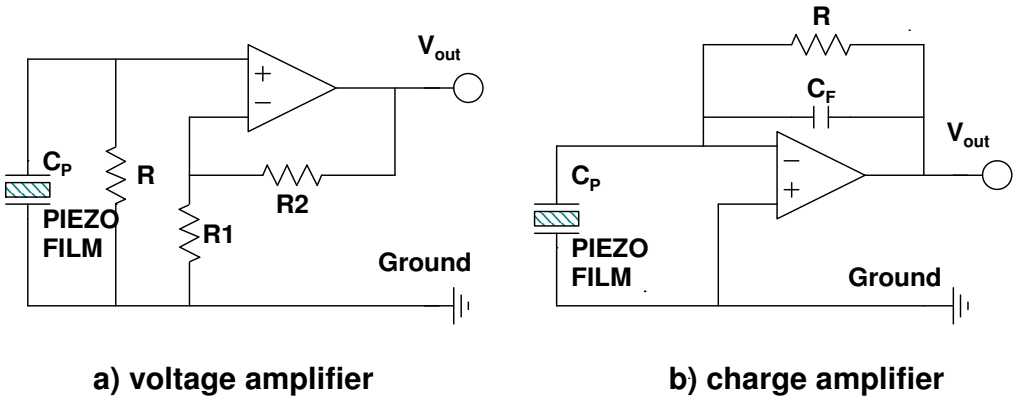

Figure 2.3: Piezoelectric sensor amplifiers.

mechanical model for the PZT-actuated suspension with lumped parameters. Structural damping is neglected in this model.

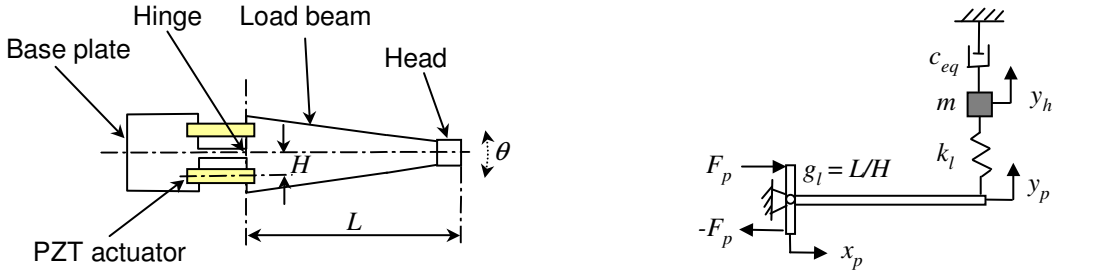

Figure 2.4: Lumped parameter model of the PZT-actuated suspension.

The load beam is modeled to be a mechanical leverage with gain, $g_l = L/H$, and an equivalent spring k_l. c_{eq} denotes the equivalent air damping acting on the slider. F_p represents the force generated by the PZT actuator. The leverage balance equation gives

$$F_p = g_l k_l \left(y_p - y_h\right)/2\,, \tag{2.11}$$

where y_h denotes the displacement of the slider, y_p denotes the displacement at the end of the leverage. The equation of motion of the slider is

$$m\ddot{y}_h = -c_{eq}\dot{y}_h - k_l\left(y_h - y_p\right) , \tag{2.12}$$

where m denotes the mass of the slider. From Eqs. (2.11) and (2.12), we have the following transfer functions

$$\frac{Y_h(s)}{Y_p(s)} = \frac{k_l}{ms^2 + c_{eq}s + k_l} \tag{2.13}$$

$$\frac{Y_h(s)}{F_p(s)} = \frac{2}{g_l\left(ms^2 + c_{eq}s\right)} \tag{2.14}$$

The applied stress to the PZT element due to the actuation force is

$$\sigma = -\frac{F_p}{wt} , \tag{2.15}$$

where w and t are the width and thickness of the PZT element, respectively. The strain of the PZT element equals

$$\varepsilon = \frac{x_p}{l} = \frac{y_p}{lg_l} , \tag{2.16}$$

where l is the length of the PZT element. The electrical field intensity given the applied voltage V_a is

$$E = \frac{V_a}{t} . \tag{2.17}$$

Substituting Eqs. (2.13)-(2.17) to the actuator equation Eq. (2.4), we can obtain the following 2nd-order transfer function from the applied voltage to the head lateral motion

$$G_p(s) = \frac{Y_h(s)}{V_a(s)} = \frac{2d_{31}g_l lYwk_l}{\left(2Ywt + lk_l g_l^2\right)ms^2 + \left(2Ywt + lk_l g_l^2\right)c_{eq}s + 2Ywtk_l} . \tag{2.18}$$

The DC gain relating the applied voltage to the head lateral motion is

$$g_{DC} = d_{31}g_l\left(\frac{l}{t}\right) . \tag{2.19}$$

Thus, the longer and thinner the actuator, the larger the DC gain. However, the PZT actuator must maintain enough stiffness in the out-of-the-plane direction to support the pre-load of the slider. Thus, its thickness cannot be too small. A multi-layer PZT actuator can maintain the same out-of-the-plane stiffness, while achieving a larger DC gain (lower driving voltage).

The actual dynamics of the PZT-actuated suspension are coupled with the resonance modes of the arm and other suspension torsion modes.

Sensor Model of the PZT-Actuated Suspension

The PZT element can also be used as a sensor. There are two PZT elements on the PZT actuated suspension. It is possible to use one of them as a vibration sensor and the other as an actuator for vibration damping control. Now consider the model in Fig. 2.4b but with only one PZT element driving, the actuation force of the actuating PZT element equals

$$F_{p1} = g_l k_l \left(y_p - y_h\right) + \varepsilon Y w t \,, \tag{2.20}$$

where ε is the strain of the sensing PZT element. Note that the strains of the two PZT elements are equal in magnitude. It can be verified that the transfer function from V_a to y_h now becomes half of that when both PZT elements are used for driving. We have

$$G_{p1} = \frac{Y_h(s)}{V_a(s)} = \frac{1}{2} G_p \,. \tag{2.21}$$

From Eqs. (2.4), (2.12), (2.15), and (2.20), we have

$$\begin{aligned} \varepsilon(s) &= \frac{1}{2}\left(g_l \left(ms^2 + c_{eq}s\right) Y_h(s) + d_{31}\frac{V_a}{t}\right) \\ &= \frac{1}{2}\left(g_l \left(ms^2 + c_{eq}s\right) G_{p1} + \frac{d_{31}}{t}\right) V_a \,. \end{aligned} \tag{2.22}$$

Using Eqs. (2.8), (2.18), (2.21), and (2.22) the transfer function from the driving voltage V_a to the sensing output voltage V_o can be obtained as

$$G_s(s) = \frac{V_o(s)}{V_a(s)} = \frac{d_{31}Yt}{2\epsilon_r\epsilon_o}\left(\frac{d_{31}g_l lYwk_l\left(ms^2 + c_{eq}s\right)}{\left(2Ywt + lk_l g_l^2\right)ms^2 + \left(2Ywt + lk_l g_l^2\right)c_{eq}s + 2Ywtk_l} + \frac{d_{31}}{t}\right). \tag{2.23}$$

Note that there is a direct feedthrough term from the input to the output.

2.2 Experimental Setup

Fig. 2.5 shows a picture of the experimental setup of the PZT-actuated suspension dual-stage servo system. It consists of a dual-stage actuator disk drive, a laser Doppler vibrometer (LDV), a digital signal processor (DSP) board and an amplifier board.

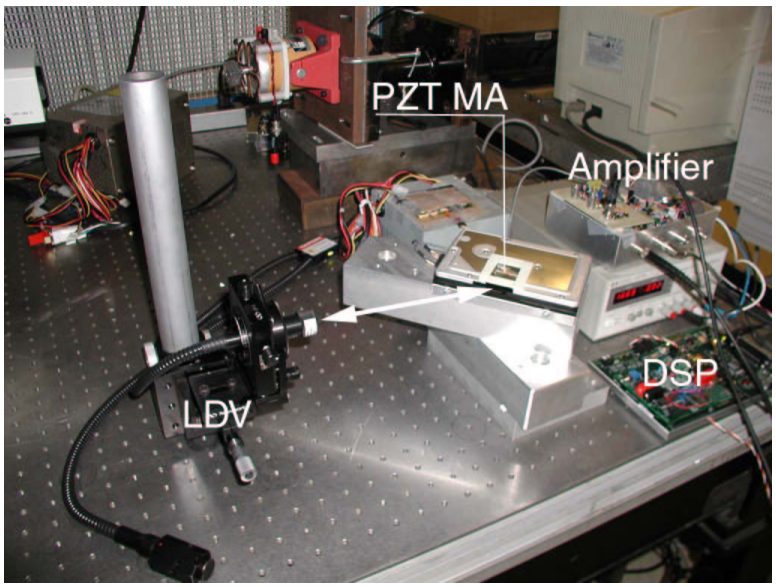

Figure 2.5: Experimental setup.

The PZT-actuated suspension used in our testing was provided by Hutchinson Technologies, Inc. (HTI) with model number Magnum-5E. It has a stroke limit of $\pm 1\mu m$

under a driving voltage of $\pm 40V$. The PZT-actuated suspension was installed on the top finger of the E-block in a 7200-RPM disk drive. Head lateral motion was detected by an LDV. An opening was cut on the side of the disk drive to allow the laser to pass through.

One major disadvantage of using an LDV as a position sensor is that track runout cannot be measured. Furthermore, the displacement output of the LDV has low-frequency drifts, mainly below 100 Hz. However, this is generally not a problem for track-following control testing since the drifts act as low-frequency disturbances and can be compensated for by the control system. The displacement output gain of the LDV used in the testing is 0.5 μm/V, and it has a resolution of 2 nanometers.

A floating-point DSP board from Texas Instruments (TI), TMS320C6711 DSK, was used to control the dual-stage servo system. An analog-digital convertor (ADC) daughter board, THS1408 EVM board, also from TI, was connect to the DSK board through its daughter board expansion interface. We designed an analog amplifier board, which has the following components:

- Digital-analog convertor (DAC): TLV5638, 2-channel, 12-bit, 1 μs settling time. It connects to the DSP board through a serial interface.
- PZT actuator amplifier: the amplifier has a gain of 10, resulting in a maximum driving voltage of ± 20 V.
- VCM current driver: a simple voltage to current amplifier is used to drive the VCM. It has a gain of 10 mA/V, resulting in a maximum driving current of ± 20 mA, which is large enough for track-following control.
- Piezoelectric sensor amplifier and analog switch: an instrumentation amplifier, AD624

from Analog Device Inc., is used as a voltage amplifier to the PZT sensor output. An analog switch, MAX319 from Maxim, is used to multiplex LDV or PZT sensor output to the ADC board.

2.3 Modal Testing of the PZT-Actuated Suspension Dual-Stage Actuator

2.3.1 Frequency Response Modal Testing

The PZT-actuated suspension has two PZT elements. Normally, both of them are used as actuators, and the dual-stage servo system is a dual-input single-output (DISO) system, as shown in Fig. 2.6a. It is also possible to use just one of them as an actuator, and use the other one as a sensor. In this case, the dual-stage servo system is a dual-input dual-output (DIDO) control system, as shown in Fig. 2.6b. In chapter 3, the controller designs are based on the normal DISO configuration. In chapter 4, the vibration damping control scheme is based on the DIDO configuration. The modal testing results presented in this section are based on the DIDO configuration. The DISO plant model is just a sub-system of the DIDO plant model by eliminating the PZT senor output.

Let u_1 and u_2 be the inputs to the VCM and the PZT actuator, respectively, and y_1 and y_2 be the head displacement output in the radial off-track direction and the PZT sensor output, respectively. The transfer function from u_j to y_i, $G_{ij}(s),\ i,j = 1,2$, can be written as

$$G_{ij}(s) = \frac{K_0^{ij}}{s^2} + \sum_{n=1}^{N} \frac{\omega_n^2 K_n^{ij}}{s^2 + 2\zeta_n \omega_n s + \omega_n^2} + d_{ij}\,, \tag{2.24}$$

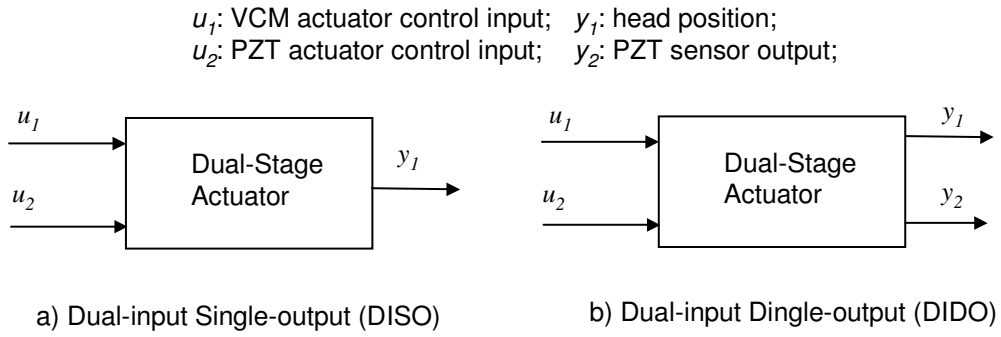

Figure 2.6: DISO and DIDO configurations of the PZT-actuated suspension dual-stage actuator.

which is the summation of the rigid body mode, a number of structural vibration modes and a feedthrough term. In Eq. (2.24), N is the total number of vibration modes considered, ω_n and ζ_n are the natural frequency and the damping ratio of mode n, respectively. K_n^{ij} is the modal constant of mode n from u_j to y_i, and d_{ij} is the direct feedthrough factor from u_j to y_i.

Figs. 2.7-2.10 show the following measured and simulated frequency responses: a) from VCM input u_1 to head displacement y_1; b) from PZT actuator input u_2 to head displacement y_1; c) from VCM input u_1 to PZT sensor output y_2; d) from PZT actuator input u_2 to PZT sensor output y_2. The solid lines are experimentally measured responses, while the dashed lines are simulated responses using the identified model.

As shown in these figures, major vibration modes of the PZT-actuated suspension dual-stage actuator in our setup include the assembly butterfly mode (M1 in the figures), the suspension sway mode (M2), the suspension 2nd torsion mode (M3), and the suspension 1st torsion mode (M4). Among them, the two most important off-track modes are the assembly butterfly mode and the suspension sway mode. Fig. 2.11 illustrates the mode

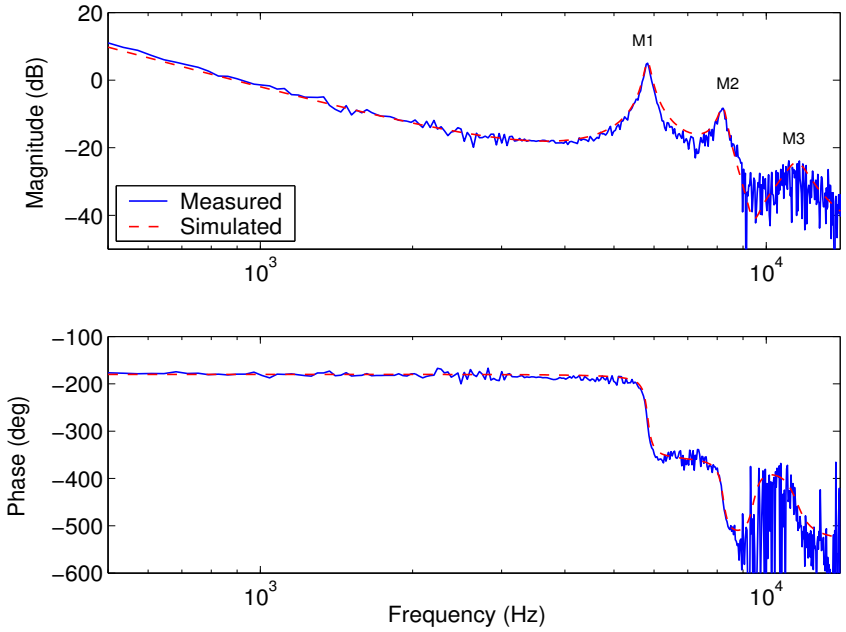

Figure 2.7: Frequency response from VCM input to head displacement.

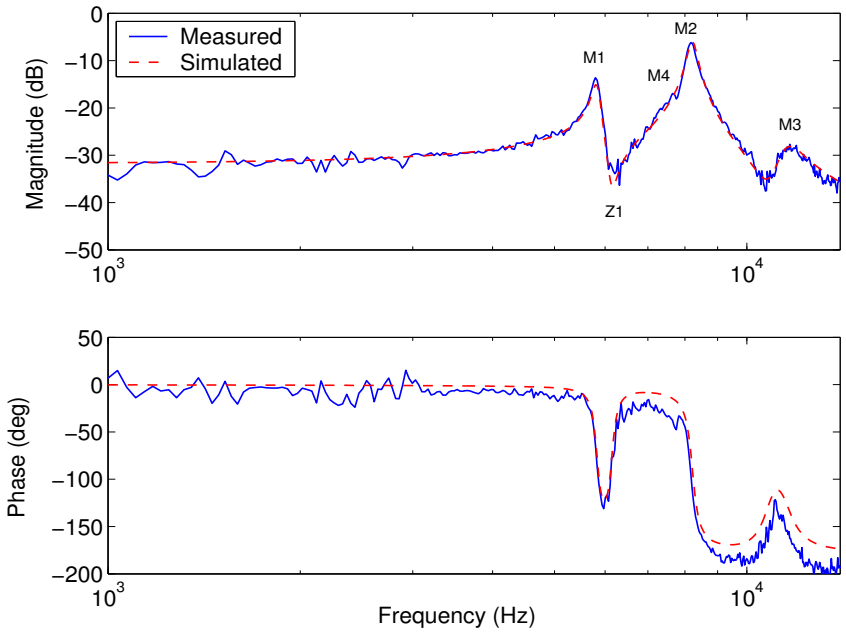

Figure 2.8: Frequency response from PZT actuator input to head displacement.

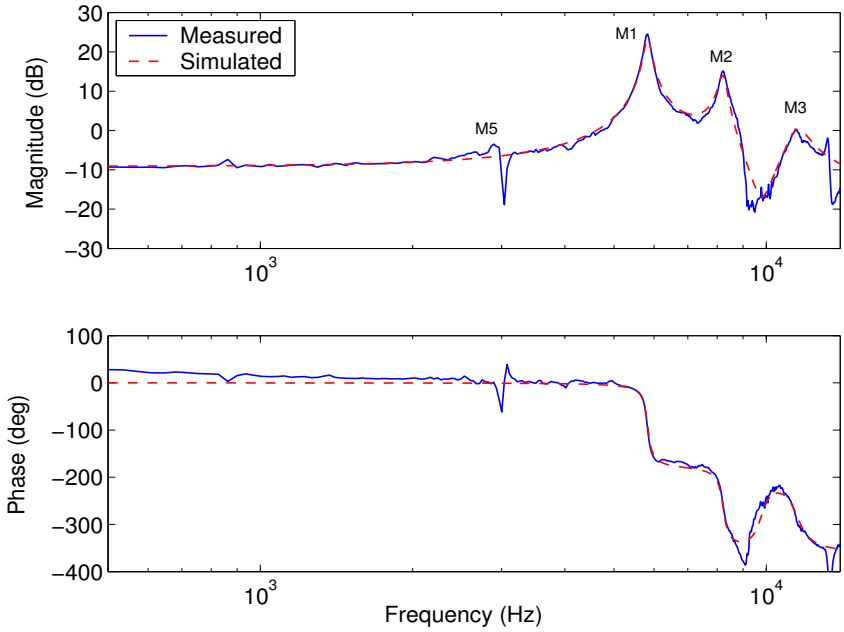

Figure 2.9: Frequency response from VCM input to PZT sensor output.

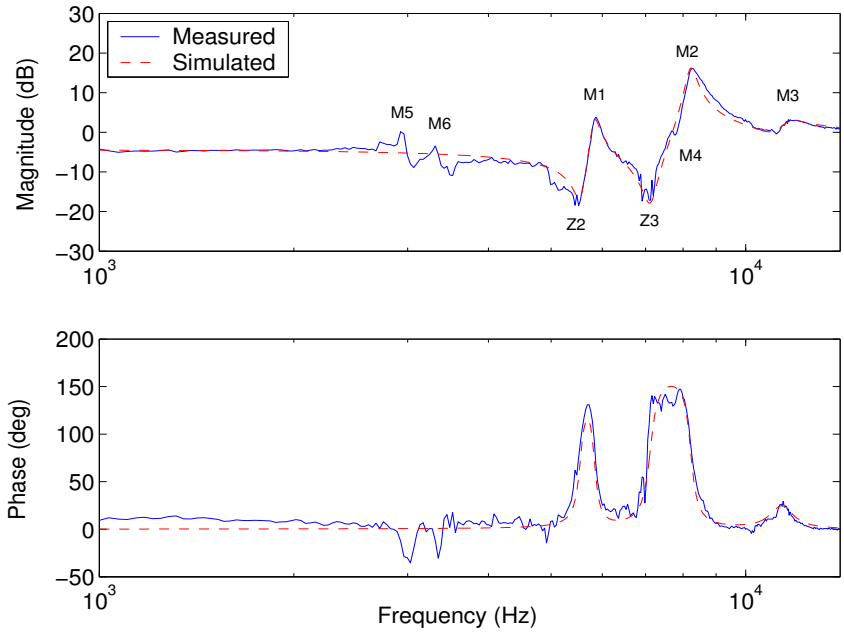

Figure 2.10: Frequency response from PZT actuator input to PZT sensor output.

shapes of these two modes. The assembly butterfly mode is generated by the coupling of in-plane sway modes of the E-block arm and the coil, in which the arm and the coil move out of the phase with respect to each other around the pivot. The suspension sway mode is the mode we discussed in section 2.1, in which the load beam and the slider vibrate with respect to the hinge of the PZT-actuated suspension. It is also called the PZT actuator mode.

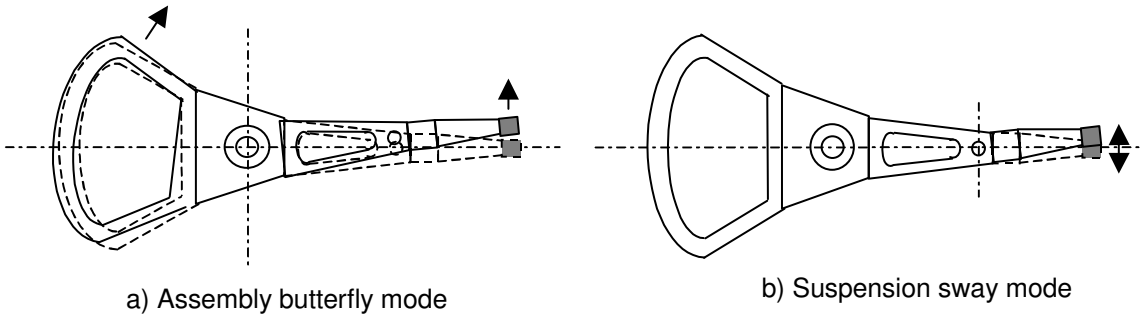

Figure 2.11: Illustration of modes shape of assembly butterfly mode and suspension sway mode.

The torsion modes of the suspension also contribute to head off-track motion. Fig. 2.12 shows the mode shapes of the 1st, 2nd and 3rd torsion modes, as well as the sway mode, of Magnum-5E PZT-actuated suspension obtained by finite element analysis [16].

As shown in Fig. 2.7, the frequency response from VCM input u_1 to head displacement y_1 is dominated by the rigid body mode in the low frequency range and the structural vibration modes in the high frequency range. Fig. 2.8 shows that the PZT actuator can excite the VCM actuator butterfly mode through the swage connection with the E-block arm.

As shown in Figs. 2.9-2.10, the PZT sensor can pick up most of the off-track

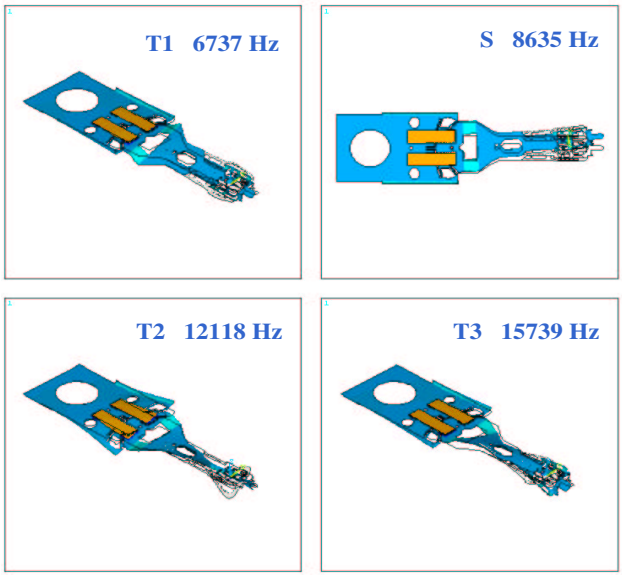

Figure 2.12: Magnum-5E vibration modes (FEA) (Courtesy of H. Gross, UC, Berkeley).

vibration modes of the head stack and suspension assembly when they are excited by the control inputs. The PZT sensor does not sense the rigid body mode, as expected. However, the PZT sensor picks up some non-off-track modes near 3 kHz (M5 and M6 in Figs. 2.9-2.10), which have little effect on the head off-track motion. These modes are probably related to the bending modes of the suspension and they are excited by the airflow disturbances in the out-of-the-plane direction. They act as noise modes to the control system.

2.3.2 Modal Parameters Extraction

The modal parameters, ζ_n, ω_n, A_n^{ij}, $n = 1, ..., N$, $i, j = 1, 2$, in Eq. (2.24) can be extracted from the measured frequency responses using modal testing techniques, such as peak-magnitude method or circle-fit method [12]. The peak-magnitude method is a simple single-degree-of-freedom (SDOF) modal testing method. Assuming the resonance frequen-

cies of each resonance mode are not closely spaced, and the modes are lightly damped, then the response near each resonance frequency is dominated by one resonance mode. Thus, modal parameters can be estimated for that mode by neglecting the effects due to the other modes.

Three modal parameters need to be estimated for each resonance mode, the natural frequency ω, the damping factor ζ, and the modal constant K. For a lightly damped resonance mode, the natural frequency ω is approximately equals to the resonance frequency ω_r,

$$\omega \approx \omega_r. \tag{2.25}$$

The damping ratio can be estimated from the so called "half-power" or "-3dB-magnitude" points by

$$\zeta \approx \frac{\omega_a - \omega_b}{2\omega_r}\,, \tag{2.26}$$

where ω_a and ω_b are the frequencies at which the magnitudes of the frequency response are $1/\sqrt{2}$ of the peak magnitude at the resonance frequency, as shown in Fig. 2.13a. The modal constant can then be estimated by

$$K \approx 2h_r\zeta\,, \tag{2.27}$$

where h_r is the magnitude of the frequency response at the resonance frequency.

For modal testing of multiple resonance modes, the modal parameters of the biggest resonance peak are estimated first. The frequency response of this mode can then be estimated and subtracted from the overall frequency response. The above process repeats until all major modes are identified.

The frequency response from the PZT actuator input to the head displacement,

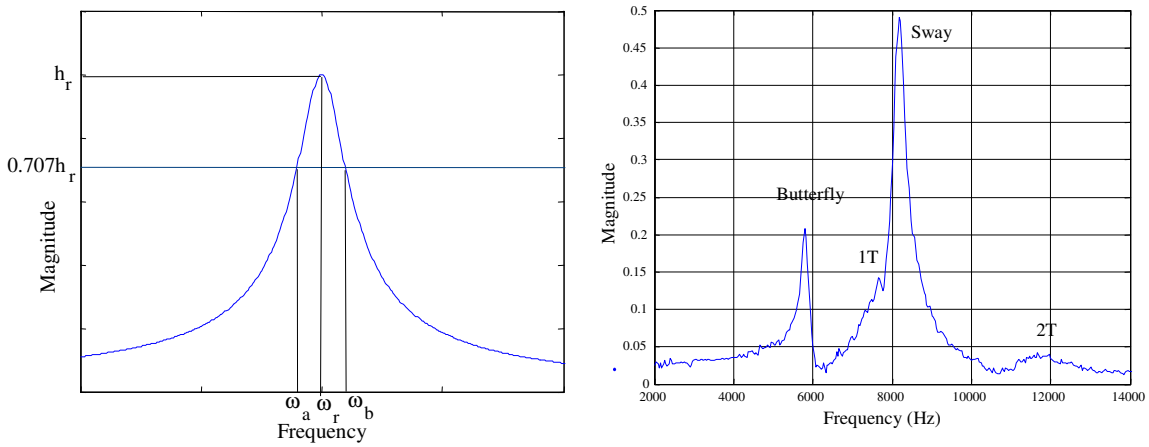

Figure 2.13: Modal testing using the peak-magnitude method.

which is shown in Fig. 2.13b in linear magnitude, is the cleanest of the four measured responses, and therefore is used to estimate the natural frequencies, ω_n, and the damping factors, ζ_n, of the resonance modes of the dual-stage actuator. Three modes, the butterfly mode (M1), the suspension sway mode (M2), and the suspension 2nd torsion mode (M3), were included in the modal analysis.

From two inputs to two outputs, there are 4 modal constants, K_n^{11}, K_n^{12}, K_n^{21}, and K_n^{22}, for each mode. Note that only three of them are independent. K_n^{12}, K_n^{21}, and K_n^{22} were estimated by using Eq. (2.27) based on the measured frequency responses in Figs. 2.8-2.10. K_n^{11} can not be directly estimated from the frequency response in Fig. 2.7 due to the coupling of the rigid body mode. Instead it was calculated by

$$K_n^{11} = K_n^{21} * K_n^{12}/K_n^{22}, \ n = 1, 2, 3. \tag{2.28}$$

The signs of the modal constants can be determined in two ways: by matching the locations

of the zeros, or by matching the phase of the frequency responses.

Table 2.1 lists all modal parameters extracted using this method.

Table 2.1: Extracted modal parameters

Parameters	Mode 1	Mode 2	Mode 3
natural frequency ω_n (Hz)	5900	8400 (FEA: 8635)	11500 (FEA: 12118)
damping factor ζ_n	0.022	0.023	0.035
modal constant from u_1 to y_1, K_n^{11}	-0.04	0.0098	0.0048
modal constant from u_2 to y_1, K_n^{12}	0.005	0.016	0.003
modal constant from u_1 to y_2, K_n^{21}	-0.32	0.11	0.08
modal constant from u_2 to y_2, K_n^{22}	0.04	0.18	0.05

Finally, the feedthrough term d_{ij} can be estimated by matching the DC gains of the measured frequency responses. The feedthrough terms from u_1 and u_2 to the head displacement y_1 were found to be zero, $d^{11} = 0$, $d^{12} = 0$, as expected. There exist direct feedthrough from inputs to the PZT sensor output as discussed in section 2.1. The feedthrough terms from u_1 and u_2 to y_2 were found to be, $d^{21} = 0.16$, $d^{22} = 0.77$.

Due to the effects of the flexible printed cable and pivot friction, the rigid body mode of the VCM can be modeled as a mass-spring-damper system instead of a double integrator. The natural frequency, damping factor and modal constant were found to be ω_0 = 160 Hz, $\zeta_0 = 0.25$, and $K_0^{11} = 3.6e7$. The excitation to the rigid body mode by the PZT actuator is small and can be neglected, thus $K_0^{12} = 0$. The PZT sensor can not sense the rigid bode mode, thus $K_0^{21} = K_0^{22} = 0$.

There are good matches between the experimentally measured frequency responses (the solid lines in Figs. 2.7-2.10) and the simulated frequency responses of the transfer functions in Eq. (2.24) using the extracted modal parameters (the dashed lines in Figs. 2.7-2.10), verifying that the extracted modal parameters are accurate.

Using the identified modal parameters, the control system can be represented as either a decoupled SISO or coupled MIMO model for controller designs:

- In the decoupled SISO representation, the VCM and the PZT actuator dynamics are modeled separately by their transfer functions. The decoupled dual-stage controller design in Chapter 3 is based on this model.

- In the coupled MIMO representation, the dual-stage actuator is modeled as a true MIMO system. In Chapter 3, representation of parametric uncertainty of this coupled MIMO plant model will be discussed. In Chapter 4, the state feedback damping controller is designed based on a state-space realization of the MIMO plant model.

Chapter 3

Track-Following Controller Design of the PZT-Actuated Suspension Dual-Stage Servo System

This chapter discusses track-following control design for the PZT-actuated suspension dual-stage servo system. The considered plant is dual-input single-output (DISO). An overview of the dual-stage controller design methodologies and structures is introduced. Two control designs are presented and compared. The first is designed using decoupled classical SISO frequency shaping design method. The second is designed using the μ-synthesis robust controller design method. Modeling and representation of model uncertainties are presented. The robustness of decoupled SISO design is analyzed using μ-analysis. Experimental results are presented.

3.1 Overview of Dual-Stage Control Design Methodologies

Various control design architectures and methodologies have been developed for control design of dual-stage servo systems. They can be largely classified into two categories: those based on decoupled or sequential single-input single-output (SISO) designs, and those based on modern optimal design methodologies, such as LQG, LQG/LTR, H_∞, and μ-synthesis.

Two constraints must be considered in the dual-stage servo control design. First, the contribution from each actuator must be properly allocated. Usually, the first-stage actuator, or the coarse actuator, has a large moving range, but a low bandwidth, while the second-stage actuator, or the fine actuator, has a high bandwidth, but small moving range. Second, the destructive effect, in which the two actuators fight each other by moving in opposite directions, must be avoided.

3.1.1 Classical SISO Design Methodologies

Several architectures and design methodologies have been proposed to transform the dual-stage control design problem into a decoupled or sequential multiple SISO compensators design problem, for example, master-slave design, decoupled design [40], PQ method [51], and parallel design by sequential loop-closing [52]. Fig. 3.1 to Fig. 3.4 show the block diagrams of dual-stage controller designs using these methods. In these figures, G_1 and G_2 represent the coarse actuator (VCM) and fine actuator (microactuator) respectively. x_1 denotes the position of the coarse actuator. x_r denotes the position of the fine actuator relative to the coarse actuator. x_p denotes the total position output. r denotes the reference

input (runout), and e denotes the position error, $e = r - x_p$.

Master-slave Design Method

In a traditional master-slave structure, the absolute position error is fed to the fine actuator, and the output of the fine actuator is fed to the coarse actuator, as shown in Fig. 3.1. The position error is first compensated by the high bandwidth fine actuator. The coarse actuator will follow the fine actuator to prevent its saturation.

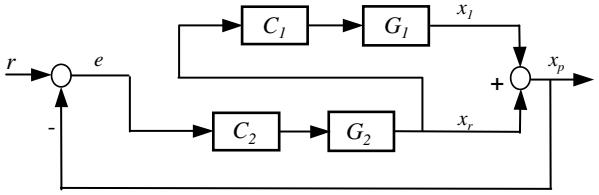

Figure 3.1: Master-slave design structure.

Decoupled Design Method

Fig. 3.2 shows a decoupled design structure [40], which is similar to the master-slave structure. A summation of the fine actuator output and the position error, which equals the position error of the coarse actuator, is fed to the course actuator. A nice feature of this structure is that the control system is decoupled into two independent control loops, and the total closed-loop sensitivity function is the product of the sensitivity functions of each of the control loops. Thus, the two compensators C_1 and C_2 can be designed independently. This method is also referred to as decoupled master-slave design method, or sensitivity function decoupling design method. Details of track-following controller design using this method will be further discussed in section 3.2.

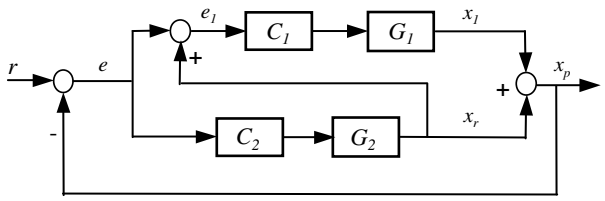

Figure 3.2: Decoupled control design structure.

Both the master-slave and the decoupled designs use the relative position of the fine actuator, x_r. If a relative position sensor is unavailable, x_r can be estimated using a model of the fine actuator.

PQ Design Method

The PQ method is another innovative design technique for control design of dual-input, single-output systems [51]. A block diagram of dual-stage controller design using this method is shown in Fig. 3.3.

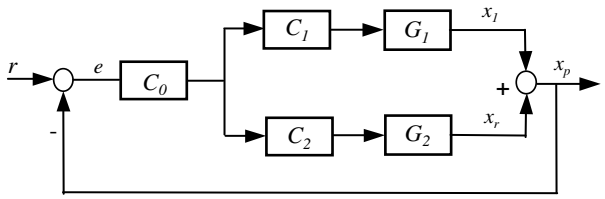

Figure 3.3: PQ control design structure.

In the PQ design, P is defined by

$$P = \frac{G_1}{G_2}\,, \tag{3.1}$$

and a dual-stage controller can be designed in two steps. The first step involves the design

of an auxiliary compensator Q for plant P, which is defined by

$$Q = \frac{C_1}{C_2}\,. \tag{3.2}$$

Q is designed to parameterize the relative contribution of the coarse and fine actuators. The 0 dB crossover frequency and phase margin of the open-loop transfer function PQ are the design parameters in the design of Q. At frequencies below the 0 dB crossover frequency of PQ, the output is dominated by the coarse actuator, while at frequencies above the 0 dB crossover frequency, the output is dominated by the fine actuator. At the 0 dB crossover frequency, the contributions from the two actuators are equal. A large phase margin of PQ will ensure that the two actuators will not fight each other when their outputs are close in magnitude, thus avoiding any destructive effects.

The second step in the PQ design methodology is to design a compensator C_0 for SISO plant PQ such that the bandwidth, gain margin, phase margin, and error rejection requirements of the overall control system are satisfied.

Parallel Design by Sequential Loop Closing

It is also possible to design the dual-stage controller directly using a parallel structure, as shown in Fig. 3.4, by imposing some design constraints and by sequential loop closing [52].

The two constraints for parallel design in terms of the open-loop transfer functions are [52]:

$$C_1(s)G_1(s) + C_2(s)G_2(s) \to C_2(s)G_2(s), \tag{3.3}$$

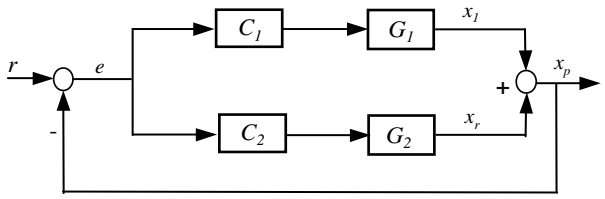

Figure 3.4: Parallel control design structure.

at high frequencies and

$$|C_1(s)G_1(s) + C_2(s)G_2(s)| \gg |C_2(s)G_2(s)|, \tag{3.4}$$

at low frequencies. The first constraint implies that the open-loop frequency response of the dual-stage control system at high frequencies approximately equals that of the fine actuator control loop. Thus, the compensator $C_2(s)$ can be first designed independently as a SISO design problem to satisfy the bandwidth, gain margin, and phase margin requirements of the dual-stage control system. The second constraint ensures that the fine actuator will not be saturated. Compensator $C_1(s)$ can then be designed for the SISO plant model with the fine actuator control loop closed, such that the low frequency constraint and overall stability requirement are satisfied. This model is defined by:

$$G(s) = \frac{G_1(s)}{1 + C_2(s)G_2(s)}\,. \tag{3.5}$$

3.1.2 Modern MIMO Design Methodologies

Since the dual-stage actuator servo system is a MIMO system, it is natural to utilize modern MIMO optimal design methodologies, such as LQG, LQG/LTR, H_∞, and μ-synthesis, to design the dual-stage controller. Usually MIMO optimal designs are based

on the parallel structure shown in Fig. 3.4, augmented with noise/disturbances models and other weighting functions to specify the control design performance objectives.

Linear quadratic Gaussian (LQG) control combines a Kalman filter and optimal state feedback control based on the separation principle. However, the Kalman filter weakens the desirable robustness properties of the optimal state feedback control. Linear quadratic Gaussian / loop-transfer recovery (LQG/LTR) control recovers robustness by a Kalman filter redesign process. Dual-stage control designs using LQG and LQG/LTR have been reported in [63], [55], [24], [54], etc.

The LQG design methodology minimizes the H_2 norm of the control system, while the H_∞ design methodology minimizes the H_∞ norm of the control system. μ-synthesis design methodology is based on the H_∞ design and accounts for plant model uncertainties during the controller synthesis process. Dual-stage control designs based on the H_∞ and μ-synthesis design methodologies have been reported in [55], [18], [49], etc. Track-following controller design using μ-synthesis will be presented in section 3.3.

Other advanced control theories also have been applied to dual-stage servo control designs, such as sliding mode control [34], neural networks [50], etc.

3.1.3 Disk Drive Servo Control Design Specifications

Traditional robustness and performance specifications of typical disk drive servo control designs include

- Gain and phase margins: to have enough stability robustness, usually a gain margin larger than 6 dB and a phase margin larger than 35° are required for disk drive servo

control systems.

- Bandwidth: bandwidth is often characterized by the open-loop gain crossover frequency. For single-stage actuator servo systems, the achievable bandwidth is limited by high-frequency resonance modes to within about 1 kHz . Dual-stage actuator servo systems can achieve more than 2 kHz bandwidth.

- Sensitivity function maximum peaking: to minimize the amplification of disturbance/noise by the servo system, the maximum peak of the sensitivity function is usually required to be less than 6 dB.

These design specifications can be conveniently checked by examining the Nyquist plot of the open-loop system as shown in Fig. 3.5

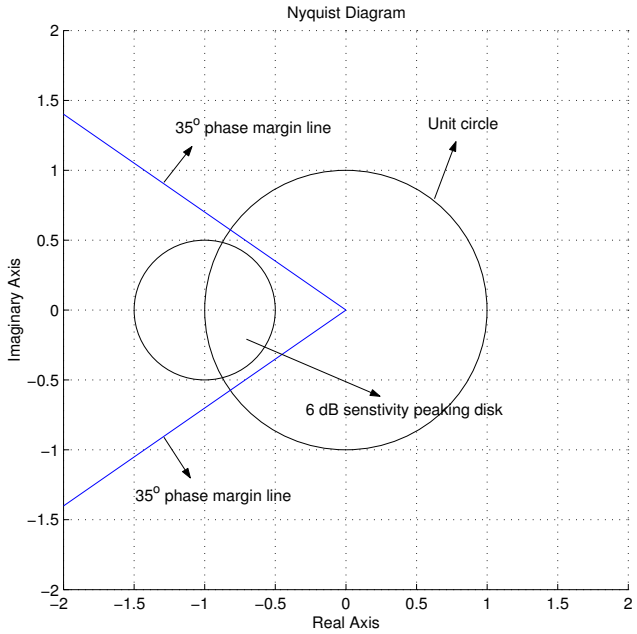

Figure 3.5: Design specifications using Nyquist plot of the open-loop system.

To satisfy the phase margin requirement, the Nyquist curve must enter the unit-circle from the right hand side of the phase margin lines. It cannot enter the disk centered at $(-1, 0)$ with a radius of 0.5 to satisfy the gain margin and sensitivity function peaking requirements.

3.2 Decoupled Dual-Stage Controller Design

The dual-stage controller design that will be discussed in this section is based on the decoupled master-slave method. It helps us to understand the dual-stage control design problem and serves as a reference to which the robust μ-synthesis design will be compared.

3.2.1 Decoupled Master-Slave Controller Design Methodology

Fig. 3.6 shows a block diagram of the dual-stage controller design using decoupled master-slave method. For simplicity, the PZT-actuated suspension will be referred to as the microactuator (MA) in this dissertation. In Fig. 3.6, G_{VCM} and G_{MA} represent the VCM and microactuator models, respectively. K_{VCM} and K_{MA} represent the VCM and microactuator loop controllers, respectively. r denotes the track runout. x_p and x_v denote the positions of the head and the VCM, respectively. PES denotes the position error between the head and the track. $RPES$ denotes the position of the head (microactuator) relative to the VCM. We have

$$PES = r - x_p = r - x_v - RPES \tag{3.6}$$

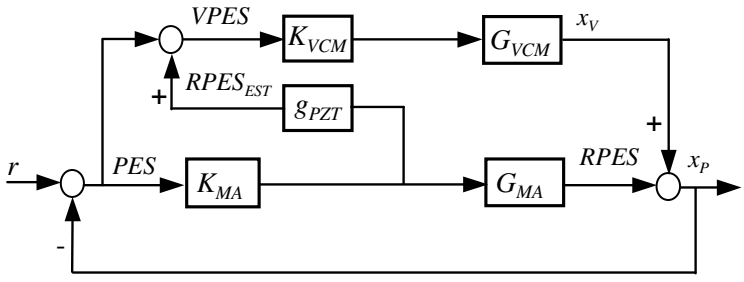

Figure 3.6: Block diagram of the track-following controller design using decoupled master-slave method

The decoupled master-slave control approach utilizes the PES and the $RPES$ signals to generate the position error of the VCM relative to the track, which will be labeled as $VPES$,

$$VPES = PES + RPES = r - x_v, \tag{3.7}$$

and this signal is fed to the VCM loop compensator to decouple the control system [40].

First lets assume $RPES$ is available. The open-loop transfer function from r to x_p with PES feedback loop open in Fig. 3.6 is

$$G_{TO} = K_{VCM}G_{VCM} + K_{MA}G_{MA} + K_{MA}G_{MA}K_{VCM}G_{VCM}\,, \tag{3.8}$$

and

$$1 + G_{TO} = (1 + K_{VCM}G_{VCM})(1 + K_{MA}G_{MA}). \tag{3.9}$$

The closed-loop sensitivity function from r to PES is

$$S_T = \frac{1}{1 + G_{TO}} = S_{VCM}S_{MA}, \tag{3.10}$$

which equals the product of the VCM and microactuator loop sensitivity functions, S_{VCM} and S_{MA}, defined by

$$S_{VCM} = \frac{1}{1 + K_{VCM}G_{VCM}}\,, \tag{3.11}$$

$$S_{MA} = \frac{1}{1 + K_{MA}G_{MA}}\,, \tag{3.12}$$

respectively. It can also be shown that the block diagram in Fig. 3.6 is equivalent to the block diagram shown in Fig. 3.7. It indicates that the runout r is first attenuated by the VCM loop and becomes $VPES$, which is further attenuated by the microactuator loop and becomes PES.

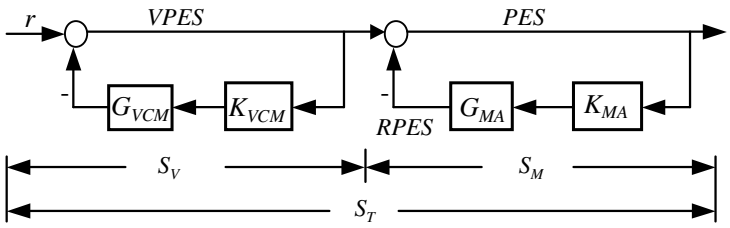

Figure 3.7: Equivalent sensitivity function block diagram.

Thus, the dual-stage servo control design can be decoupled into two independent SISO sensitivity function shaping designs: the VCM loop and the microactuator loop. Dual-stage system stability is guaranteed if each individual loop is stable. The VCM loop sensitivity function can be designed using traditional single-stage servo design methodologies. The microactuator loop sensitivity function is designed to expand the bandwidth of the overall feedback system and provide additional error rejections.

For most PZT-actuated suspensions, $RPES$ is not available. An estimate of it, $RPES_{EST}$, can be obtained by multiplying the PZT control input by the DC gain of the PZT actuator, g_{PZT}. This estimate is accurate in the low frequency range since the dynamics of the PZT actuator can be accurately characterized by a pure gain up to about 4 kHz, as shown in Fig. 2.8. Above this frequency, its dynamics are dominated by the resonance modes. Let ΔG_{MA} denotes the difference between the estimator g_{PZT} and the actual microactuator model, G_{MA},

$$\Delta G_{MA} = g_{PZT} - G_{MA}\,. \tag{3.13}$$

The model error introduces an additional term in the open-loop transfer function in Eq. (3.8): $K_{MA}\Delta G_{MA}K_{VCM}G_{VCM}$. Both K_{MA} and K_{VCM} are designed to have notch filters at resonance frequencies, where the model error is large. Furthermore, the VCM loop gain

crossover frequency is designed to be far less than the resonance frequencies. Thus, the effect of this additional term is small, and the sensitivity function decoupling defined in Eq. (3.10) can be approximated.

The effects on the stability of the control system by this approximation and when there is model uncertainty in g_{PZT} will be analyzed using μ-analysis in section 3.3.

3.2.2 Decoupled Dual-Stage Controller Design Results

VCM Loop

The VCM loop compensator, $K_{VCM}(s)$, was designed to be a simple lead-lag compensator. The lag compensator increases the control gain and error rejection in the low frequency region. The lead compensator boosts the phase margin at the open-loop gain crossover frequency. The transfer function of the lead-lag compensator is

$$K_{vll} = (\frac{s+\omega_{b1}}{s+\omega_{a1}})(\frac{s+\omega_{b2}}{s+\omega_{a2}})\,, \tag{3.14}$$

with corner frequencies chosen to be

$$\omega_{b1} = 500 * 2\pi,\ \ \omega_{a1} = 10 * 2\pi\,,$$

$$\omega_{b2} = 6400 * 2\pi,\ \ \omega_{a2} = 100 * 2\pi\,.$$

A notch filter is cascaded with the lead-lag compensator to attenuate the butterfly mode (5.9 kHz) and the suspension sway mode (8.4 kHz). The transfer function of the notch filter is

$$K_n = \left(\frac{s^2 + 2\zeta_{b1}s + \omega_1^2}{s^2 + 2\zeta_{a1}s + \omega_1^2}\right)\left(\frac{s^2 + 2\zeta_{b2}s + \omega_2^2}{s^2 + 2\zeta_{a2}s + \omega_2^2}\right)\,, \tag{3.15}$$

where

$$\omega_{b1} = 5900 * 2\pi, \;\; \zeta_{a1} = 0.5 \;\; , \zeta_{b1} = 0.02 \, ,$$

$$\omega_{b2} = 8400 * 2\pi, \;\; \zeta_{a2} = 0.1 \;\; , \zeta_{b2} = 0.02 \, .$$

The overall control loop gain was calculated to have an open-loop gain crossover frequency of 800 Hz. The sampling frequency of the control system is 25 kHz. The dashed lines in Figs. 3.8, 3.9, and 3.10 show the Bode plots of the discretized VCM loop controller, open-loop transfer function, and closed-loop sensitivity function, respectively.

PZT Actuator Loop

The PZT actuator loop compensator, $K_{MA}(s)$, was designed to be a lag compensator cascaded with a notch filter similar to the one defined in Eq. (3.15). Since the frequency response of the PZT actuator is almost flat in the low frequency range, a lag compensator is used to provide the control gain for error rejection. The gain crossover frequency of the PZT actuator loop was designed to be much larger than that of the VCM loop at 2500 Hz (1/10 of the sampling frequency). The corner frequency of the lag compensator pole was chosen to be at 10 Hz, and the corner frequency of the lag compensator zero was tuned to be at 2500 Hz to satisfy the overall stability margins and sensitivity function peaking requirements.

The dotted lines in Figs. 3.8, 3.9, and 3.10 show the Bode plots of the PZT actuator controller, open-loop transfer function, and closed-loop sensitivity function, respectively.

Overall Dual-Stage System

The VCM and PZT actuator loop compensators designed above were used in the block diagram of the dual-stage control system depicted in Fig. 3.6. The solid lines in Figs. 3.9 and 3.10 show the Bode plots of the overall open-loop transfer function from r to x_p and the closed-loop sensitivity function, respectively.

Table 3.1 lists the gain margins, phase margins, and gain crossover frequencies of the VCM loop, PZT actuator loop and overall dual-stage systems.

Table 3.1: Summery of decoupled design results

	Gain Margin (dB)	Phase Margin (deg)	Gain c/o freq. (Hz)
VCM loop	10.9	40.5	800
PZT loop	9.7	66.1	2500
Overall	7.4	50.2	2104
Design Specification	6	35	2000

As can be seen from Fig. 3.9, the overall open-loop frequency response near its gain crossover frequency is dominated by that of the PZT actuator loop. A simple tuning process was conducted to satisfy the design specifications by changing the corner frequency of the zero of the PZT actuator loop lag compensator. Increasing this frequency improves the overall gain margin, but reduces the phase margin and increases sensitivity function peaking, and visa versa. It was determined in simulations that an optimal value of this corner frequency is 2500 Hz to satisfy all the gain margin, phase margin and sensitivity function peaking requirements. Fig. 3.11 shows the Nyquist plot of the open-loop system. It is noted that the Nyquist curve is located in the safe region of the Nyquist diagram.

Fig. 3.10 shows the sensitivity function Bode plots of the VCM loop, PZT actuator loop and overall dual-stage system. The unity-gain frequency of the total sensitivity function

is 1490 Hz, and the maximum peaking is 5.0 dB occurring at 4760 Hz. The total sensitivity function of the dual-stage system is approximately the product of the sensitivity functions of the VCM loop and PZT actuator loop. Large attenuation is obtained in the low frequency region with both sensitivity functions attenuating error. However, the overall sensitivity function has less attenuation in the mid-frequency range, from about 700 Hz to about 2 kHz, than that of the PZT actuator loop. This is due to the amplification by the VCM loop sensitivity function over its unity-gain frequency at about 700 Hz. Relatively poor mid-frequency error rejection performance is one drawback of the decoupled master-slave design method.

Fig. 3.12 shows the step response of the dual-stage system. When there is a step reference input, the PZT actuator responds quickly and jumps to the reference step at first. The VCM moves at a lower speed following the reference step and the PZT actuator motion. As the overall position reaches the reference step, the PZT actuator starts to retract slowly back to the original zero position relative to the VCM.

As mentioned before, the dual-stage control design must avoid destructive motion where the two actuators fight each other. The control performance in this regard can be evaluated by checking the phase margin of the PQ transfer function, which is defined as the ratio of the VCM loop and the microactuator loop open-loop transfer functions. To avoid destructive motion, the PQ phase margin must be at least 60° (larger than 90° for best results). The PQ transfer function of decoupled master-slave structure is

$$G_{PQ} = \frac{K_{VCM} G_{VCM} (1 + K_{MA} g_{PZT})}{K_{MA} G_{MA}} . \tag{3.16}$$

Fig. 3.13 shows the Bode plot of this transfer function. The phase margin is

107°. Therefore, destructive motion is avoided. The decoupled master-slave control feeds the output of the microactuator to the VCM loop to follow it. It can inherently prevent destructive motion of the two actuators. The crossover frequency of the PQ plot is 770 Hz. Below this frequency, error is mainly compensated for by the VCM. Above this frequency, it is mainly compensated for by the microactuator.

3.2.3 Experimental Results

The designed controller was implemented using the experimental setup described in Chapter 2, section 2.2. Fig. 3.14 shows the measured and simulated sensitivity function Bode plots. Overall, the experimental data agrees well with the simulation data. The actual sensitivity unity-gain frequency is 1321 Hz (vs. 1490 Hz in the simulation). The actual sensitivity function maximum peaking is 6.3 dB occurring at 3460 Hz (vs. 5 dB occurring at 4760 Hz in the simulation).

Fig. 3.15 shows the head off-track motion before and after the controller is applied. Head off-track motion is 6.1 nm in the 1-σ value when control is applied. Note that because the head position is measured by an LDV in the experimental testing, this result does not reflect the effects on the TMR due to track runout. Fig. 3.16 shows the FFT of the closed-loop head off-track motion. The peak in the 8-9 kHz frequency range is due to the suspension sway mode vibrations excited by the air turbulence. The FFT in the 3-5 kHz range is slightly amplified by the control system due to the sensitivity function peaking.

Fig. 3.17 shows the control signals of the VCM and the PZT actuator. Both are within their saturation limits.

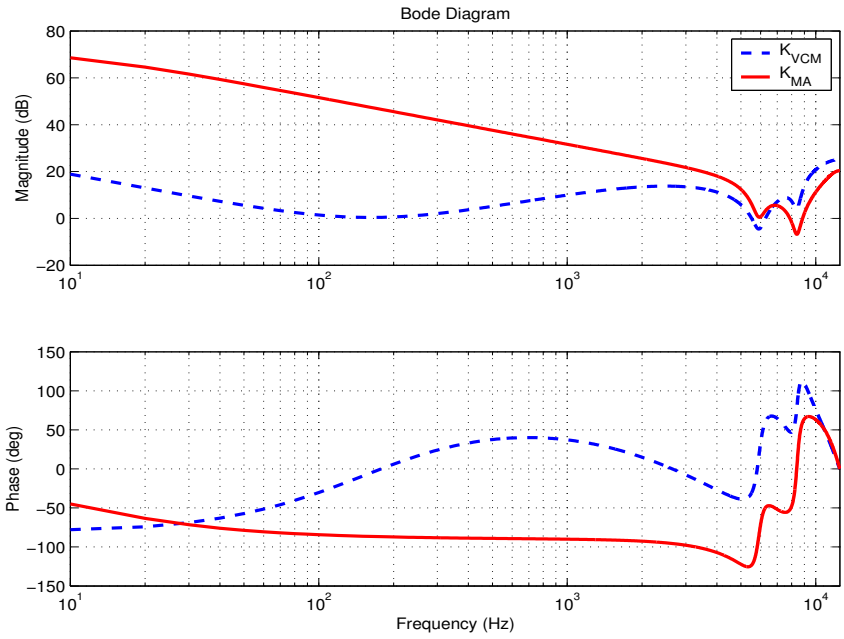

Figure 3.8: Bode plots of VCM loop and MA loop controllers.

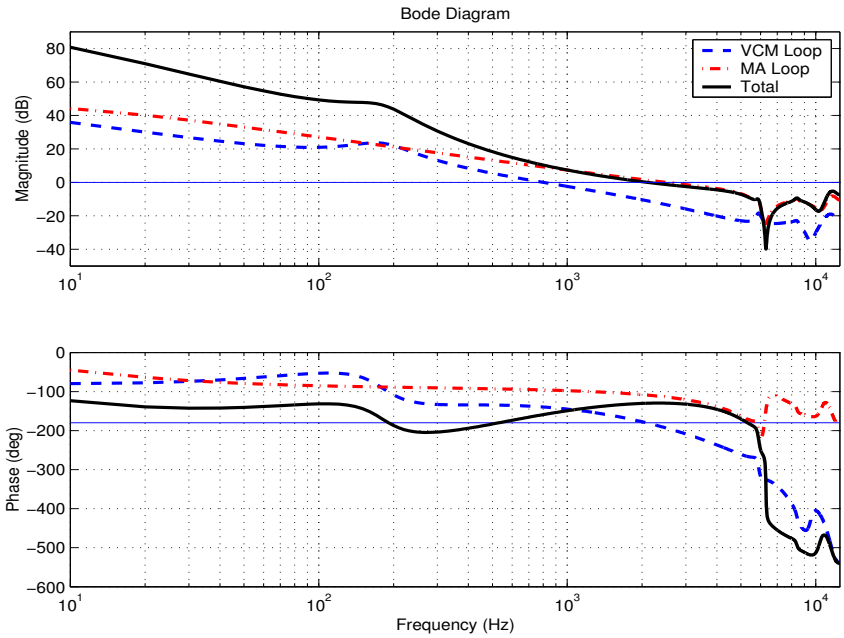

Figure 3.9: Bode plots of the VCM loop, MA loop, and overall open-loop transfer functions.

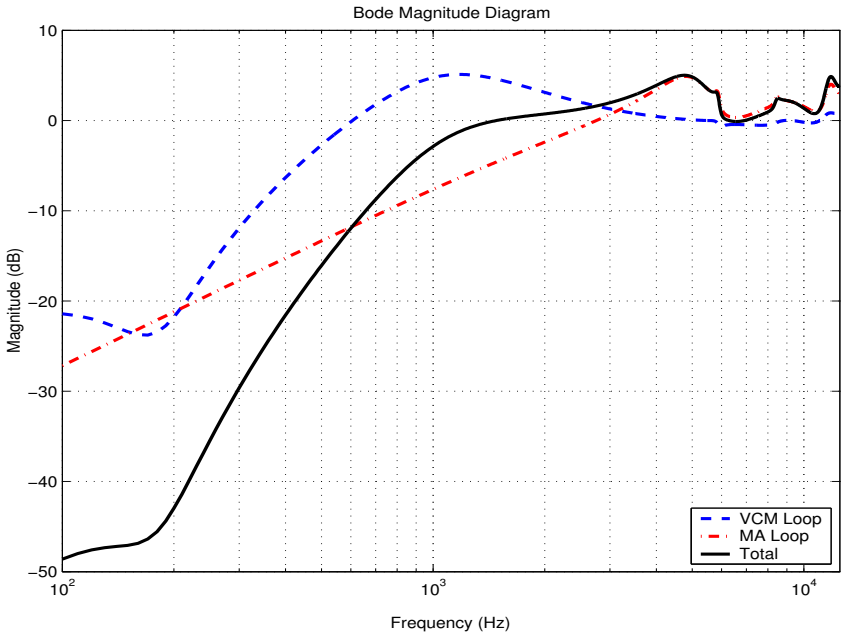

Figure 3.10: Bode plots of VCM loop, MA loop, and overall closed-loop sensitivity functions.

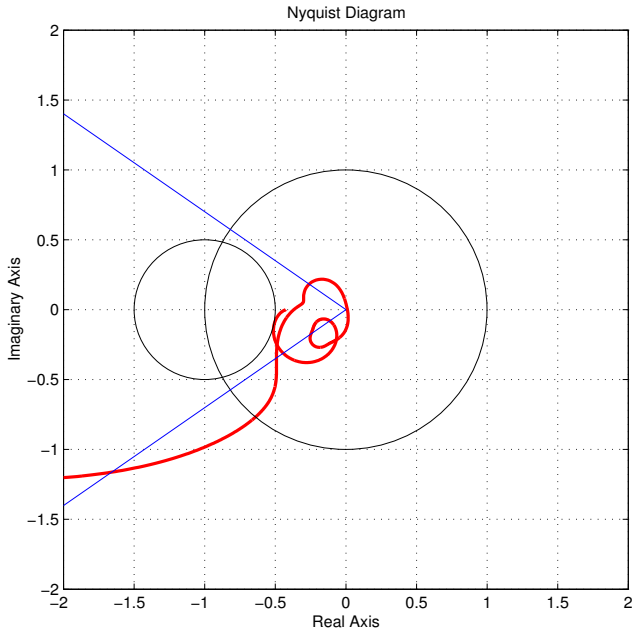

Figure 3.11: Nyquist diagram of the dual-stage open-loop system.

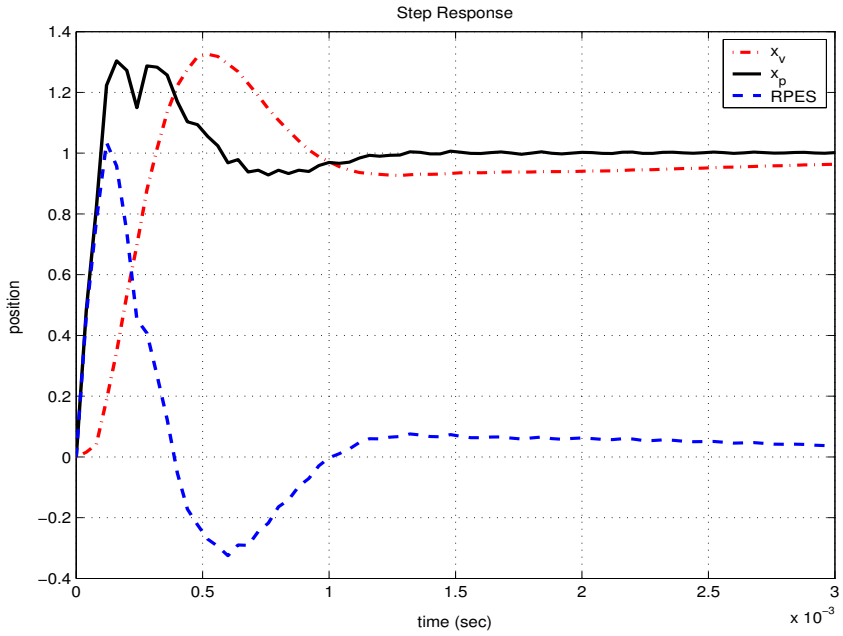

Figure 3.12: Step responses of the dual-stage servo system.

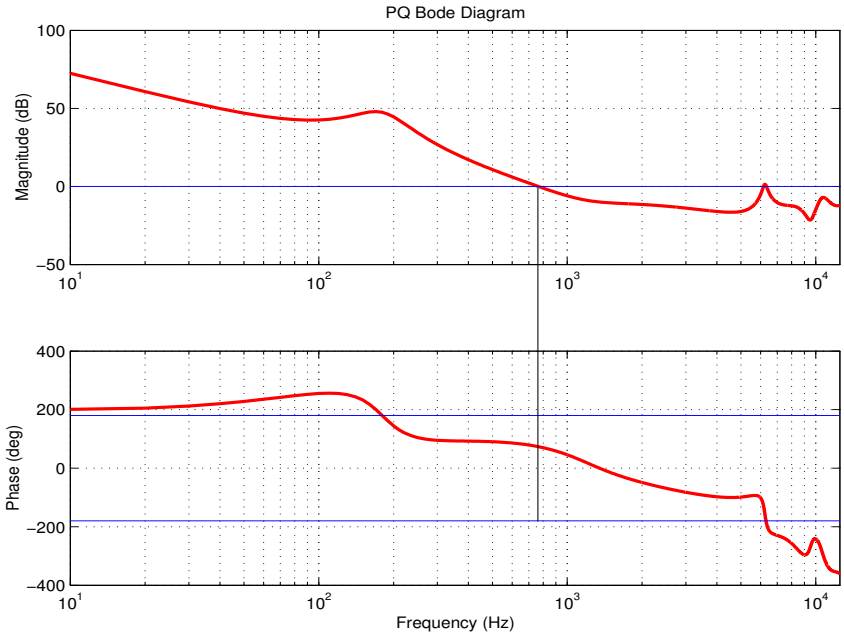

Figure 3.13: PQ plot of the dual-stage system.

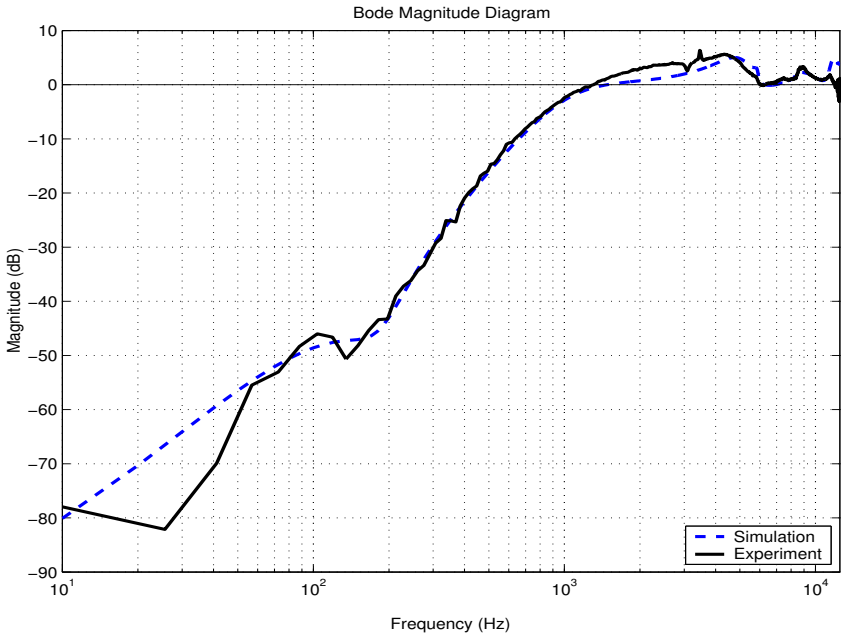

Figure 3.14: Measured sensitivity function Bode plot of the closed-loop system.

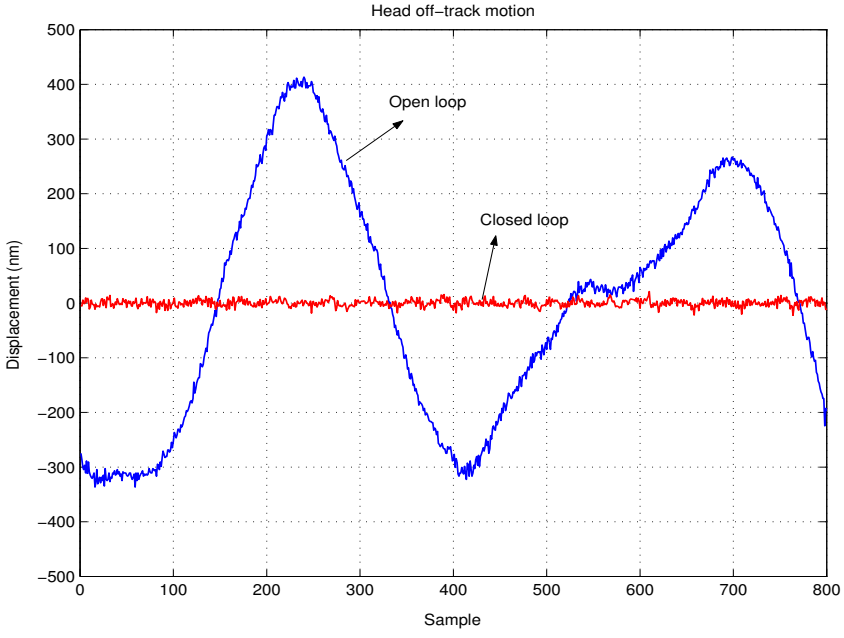

Figure 3.15: Head off-track motion before and after control is applied.

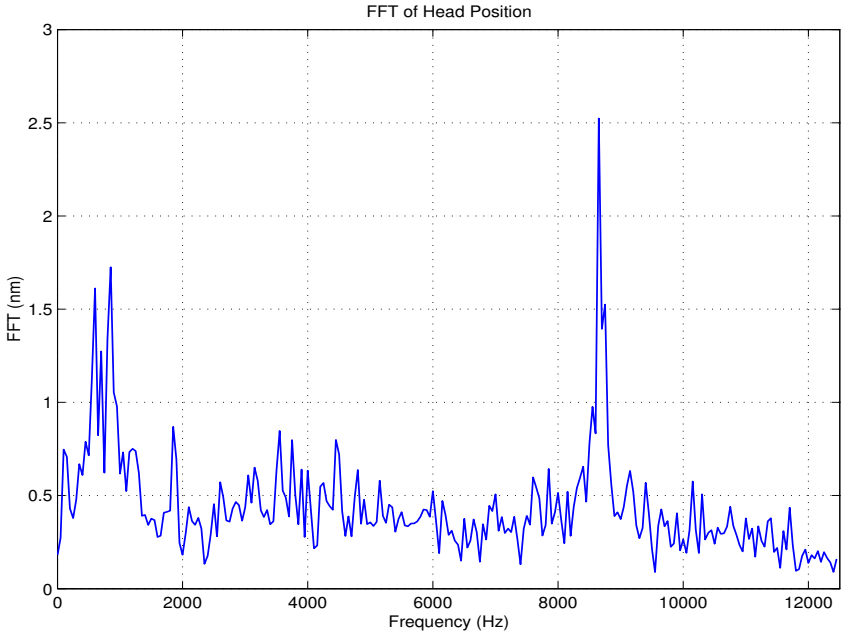

Figure 3.16: FFT of the head off-track motion when control is applied.

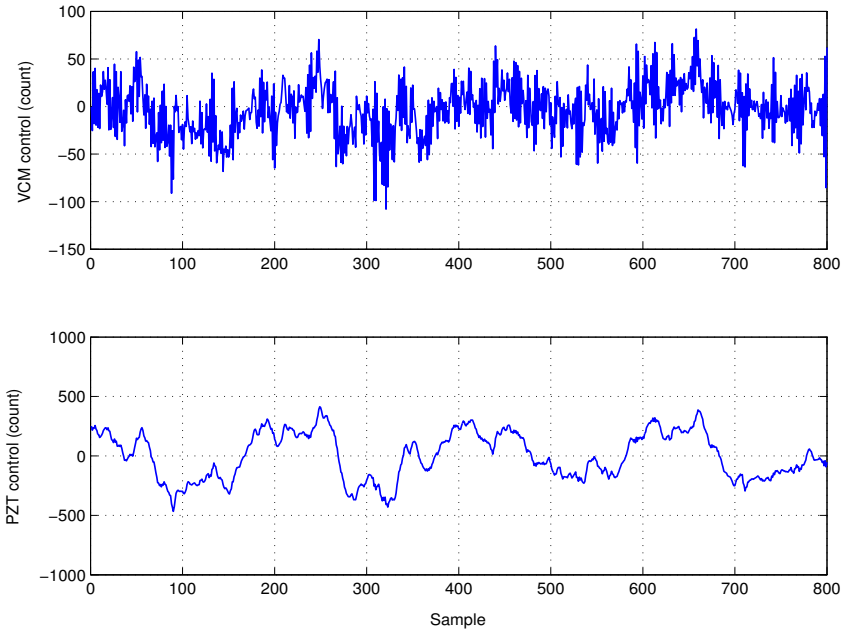

Figure 3.17: Control action of the VCM and the PZT actuator.

3.3 Robust Controller Design and Analysis

The decoupled master-slave method is a simple tool for dual-stage servo control design. However, dual-stage servo systems are MIMO systems with uncertain dynamics. Classical gain/phase margins computed one-loop-at-a-time cannot capture the effects of simultaneous variations in the multiple loops and the cross coupling between them [9]. This section discusses robust control design and analysis of dual-stage servo control systems using μ-Synthesis and μ-Analysis. The representation of structured parametric uncertainty of the PZT-actuated suspension dual-stage system is presented. An overview of structured singular value robust control theory is introduced. Dual-stage controller design using μ-synthesis is presented. The design and experimental results are presented and compared with those obtained using the decoupled master-slave method in the previous section.

3.3.1 Model Uncertainty Representation of the PZT-Actuated Suspension Dual-Stage Servo System

As presented in Chapter 2, the dual-stage plant model can be represented by the summation of the rigid body mode and several structural resonance modes. The natural frequency, damping factor, and the constant of each resonance mode can have some variation from drive to drive. Furthermore, they can change with ambient temperature and humidity. As an example, Tab. 3.2 shows the natural frequency and damping factor of two PZT-actuated suspensions we tested.

For these two test samples, the natural frequency has a 2% variation, and a maximum 5% deviation from the nominal FEA value. The damping factor has a 28% variation.

Table 3.2: Parameters variations of two PZT-actuated suspension test samples

	test sample 1	test sample 2	Nominal (FEA)
Resonance Freq. (Hz)	8400	8220	8635
Damping Factor	0.023	0.018	-

Besides parameter variations, the plant model can have unmodeled dynamics. For example, the 1st torsion and 3rd torsion modes of the PZT-actuated suspension are not included in our model since both of them are small in magnitude and located at high frequencies.

Traditionally, unmodeled dynamics is referred to as unstructured uncertainty, while parametric variations in plant dynamics is referred to as structured uncertainty [9]. In structured singular value (μ) control theory, both can be represented using a structured perturbation matrix.

Representing Parametric Uncertainty using Linear Fractional Transformations (LFT)

The linear fractional transformation (LFT) of the M-Δ interconnect structure shown in Fig. 3.18a is defined as [5]

$$F_L(M, \Delta) = M_{11} + M_{12}\Delta \left(I - M_{22}\Delta\right)^{-1} M_{21}\,. \tag{3.17}$$

Similarly, when the upper loop of M is closed with Δ as shown in Fig. 3.18b the LFT is defined as

$$F_U(M, \Delta) = M_{22} + M_{21}\Delta \left(I - M_{11}\Delta\right)^{-1} M_{12}\,. \tag{3.18}$$

Variation in parameters can be represented by LFTs using real perturbations [5]. Suppose a parameter a has a nominal value of 2 and has a 10% variation (i.e., it takes a

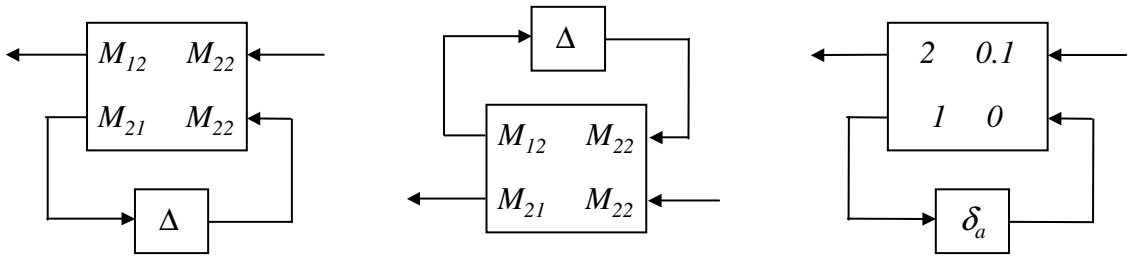

a) M-Δ interconnect system b) Upper loop closed M-Δ system c) Parametric uncertainty LFT

Figure 3.18: Representing parametric uncertainty using LFT.

value in [1.8-2.2]), it can be written as

$$a = 2 + 0.1\delta_a \ , |\delta_a| \leq 1 \, . \tag{3.19}$$

This can be represented by an LFT interconnect shown in Fig. 3.18c. Now check

$$\begin{aligned} a &= F_L \left(\begin{bmatrix} 2 & 0.1 \\ 1 & 0 \end{bmatrix}, \delta_a \right) \\ &= 2 + 0.1 * \delta_a \left(1 - 0 * \delta_a\right)^{-1} * 1 \\ &= 2 + 0.1\delta_a \end{aligned}$$

Consider a single resonance mode defined by

$$G(s) = \frac{b}{s^2 + a_1 s + a_0} \, , \tag{3.20}$$

in which a_0, a_1, and b are parameters related to the natural frequency, damping factor, and modal constant of the mode. An LFT representation of the variations in these three

parameters is shown in Fig. 3.19, in which the diagonal uncertainty matrix, Δ, is defined as

$$\Delta := \begin{bmatrix} \delta_{a_0} & & \\ & \delta_{a_1} & \\ & & \delta_b \end{bmatrix}. \tag{3.21}$$

The augmented uncertain system has 4 inputs (u , w_{a_0} , w_{a_1} , w_b) and 4 outputs (y , z_{a_0} , z_{a_1} , z_b. Inputs (w_{a_0} , w_{a_1} , w_b), outputs (z_{a_0} , z_{a_1} , z_b) and Δ are used to represent the variations in a_0, a_1, and b.

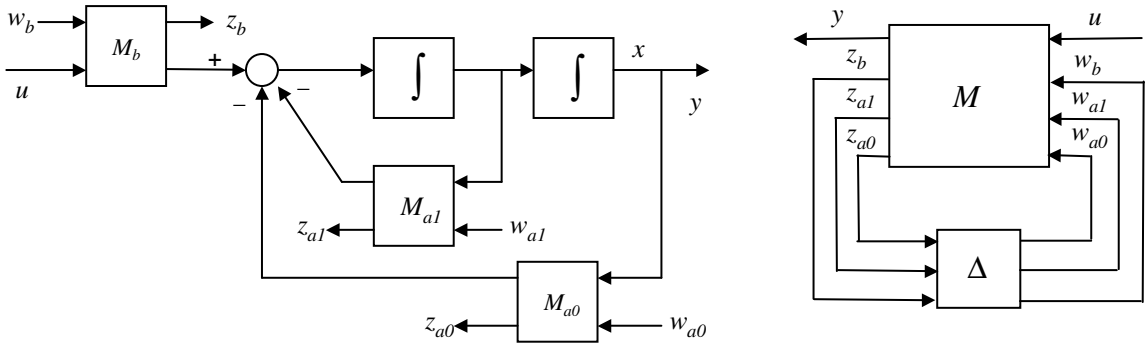

a) Augmented input/output model of an uncertain system

b) LFT of the uncertain system

Figure 3.19: Representing parametric uncertainty of a single resonance mode.

A Coupled Dual-Stage Model with Structured Uncertainty

Fig. 3.20 shows a coupled MIMO model of the PZT-actuated suspension dual-stage actuator, which includes four modes (one pivot friction/flexible cable mode and three structural vibration modes), as discussed in Chapter 2. The output of the system equals the superposition of the output of each mode actuated/excited by the VCM and the PZT actuator. Compared to the dual-stage model by simply adding the transfer functions of

the VCM and PZT actuator used in the previous design [18], a coupled MIMO model is a more precise representation of the dynamics of the system. It can capture the effects of simultaneous parameters variations in both the VCM loop and the PZT actuator loop for robust control design and analysis. It can also prevent excessive modeling, in which the order of the dual-stage system is higher than its actual physical order, resulting from addition of two transfer functions.

This model allows full characterization of parametric uncertainty of the PZT-actuated suspension dual-stage system. There are four parameters associated with each mode, and in total there are 16 uncertain parameters. The sizes of perturbations to these parameters used in our design and analysis are listed in Tab. 3.3

Table 3.3: Perturbations of the uncertain dual-stage actuator model ($i = 0, 1, 2, 3$)

Parameter	Perturbations
Natural frequency ($\sqrt{a_{i0}}$)	10%
Damping factor (a_{i1})	100%
Modal constant, VCM excitation, (b_{i1})	10%
Modal constant, PZT excitation, (b_{i2})	10%

Besides variations in model parameters, there are unmodeled dynamics. A plant model is usually only characterized up to certain frequency and the dynamic behavior of the plant beyond that frequency is unknown. Even in the characterized frequency range, some dynamics are neglected if their effects are small. In our testing, the frequency responses are measured up to 12 kHz. The suspension 1st torsion mode (at around 7 kHz) and 3rd torsion mode (at around 15 kHz) are neglected. Unmodeled dynamics can be represented using multiplicative and additive uncertainty models and complex perturbations, which represent a ball of all possible plants.

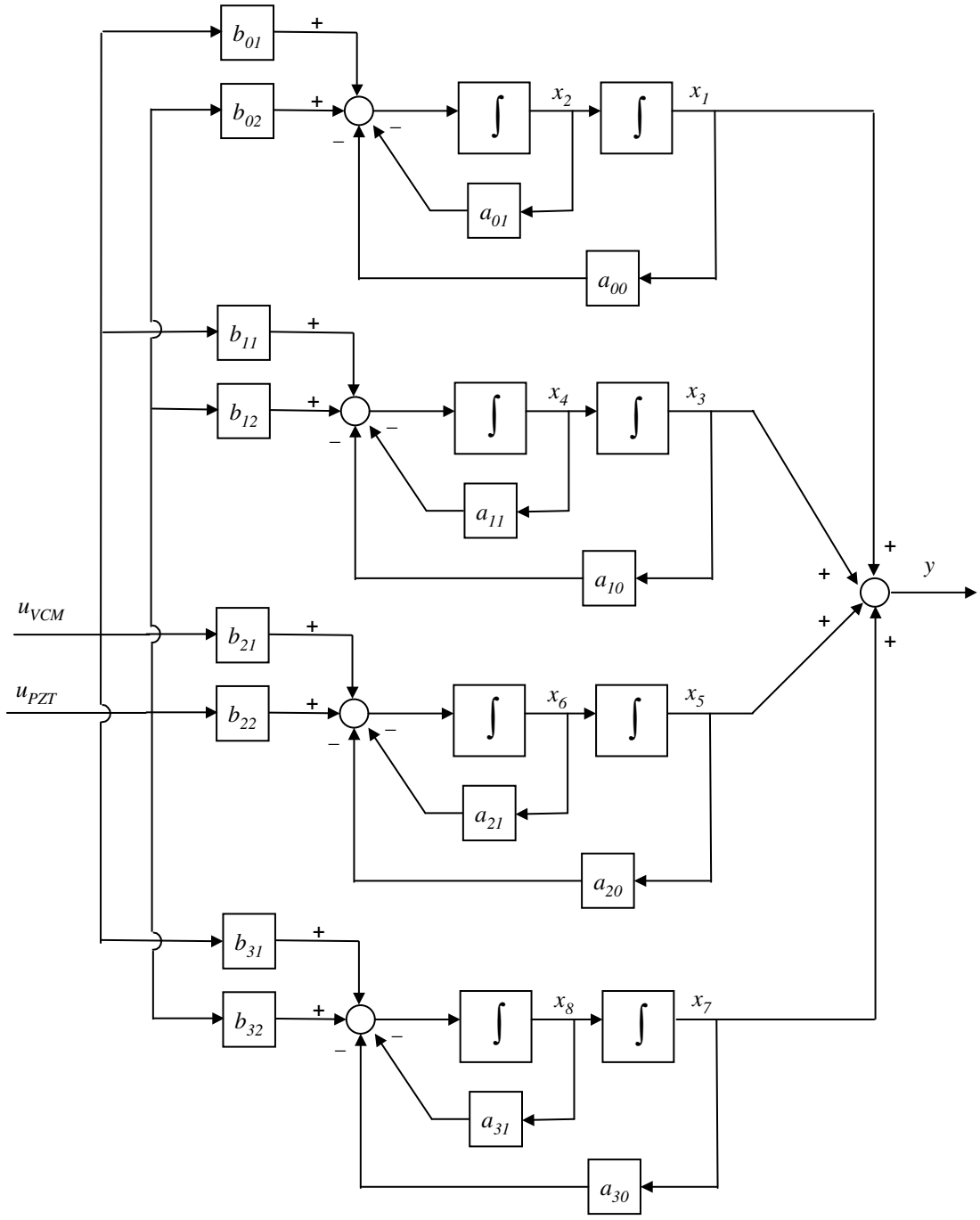

Figure 3.20: Coupled MIMO model of the PZT-actuated suspension dual-stage system.

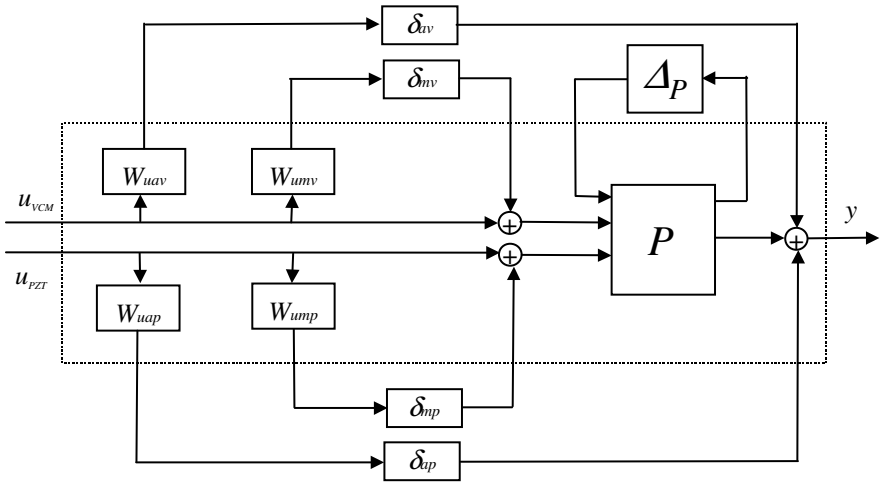

Figure 3.21: Uncertainty plant model of the PZT-actuated suspension dual-stage actuator with multiplicative, additive and parametric uncertainties.

Fig. 3.21 shows the uncertain plant model of the dual-stage actuator including multiplicative, additive and parametric uncertainties. P represents the coupled MIMO plant model depicted in Fig. 3.20, added by 16 parametric uncertainty LFTs. Δ_P represents the parametric uncertainty perturbations, which is a real diagonal matrix. δ_{mv}, δ_{av}, δ_{mp}, and δ_{ap} are complex perturbations representing multiplicative and additive uncertainties from the VCM and PZT actuator inputs, respectively. Define the unmodeled dynamics uncertainty perturbation matrix by

$$\Delta_u = \text{diag}\left(\delta_{mv}, \delta_{av}, \delta_{mp}, \delta_{ap}\right) . \tag{3.22}$$

W_{umv}, W_{uav}, W_{ump}, and W_{uap} are the corresponding uncertainty weighting functions. Even though they can be chosen as dynamic models, constant weighting functions are used in our model for simplicity. By absorbing the weighting functions into the augmented plant model, as shown in the dashed box in Fig. 3.21, multiplicative and additive uncertainties can also be represented in LFT forms. A single structured diagonal perturbation

matrix defined by

$$\Delta = \begin{bmatrix} \Delta_p & 0 \\ 0 & \Delta_u \end{bmatrix}, \tag{3.23}$$

$$\Delta_p = \mathrm{diag}(\delta_i), \delta_i \in \mathbb{R}, i = 1 \ldots 16 \,, \tag{3.24}$$

$$\Delta_u = \mathrm{diag}(\delta_j), \delta_j \in \mathbb{C}, j = 1 \ldots 4 \,, \tag{3.25}$$

can be used to represent both parameters variations and unmodeled dynamics of the PZT-actuated suspension dual-stage actuator model. Note that Δ is a structured block diagonal matrix. The elements of Δ can be real or complex diagonal or full sub-matrices. Compared to using unstructured full complex matrix to represent uncertainty in traditional robust control theory, the structured uncertainties representation is more flexible and accurate. It can represent mixed uncertainties with both real parameters variations and unmodeled dynamics of each component. The unstructured uncertainty at component level becomes structured uncertainty at system level. The structured singular value μ is used to analyze the stability robustness of control systems with structured uncertainties.

3.3.2 Overview of μ-Synthesis and Analysis

In this section, an overview of robust control design and analysis using μ-synthesis is introduced. For more detail of the theories and proofs of μ-synthesis and analysis, please refer to [10] [64] [45] [5] [9].

The Structured Singular Value μ

A general definition of the perturbation matrix Δ is

$$\Delta \in \mathbf{\Delta}, \text{where } \mathbf{\Delta} = \left\{ \text{diag} \left[\delta_1^c I_{c1}, \ldots, \delta_s^c I_{cs}, \delta_1^r I_{r1}, \ldots, \delta_p^r I_{rp}, \Delta_1, , \ldots, \Delta_F \right] \right\},$$

$$\delta_i^c \in \mathbb{C}, \delta_i^r \in \mathbb{R}, \Delta_k \in \mathbb{C}^{m_k \times m_k}. \quad (3.26)$$

The structured singular value μ of the uncertainty M-Δ structure depicted in Fig. 3.18a is defined as

$$\mu_{\mathbf{\Delta}}(M) := \frac{1}{\min\{\bar{\sigma}(\Delta) : \Delta \in \mathbf{\Delta}, \det(I - M\Delta) = 0\}}, \quad (3.27)$$

and $\mu_{\mathbf{\Delta}}(M) := 0$ if $\det(I - M\Delta) \neq 0$ for all $\Delta \in \mathbf{\Delta}$. Basically, μ is the reciprocal of the minimum size of Δ that makes the M-Δ structure become singular. A μ-test in the frequency domain can be used to analyze the stability robustness of dynamic systems.

Robustness Stability and Performance Analysis using μ

For controller robustness analysis, consider the feedback system depicted in Fig. 3.22, in which P_a and K represent the augmented nominal plant model and the controller, respectively. P_a includes plant dynamics and LFTs and weighting functions to represent model uncertainties. The inputs of P_a are the control input u, disturbance d, and uncertainty perturbation input w. The outputs are the measurement y, performance objective e, and perturbation output z.

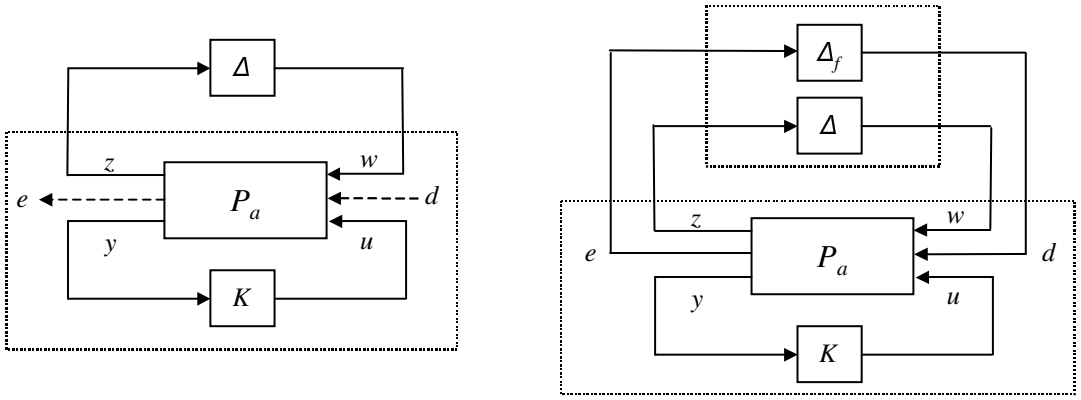

Figure 3.22: Robust stability and performance analysis using μ.

The augmented plant P_a can be written as

$$\begin{bmatrix} z \\ e \\ y \end{bmatrix} = \begin{bmatrix} P_{11} & P_{12} & P_{13} \\ P_{21} & P_{22} & P_{23} \\ P_{31} & P_{32} & P_{33} \end{bmatrix} \begin{bmatrix} w \\ d \\ u \end{bmatrix} . \tag{3.28}$$

The nominal open-loop system when the uncertainty input w and output z are not considered is $G_O = \begin{bmatrix} P_{22} & P_{23} \\ P_{32} & P_{33} \end{bmatrix}$.

For robust stability analysis, the disturbance d and error e are not considered. The closed-loop system is defined using LFT notation by grouping P_a and K together, as shown in the dashed box in Fig. 3.22a, as follows

$$\begin{aligned} G_C &= F_L \left(\begin{bmatrix} P_{11} & P_{13} \\ p_{31} & P_{33} \end{bmatrix}, K \right) \\ &= P_{11} + P_{13}K(I - P_{33}K)^{-1}P_{31} . \end{aligned} \tag{3.29}$$

The robust stability of the closed-loop system G_C subjected to structured perturbation

Δ can be analyzed using a μ-test of the G_C-Δ structure in the frequency domain. First, the frequency response of $G_C(j\omega)$ is calculated. Then, the structured singular value μ is calculated for $G_C(j\omega)$ at each frequency with respect to the uncertainty structure Δ. The structured singular value robust stability theorem is as follows [5] [64]:

The system is well-posed and stable for all $\Delta \in \mathbf{\Delta}$ with $\|\Delta\|_\infty < 1/\beta$ if and only if

$$\sup_{\omega \in \mathbb{R}} \mu_{\mathbf{\Delta}}(G(j\omega)) \leq \beta \,. \tag{3.30}$$

The theorem says that the peak value of μ of the frequency response of the system determines the stability robustness of the closed-loop system. The smaller this value, the larger the size of the perturbation that is needed to make the control system unstable. Typically μ is required to be less than one since signals are usually normalized. The reciprocal of the peak value of μ is called the stability margin of multi-variable control systems [9].

Performance robustness in terms of the H_∞ norm of the closed-loop system can also be analyzed using μ by defining an augmented perturbation matrix as

$$\Delta_P := \left\{ \begin{bmatrix} \Delta & 0 \\ 0 & \Delta_F \end{bmatrix} ; \Delta \in \mathbf{\Delta} \,, \Delta_F \in \mathbb{C}^{n_d \times n_e} \right\} , \tag{3.31}$$

in which Δ_F is a fictitious complex full-matrix perturbation and has compatible dimensions with d and e. Robust performance defined in terms of the H_∞ norm from disturbance d to the performance objective e under perturbation Δ, $\|F_U(G_P, \Delta)\|_\infty$, can be checked by a μ-test in the frequency domain of the G_p-Δ_P structure shown in Fig. 3.22b. The structured singular value robust performance theorem is as follows [5] [64]:

The system is well-posed, stable and $\|F_U(G_P, \Delta)\|_\infty \leq \beta$ for all $\Delta \in \mathbf{\Delta}$ with

$\|\Delta\|_\infty < 1/\beta$ if and only if

$$\sup_{\omega\in\mathbb{R}} \mu_{\mathbf{\Delta_P}}(G_P(j\omega)) \leq \beta\,. \tag{3.32}$$

The theorem says that the robust performance problem is equivalent to the robust stability problem with an augmented uncertainty.

The proofs of both theorems can be found in [5] [64].

μ-Synthesis using D-K Iteration

μ-synthesis is a robust optimal controller design technique to minimize the structured singular value μ. The objective of μ-synthesis is to find a stabilizing controller K minimizing the peak value of μ of the closed-loop system $F_L(P,K)$, i.e.,

$$\min_{\text{Stabilizing}K} \max_{\omega\in\mathbb{R}} \mu_{\mathbf{\Delta}}(F_L(P,K)(j\omega))\,. \tag{3.33}$$

As it turns out, the calculation of μ is usually very difficult, but the calculations of an upper and lower bounds on μ are much easier. For the M-Δ structure shown in Fig. 3.18a, it can be shown that an upper bound of $\mu_\Delta(M)$ is the maximum singular value of an optimally scaled matrix of M [45],

$$\mu_\Delta(M) \leq \inf_{D\in\mathbf{D}_\Delta} \bar{\sigma}(DMD^{-1})\,, \tag{3.34}$$

in which $\mathbf{D}_\Delta$ is the set of matrices that have the property that D and Δ commute, i.e., $D\Delta = \Delta D$. Using this upper bound, the optimization in Eq. (3.33) can be reformulated as [5]

$$\min_{\text{Stabilizing}K} \min_{D(s)\in D_\Delta} \|DF_L(P,K)D^{-1}\|_\infty\,, \tag{3.35}$$

in which $D(s)$ is a stable minimum-phase transfer function whose frequency response approximates the upper bound of μ at each frequency.

D-K iteration is a μ-synthesis tool, which attempts to minimize μ through a two-step iterative process [5]. The first step of D-K iteration is holding $D(s)$ fixed and solving the optimization of

$$\min_{\text{Stabilizing}K} \|DF_L(P,K)D^{-1}\|_\infty . \tag{3.36}$$

By absorbing the D scalers into an augmented plant, this optimization becomes a standard H_∞ optimization control problem.

The second step of D-K iteration is holding K fixed and finding the optimal scaling $D(s)$. First, the lowest upper bound of μ is calculated point-wise in the frequency domain through convex optimization. Then, the optimal frequency-dependent scaling is curve fitted with a stable, minimum-phase, transfer function $\hat{D}(s)$. The estimated scalers $\hat{D}(s)$ and $\hat{D}(s)^{-1}$ will be absorbed into the augmented plant for K optimization in the next iteration.

D-K iteration is the only tool available today to solve robust controller synthesis problems with structured uncertainty, and it has been shown to be effective in many applications. However it cannot guarantee a global or even local minimum. Sometimes, the uncertainty and performance weightings need to be modified in order to get a better solution. Eventually, the synthesized controllers can be analyzed against the original uncertainty and performance weightings to evaluate their robustness and performance.

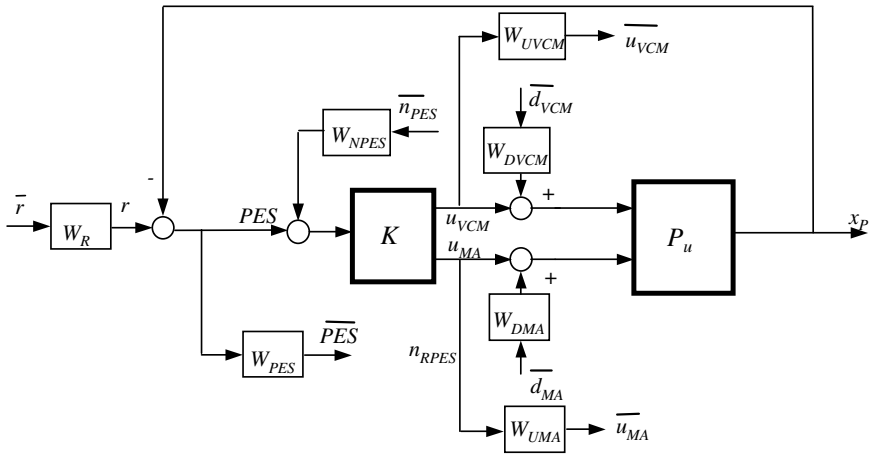

Figure 3.23: Model with weighted inputs and outputs for μ-synthesis controller design.

3.3.3 Track-Following Controller Design Using μ-Synthesis

In order to perform controller design using μ-synthesis, the model uncertainty is represented using linear fractional transformations (LFT), and disturbance inputs and error outputs are weighted to characterize the real plant environment and the performance requirements. We have discussed the uncertainty representation of the PZT-actuated suspension dual-stage servo system in section 3.3.1. Fig. 3.23 shows a weighted model of the dual-stage system used for controller synthesis. In Fig. 3.23, P_u represents the coupled dual-stage plant model with both parametric uncertainty and unmodeled dynamics described in section 3.3.1.

Disturbance input signals accounted for in the model include the runout r, input disturbances to the VCM and microactuator, d_{VCM} and d_{MA}, respectively, and the PES sensor noise n_{PES}. These disturbance signals are generated by passing normalized signals $\overline{r}$, $\overline{d_{VCM}}$, $\overline{d_{MA}}$, and $\overline{n_{PES}}$ through weighting functions W_r, W_{dVCM}, W_{dMA}, and W_{nPES},

respectively.

The output signals in the synthesis model are the head position error signal, PES, the VCM control input u_{VCM}, and the microactuator control input u_{MA}. These signals are multiplied by scaling factors, W_{PES}, W_{uVCM}, and W_{uMA} ,respectively, to produce the weighted performance signals $\overline{PES}$, $\overline{u_{VCM}}$, and $\overline{u_{MA}}$.

Given a set of input and output weights and plant uncertainties, if the synthesized controller achieves

$$\mu \leq \beta \,, \tag{3.37}$$

the closed-loop transfer function, $\overline{T}$, from the normalized disturbances

$$\overline{d} = \left[\overline{r}\ \overline{d_{VCM}}\ \overline{d_{MA}}\ \overline{n_{PES}}\right] \tag{3.38}$$

to the weighted performance signals

$$\overline{e} = \left[\overline{PES}\ \overline{u_{MA}}\ \overline{u_{VCM}}\right] \tag{3.39}$$

will have an infinity norm

$$\| \overline{T} \|_\infty \leq \beta \tag{3.40}$$

for perturbations

$$\| \Delta \|_\infty < \frac{1}{\beta} \,, \tag{3.41}$$

where Δ is defined in Eq. (3.23)

The H_∞ norm can be interpreted as the RMS gain of the sinusoidal signals. Assume that each element $\overline{d_i}$ of the disturbance input vector in Eq. (3.38) is a sinusoid of the form

$$\overline{d_i}(t) = D_i \sin(\omega_i t + \psi_i) \,, \tag{3.42}$$

such that

$$\sum_{i=1}^{4} D_i^2 \leq 1\,. \tag{3.43}$$

Then the steady state response of output in Eq. (3.39) will also be a sinusoid of the form

$$\overline{e_i}(t) = E_i \sin(\omega_i t + \phi_i)\,, \tag{3.44}$$

and

$$\sum_{i=1}^{3} E_i^2 \leq \beta\,, \tag{3.45}$$

under the perturbations defined in Eq. (3.41).

The H_∞ design can also be interpreted as frequency loop-shaping design using weighting functions, as described in the next section.

Weighting Functions for μ-Synthesis Design

In our design, the output weights W_{PES}, W_{uVCM}, and W_{uMA} were chosen to be constant gains, in order to limit the magnitude of the error signals within acceptable bounds. W_{PES} was chosen to be 1/(10 nm), which implies that the TMR target is 10 nm. W_{uVCM} and W_{uMA} must be chosen to bound the control input signals to be within their saturation limits. They both are equal to 1/(2 V), since the DAC outputs saturation limits are $\pm$2 V.

The input weights, W_{dVCM} and W_{dMA} were chosen to be 2 mV at the DAC outputs, respectively, and W_{nPES} was chosen to be 2 nm. The runout weight W_r was chosen in combination with W_{PES} to shape the closed-loop sensitivity function. If the designed control system achieves a peak μ value of β, we have,

$$\|W_{PES} S W_r\|_\infty \leq \beta\,, \tag{3.46}$$

where S is the closed-loop sensitivity function from runout r to PES. Define the desired closed-loop sensitivity function to be

$$S_N = \frac{1}{W_{PES} W_r} \,. \tag{3.47}$$

If $\beta < 1$, the magnitude of the Bode plot of S will be bounded below by that of S_N.

The performance specifications of the closed-loop sensitivity function used in the design are

- Maximum peaking less than 6 dB.
- Sensitivity unity-gain frequency larger than 1200 Hz.
- Low frequency attenuation larger than 60 dB

Based on these criteria, W_r was designed to have two poles at $1200 * 2\pi(1 \pm j)$, and two zeros at $30 * 2\pi$. The Bode plot of the resulting S_N defined in Eq. (3.47) is shown in Fig. 3.24.

3.3.4 Controller Synthesis Results

Controllers were synthesized using D-K iteration of the μ-synthesis Matlab Toolbox. In order to reduce the order of the synthesized controllers, constant D-scalings were used during μ upper-bound fittings in the D-K iteration. The synthesized controller is 10th order. Simulations show its performance is sensitive to further model reduction. Since 10th order is not particularly high, this synthesized controller was used directly in the simulation and experimental testing without further model reduction.

As we mentioned earlier, D-K iteration cannot guarantee that the synthesized controller achieves the minimum structured singular value given the uncertainty and per-

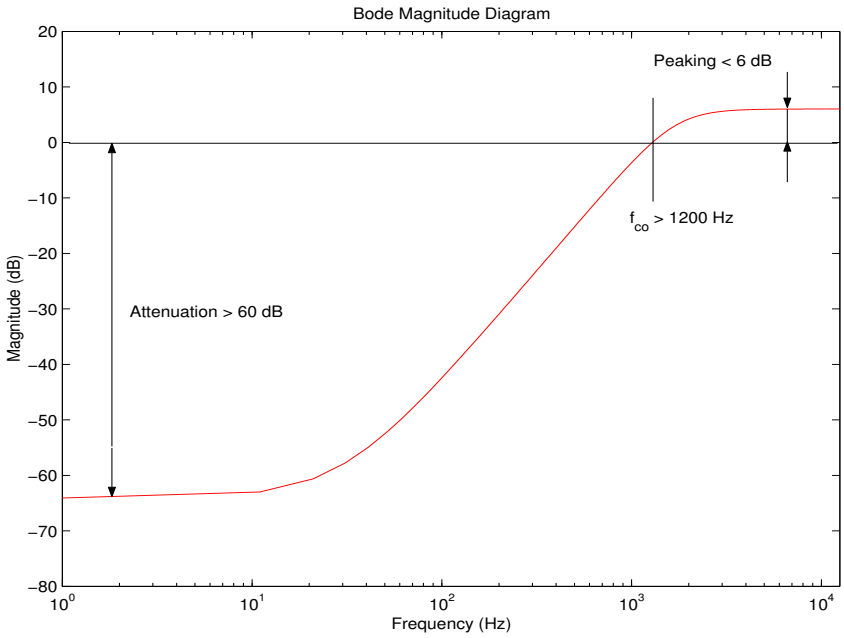

Figure 3.24: Sensitivity function frequency shaping design.

formance weightings. In our design, we found that the synthesized controller using the original uncertainty and performance weightings turned out to be very conservative. After some trial-and-error, a better design was obtained by relaxing some of the uncertainty constraints. The synthesized controller was analyzed using the original uncertainty and performance specifications. The results show that it can achieve a much better error rejection performance with only a small degradation in the robustness.

Fig. 3.25 shows the μ bounds for robust stability and robust performance tests of the closed-loop system using this controller with respect to the original uncertainty representations. The robust stability (RS) and robust performance (RP) peak μ values are, $\beta_{RS} = 0.45$ and $\beta_{RP} = 1.26$, respectively. Thus, the control system is stable for the prescribed uncertainties. In the worst case, the magnitude of the sensitivity function of

the uncertain system is 26% larger than that of the desired nominal sensitivity function. Fig. 3.26 shows the sensitivity function Bode plot of the nominal system with the synthesized controller. The unity-gain frequency of the sensitivity function is 1450 Hz (design objective: larger than 1200 Hz), and the maximum peak is 4.1 dB (design objective: less than 6 dB).

Fig. 3.27 shows the Bode plots of synthesized VCM loop and PZT actuator loop controllers. μ-synthesis yields an unconventional control design. Notice that neither the VCM nor the PZT actuator controllers contain a notch filter at the butterfly mode frequency near 6 kHz. As it turns out, the μ-synthesis controllers utilize the dynamic coupling effects between the VCM and the PZT actuator. As shown in the Bode plots of the open-loop systems in Fig. 3.28, the VCM and the PZT actuator open-loop transfer functions have almost the same magnitude, but about 180° phase difference near the butterfly mode frequency. It utilizes destructive motion of the two actuators to cancel the resonance mode in the overall open-loop system. It is a robust design, since the two actuators are exciting the same resonance mode, and they can still cancel each other even if the resonance frequency changes.

The crossover frequency, gain margin and phase margin of the overall nominal open-loop system are 1950 Hz, 8.6 dB, 37.1° respectively. Fig. 3.29 shows the Nyquist plot of the open-loop system. The Nyquist curve is located in the safe region of the diagram.

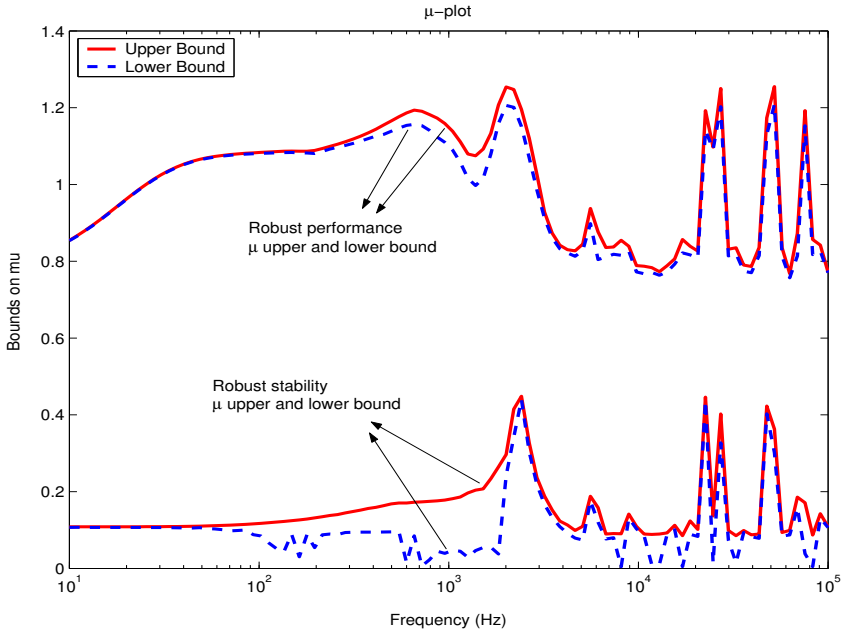

Figure 3.25: Robust stability and robust performance μ-plot.

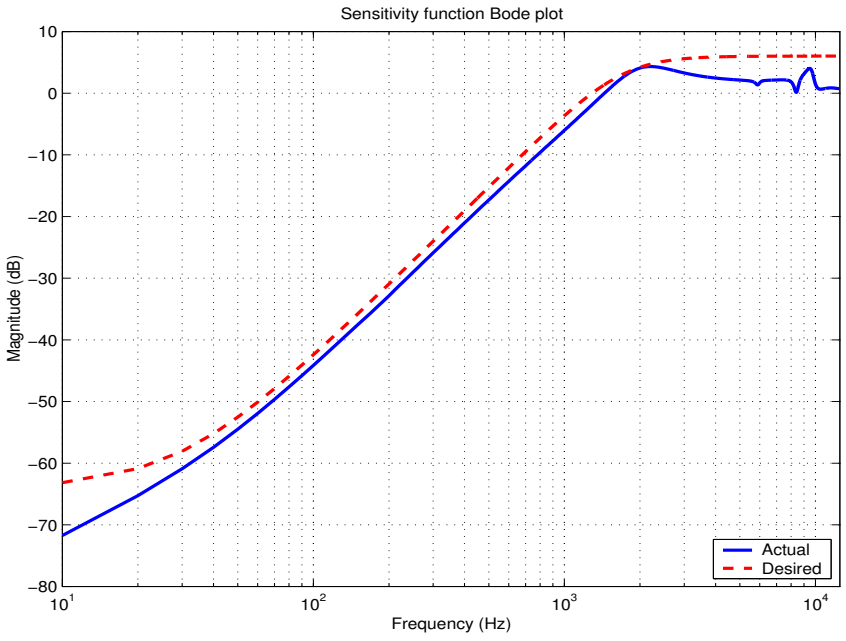

Figure 3.26: Bode plot of the closed-loop sensitivity function.

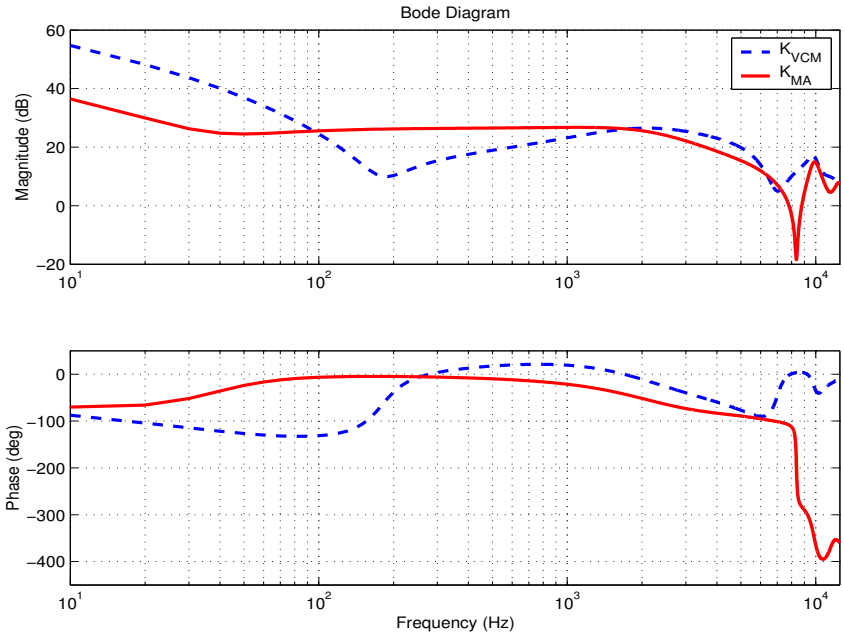

Figure 3.27: Bode plots of VCM loop and microactuator loop controllers.

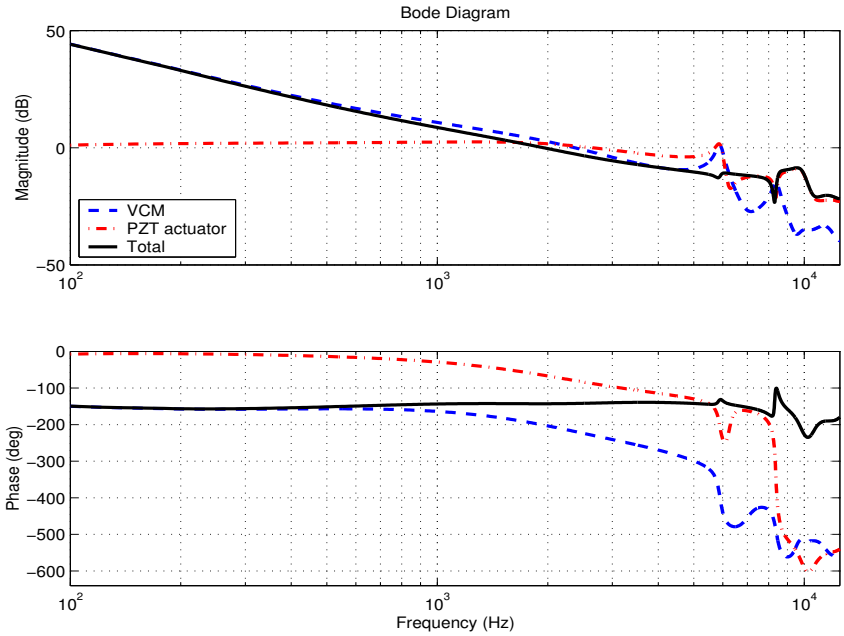

Figure 3.28: Bode plots of the VCM , PZT actuator, and overall open-loop transfer functions.

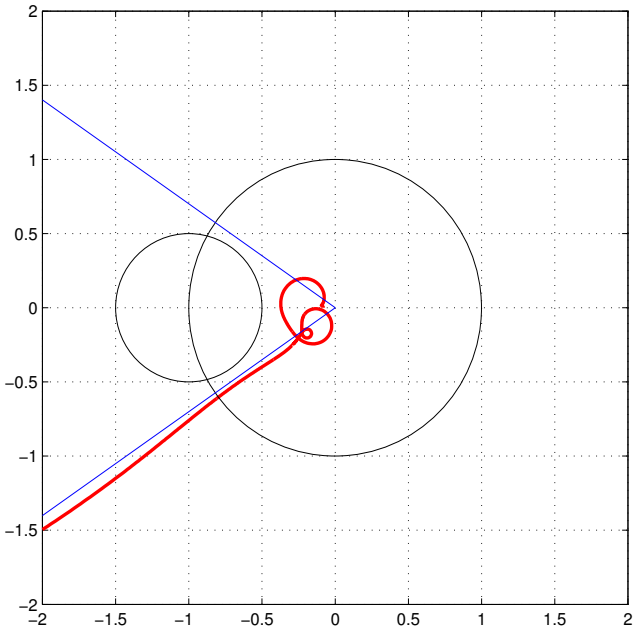

Figure 3.29: Nyquist diagram of the open-loop system.

3.3.5 Experimental Results and Comparison with the Decoupled Design

Experimental Results

Fig. 3.30 shows the sensitivity functions Bode plots. The solid and dotted lines are the experimental and the simulation data of μ-synthesis design, respectively. Table 3.4 summarizes the simulation and experimental results:

Table 3.4: Sensitivity function data of μ-synthesis design

	Unity-gain Freq. (Hz)	Maximum Peaking (dB)	Peaking Freq. (Hz)
Design Spec.	$\geq$ 1200	$\leq$ 6 dB	-
Simulation	1450	4.1	-
Experiment	1416	6.9	2260

For comparison purpose, the experimental data of the decoupled design is shown as the dashed line in the plot. As shown in the plot, the μ-synthesis design has better error

rejection in the mid-frequency range of 400-1500 Hz. However, it has less attenuation in the low frequency range below 100 Hz than the decoupled design.

Fig. 3.31 shows the FFT of measured head off-track motion when control is applied. The solid line is the result using the μ-synthesis controller, while the dotted line is the result using the decoupled controller designed in section 3.2. The FFT results agree with the sensitivity function result shown in Fig. 3.30. As shown in the plot, the μ synthesis controller has larger attenuation of error in the mid-frequency range of about 500-1000 Hz, but less attenuation of error in the low frequency range. The overall head off-track motion using μ-synthesis controller is 6.7 nm in the 1-σ value, which is slightly larger than that when using the decoupled controller. Fig. 3.17 shows the PES and the control signals of the VCM and the PZT actuator.

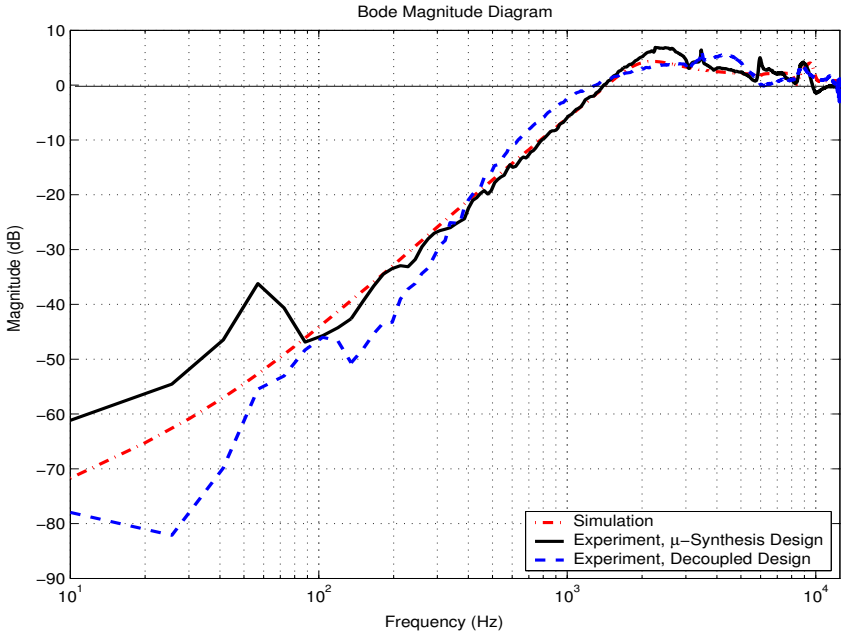

Figure 3.30: Measured sensitivity function Bode plot of the closed-loop system.

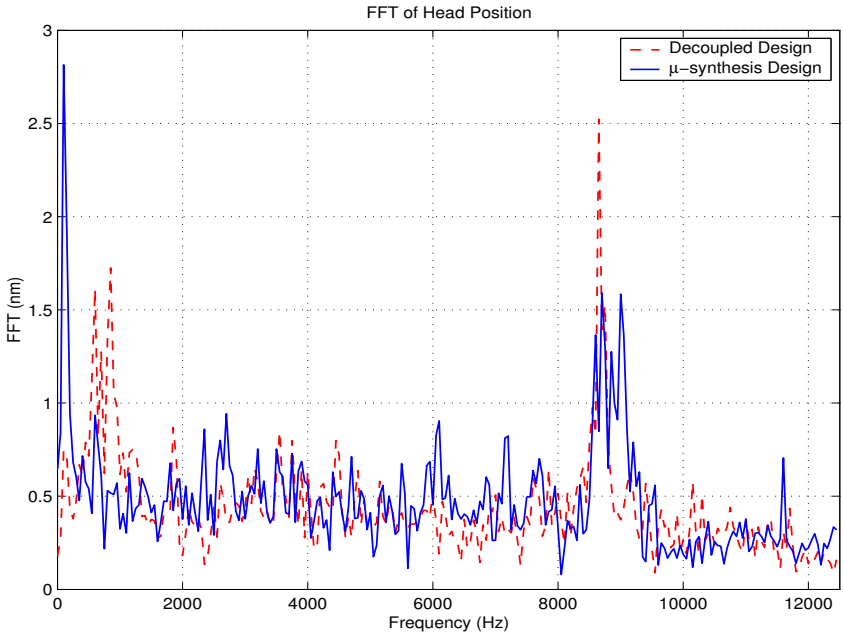

Figure 3.31: FFT of the head off-track motion when control is applied.

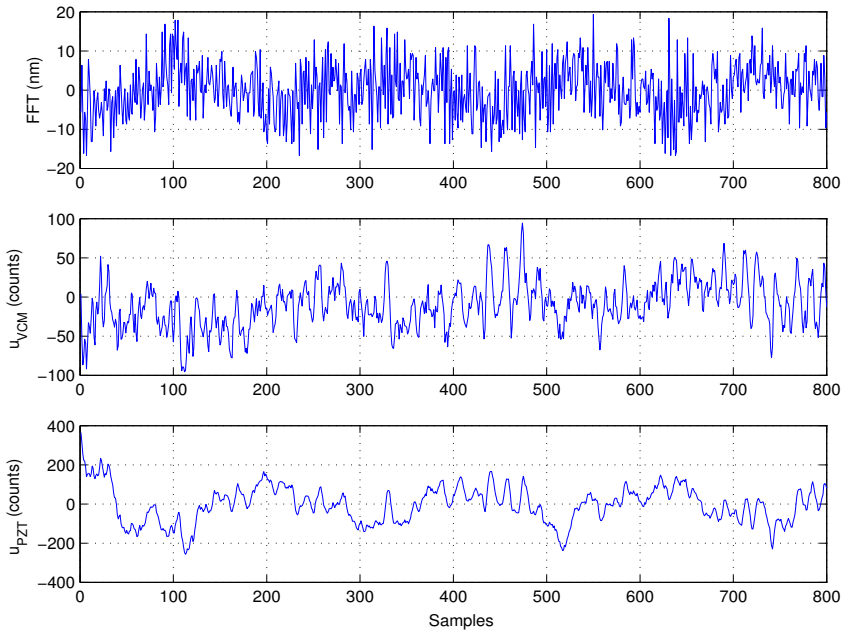

Figure 3.32: Time traces of the head position and control actions of the VCM and the PZT actuator.

Robustness Analysis of the Decoupled Design

We have mentioned in section 3.2 that there is concern about the robustness of the decoupled master-slave design for two reasons. First, the position of the PZT actuator is estimated using its DC gain and the high frequency dynamics of the PZT actuator are neglected. Second, the actual DC gain of the PZT actuator can be different from the model. The robustness of the decoupled design can be analyzed using μ. The one-input two-output controller K used in the μ-analysis in Fig. 3.22 of the decoupled design is

$$K = \begin{bmatrix} K_{VCM}\left(1 + K_{MA} g_{PZT}\right) \\ \\ K_{MA} \end{bmatrix} \tag{3.48}$$

Fig. 3.33 shows the μ bounds for robust stability and robust performance tests of the uncertainty closed-loop system with the decoupled controller. The robust stability and robust performance peak μ values are, $\beta_{RS} = 0.81$ and $\beta_{RP} = 6.27$, respectively. Thus, the decoupled design can maintain the stability of the control system for the prescribed uncertainties. However, the stability margin is much smaller than that of the μ-synthesis design. The performance of the decoupled design could have a large degradation for the perturbed system.

Comparisons of the Decoupled and the μ-Synthesis Designs

Table 3.5 compares the design and experimental testing results of the decoupled and the μ-synthesis designs. The bandwidths of the two controllers are very close. Notice that even though the decoupled design has a larger phase margin than the μ-synthesis design for the nominal system, its robustness is actually worse in terms of μ for the perturbed system. The nominal PES performance of the μ-synthesis design is slightly worse than

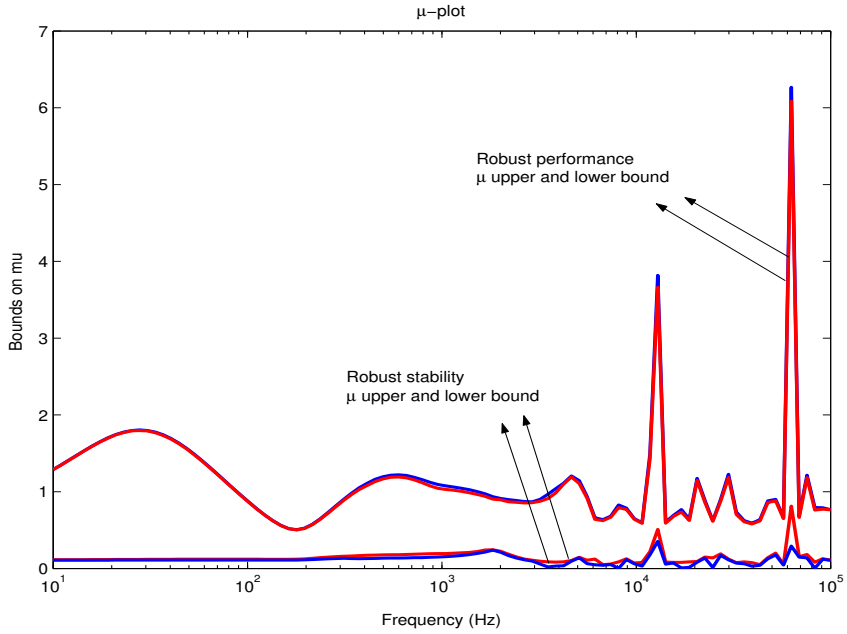

Figure 3.33: Robust stability and robust performance μ-plot of the decoupled design.

that of the decoupled design. Both the VCM and the PZT actuator controllers of the μ-synthesis design are 10th order, while those of the decoupled design are 6th and 5th orders respectively. Implementation of the μ-synthesis controller requires almost twice the computation as the controller designed using the decoupled design method.

Table 3.5: Comparison of the decoupled design and the μ-synthesis design

	Decoupled Design	μ-synthesis Design
Gain margin (dB)	7.4	8.6
Phase margin (°)	50.2	37.1
Open-loop c/o freq. (Hz)	2104	1950
Sensitivity c/o freq. (Hz)	1361	1419
Sensitivity max peaking (dB)	6.3	6.9
Robust stability μ	0.81	0.45
Robust performance μ	6.27	1.26
Closed-loop head motion (nm)	6.1	6.7
Controller order	K_{VCM}: 6th, K_{PZT}: 5th	Both 10th

Chapter 4

Active Damping of the PZT-Actuated Suspension Dual-Stage Servo System

High bandwidth dual-stage servo systems can achieve larger attenuation of low-frequency runout and disturbances. Airflow excited vibrations of high-frequency structural resonance modes become one of the major limiting factors for achieving higher track densities of dual-stage servo systems in HDDs. This chapter presents feedback damping control of the PZT-actuated suspension dual-stage system. The proposed control scheme utilizes one PZT element on the PZT-actuated suspension as a vibration sensor and the other PZT element as an actuator to damp the resonance modes of the PZT-actuated suspension dual-stage actuator. Vibration damping controller design and experimental results are presented.

4.1 Active Vibration Compensation using Dual-Stage Multi-Sensing Servo Systems

Vibration Compensation using Instrumented Suspension

The adoption of dual-stage servo systems will change the PES spectral distribution. Traditional large TMR contributors of low-frequency runout and disturbances can be sufficiently attenuated by the high bandwidth dual-stage servo control system. The TMR contributions due to air turbulence excited high-frequency structural vibrations, and other wide-band noises and disturbances, now become significant. The characterizations of airflow induced structural vibrations have been reported in [62] [30] [16], etc. It is found that the magnitude of the flow induced vibration is proportional to the square of the flow speed [62], and the airflow affects head off-track motion mainly by exciting the actuator structural resonance modes [30] [16].

In current disk drive designs, airflow excited vibrations are mitigated by using shorter and stiffer suspensions and putting air blocker in the upward-flow direction. As the track density and spindle rotation speed increase, active compensation of airflow excited vibrations may be necessary.

The compensation of these high-frequency vibrations requires a very high bandwidth and sampling frequency. However, the sampling frequency of the PES is limited by the number of servo sectors allocated to store position information on a data track. Multi-sensing servo systems using auxiliary vibration sensors can be used to compensate airflow excited vibrations. In an instrumented suspension multi-sensing servo system, strain

sensors are attached or fabricated on the surface of the suspension to detect its vibration. The location and orientation of the sensors will be optimized to give the biggest correlation between the strain sensor output and head off-track motion of the slider due to suspension vibration. A method to search the optimal sensor location and orientation on the load beam using finite element analysis has been proposed in [26].

Different control schemes for suspension vibration compensation are needed depending on the type and configuration of dual-stage actuators. The PZT actuators on the PZT-actuated suspensions are located behind the suspension and can excite the suspension dynamics. In this case, feedback active damping control can be applied. The MEMS microactuator of an actuated-slider dual-stage servo system has little effect on the suspension dynamics. In this case, feedforward control can be used to cancel the TMR induced by the suspension vibration. Fig. 4.1 illustrates these two control schemes. In this chapter, feedback damping control of the PZT-actuated suspension dual-stage system is discussed.

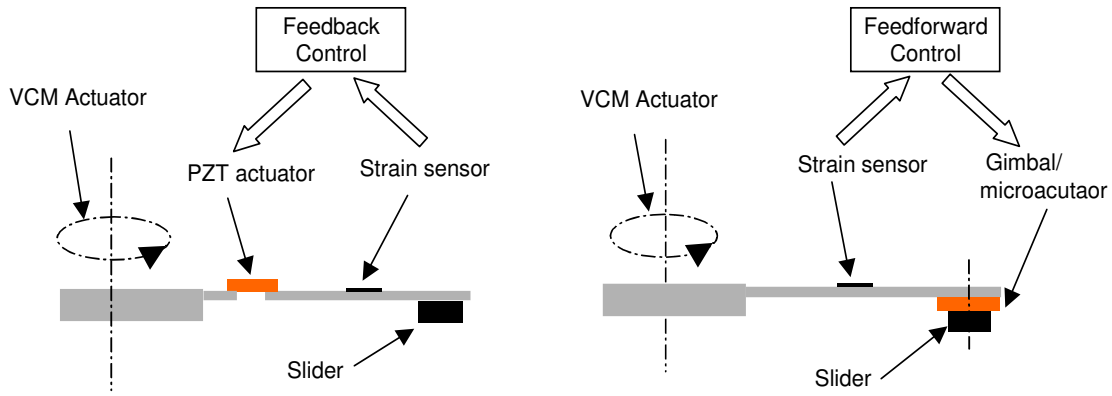

Figure 4.1: A schematic diagram of vibration compensation using dual-stage actuators.

4.1.1 Windage Vibration Sensing using the PZT Sensor

As presented in Chapter 2, the PZT elements on the PZT-actuated suspension can also be used as vibration sensors. Fig. 4.2 shows the power spectral densities (PSD) of the head off-track motion (upper half) and the PZT sensor output (lower half) when the spindle is rotating in a 7200-RPM disk drive, whose model is presented in Chapter 2.

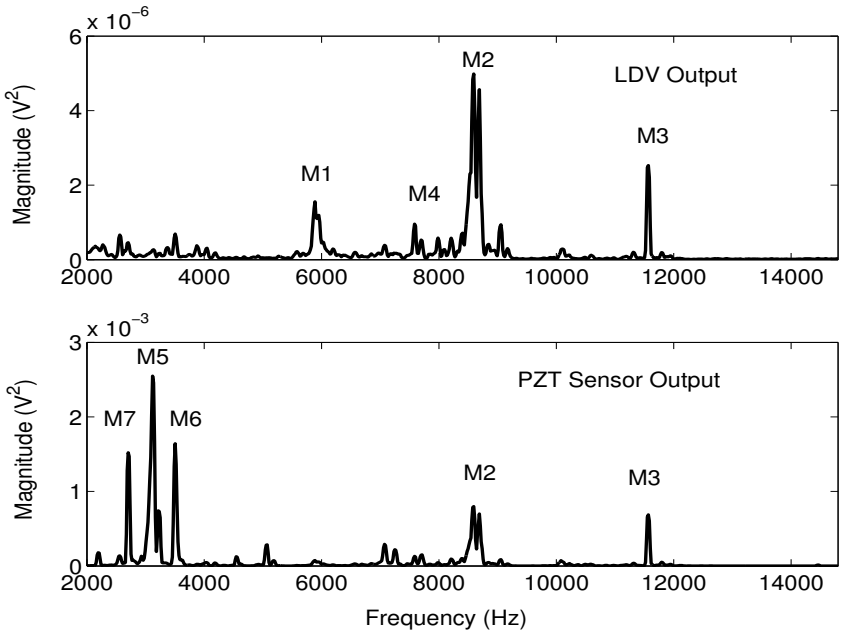

Figure 4.2: PSDs of the head off-track motion and the PZT sensor output due to airflow excited vibrations.

As shown in the figure, the major off-track modes excited by air turbulence generated by disk rotation include the butterfly mode (M1), and the suspension sway mode (M2), the suspension 1st and 2nd torsion mode (M4 and M3). The PZT sensor is able to sense the vibrations of modes M2 and M3 when they are excited by airflow disturbances, but not M1 and M4. Modes M5, M6, and M7 have a large contribution to the PZT sensor output, yet they have little contribution to the head off-track motion. These modes are

probably related to the bending modes of the suspension in the out-of-the-plane direction. The PZT sensor output can be used to implement vibration damping control of the PZT actuated suspension dual-stage system.

4.2 Controller Design

4.2.1 State Space Model Realization

The two-input two-output control system can be represented using a state space model based on the transfer functions in Eq. (2.24) and the extracted modal parameters. The rigid body mode is not observable from the PZT sensor output, and hence not included in the state space model for vibration damping control design. A state space realization including the three vibration modes M1, M2, and M3 is:

$$\begin{aligned} \dot{\mathbf{x}} &= \mathbf{A}\mathbf{x} + \mathbf{B}\mathbf{u}\,, \\ \mathbf{y} &= \mathbf{C}\mathbf{x} + \mathbf{D}\mathbf{u}\,, \end{aligned} \tag{4.1}$$

where $\mathbf{x} = [x_1\, x_2\, x_3\, x_4\, x_5\, x_6]^T$, $\mathbf{u} = [u_1\, u_2]^T$, $\mathbf{y} = [y_1\, y_2]^T$. As defined in Chapter 2, u_1 and u_2 represent the inputs to the VCM and the PZT actuator, respectively. y_1 and y_2 represent the head displacement output (excluding the rigid body mode) and the PZT sensor output, respectively. The decoupled state matrices can be written as

$$\mathbf{A} = \begin{bmatrix} A_1 & 0_{2\times2} & 0_{2\times2} \\ 0_{2\times2} & A_2 & 0_{2\times2} \\ 0_{2\times2} & 0_{2\times2} & A_3 \end{bmatrix}, \qquad \mathbf{B} = \begin{bmatrix} B_1 \\ B_2 \\ B_3 \end{bmatrix},$$

$$\mathbf{C} = \begin{bmatrix} c_{11} & 0 & c_{12} & 0 & c_{13} & 0 \\ c_{21} & 0 & c_{22} & 0 & c_{23} & 0 \end{bmatrix}, \quad \mathbf{D} = \begin{bmatrix} 0_{1\times2} \\ D_2 \end{bmatrix}, \tag{4.2}$$

where each sub-matrix is expressed as

$$A_n = \begin{bmatrix} 0 & 1 \\ a_{n1} & a_{n2} \end{bmatrix}, \quad B_n = \begin{bmatrix} 0 & 0 \\ b_{n1} & b_{n2} \end{bmatrix}, \tag{4.3}$$

$$n = 1, 2, 3.$$

where

$$a_{n1} = -\omega_n^2, \quad a_{n2} = -2\zeta_n\omega_n\,, \tag{4.4}$$

and by normalizing the PZT sensor output equation with $c_{2n} = 1, n = 1, 2, 3$, we have

$$b_{n1} = K_n^{21}, \quad b_{n2} = K_n^{22}\,,$$

$$c_{1n} = K_n^{11}/K_n^{21} = K_n^{12}/K_n^{22}\,. \tag{4.5}$$

4.2.2 Vibration Damping Control Design

Discrete-Time Vibration Damping Control Design

There are two approaches to the control design of sampled-data systems. In the continuous-time design approach, a controller is first designed in the continuous-time domain. Then the discrete-time equivalent of the controller is computed and used in simulation and testing. In the discrete-time design approach, the system model is first discretized. A discrete-time controller is then designed directly using the discretized plant model.

When the sampling frequency is high enough (10-times larger than the bandwidth of the closed-loop system) and the computational-time delay is small, the discrete-time equivalent is a very good approximation of the continuous-time system [14]. In this case,

both approaches can be used. However, the discrete-time design approach is more flexible because it allows the design of multi-rate controllers. This is particularly important for control design of disk drive systems since the sample frequency is limited. The track-following control designs presented in Chapter 3 were designed using the continuous-time design approach because of its simplicity.

For the vibration damping controller design, the effects due to the computational-time delay are significant because the bandwidth is much higher and the control algorithm is more complicated. For example, a time delay of 15 μs (actual time delay in our implementation) can result in a phase loss of 54° at 10 kHz crossover frequency. Therefore, the time delay effects must be considered in the control design process. Even though the time delay can be approximated by Pade approximation using a continuous-time model, it is much simpler and more accurate to represent the time delay using a discrete-time model since the control signal is a constant during a sample interval [4]. Thus, the discrete-time design approach will be used to design the vibration damping controller. An augmented plant model with noise modes is first discretized. A discrete-time Kalman estimator is then designed to estimate the state of the vibration modes, and the state-feedback gain matrix is designed using discrete-time linear quadratic regulator (DLQR) control to damp the resonance modes.

Augmented Plant Model for Kalman Filter Design

As shown in Fig. 4.2, modes M5, M6, and M7 have a large contribution to the PZT sensor output when excited by airflow disturbances, but have little contribution to the head off-track motion. Moreover, they are either not controllable or weakly controllable by

the control inputs. Thus, they will be modeled as sensor noise and will be accounted for in an augmented plant model described by

$$\begin{aligned}
\begin{bmatrix} \dot{\mathbf{x}} \\ \dot{\mathbf{x}_\mathbf{w}} \end{bmatrix} &= \begin{bmatrix} \mathbf{A} & \mathbf{0} \\ \mathbf{0} & \mathbf{A_w} \end{bmatrix} \begin{bmatrix} \mathbf{x} \\ \mathbf{x_w} \end{bmatrix} + \begin{bmatrix} \mathbf{B} & \mathbf{B_w 1} \\ \mathbf{0} & \mathbf{B_w 2} \end{bmatrix} \begin{bmatrix} \mathbf{u} \\ \mathbf{w} \end{bmatrix}, \\
\begin{bmatrix} \mathbf{y_1} \\ \mathbf{y_2} \end{bmatrix} &= \begin{bmatrix} \mathbf{C_1} & \mathbf{0} \\ \mathbf{C_2} & \mathbf{C_w} \end{bmatrix} \begin{bmatrix} \mathbf{x} \\ \mathbf{x_w} \end{bmatrix} + \begin{bmatrix} \mathbf{D} & \mathbf{0} \end{bmatrix} \begin{bmatrix} \mathbf{u} \\ \mathbf{w} \end{bmatrix},
\end{aligned} \tag{4.6}$$

where $\mathbf{x} \in \mathbb{R}^6$ represents the state of the three vibration modes to be controlled (M1, M2, M3); $\mathbf{A}$, $\mathbf{B}$, $\mathbf{C_1}$, and $\mathbf{C_2}$ are given by Eqs. (4.1)-(4.5); $\mathbf{x_w} \in \mathbb{R}^6$ represents the state variables of the three noise modes (M5, M6, M7); $\mathbf{w} \in \mathbb{R}^6$ is a fictitious white disturbance vector used to characterize the excitation to each vibration mode by airflow disturbances; $\mathbf{A_w}$ is estimated from the measured PSD in Fig. 4.2; $\mathbf{B_w}$ and $\mathbf{C_w}$ are normalized.

The discrete-time model of P in Eq. (4.6), with computational-time delay t_d, can be written as follows [4]

$$\begin{aligned}
\begin{bmatrix} \mathbf{x}(k+1) \\ \mathbf{x_w}(k+1) \\ \mathbf{u}(k) \end{bmatrix} &= \begin{bmatrix} \mathbf{\Phi} & 0 & \mathbf{\Gamma_1} \\ 0 & \mathbf{\Phi_w} & 0 \\ 0 & 0 & 0 \end{bmatrix} \begin{bmatrix} \mathbf{x}(k) \\ \mathbf{x_w}(k) \\ \mathbf{u}(k-1) \end{bmatrix} + \\
&\quad + \begin{bmatrix} \mathbf{\Gamma_2} \\ 0 \\ I \end{bmatrix} \mathbf{u}(k) + \begin{bmatrix} \mathbf{\Gamma_w} \end{bmatrix} \mathbf{w}(k), \quad \cdot \\
\begin{bmatrix} \mathbf{y_1}(k) \\ \mathbf{y_2}(k) \end{bmatrix} &= \begin{bmatrix} \mathbf{C} & \mathbf{C_w} & \mathbf{D} \end{bmatrix} \begin{bmatrix} \mathbf{x}(k) \\ \mathbf{x_w}(k) \\ \mathbf{u}(k-1) \end{bmatrix}
\end{aligned} \tag{4.7}$$

Assuming the computational time delay t_d is smaller than the sampling time T_s, we have

$$\Phi = e^{AT_s}\,, \tag{4.8}$$

$$\Phi_w = e^{A_w T_s}\,, \tag{4.9}$$

$$\Gamma_1 = \int_0^{t_d} e^{A\tau} B d\tau\,, \tag{4.10}$$

$$\Gamma_2 = \int_{t_d}^{T_s} e^{A\tau} B d\tau\,, \tag{4.11}$$

$$\Gamma_w = \int_0^{T_s} e^{A_w\tau} B_w d\tau\,. \tag{4.12}$$

Kalman filter and DLQR design

A discrete-time Kalman filter with prediction and correction steps was designed based on the augmented discrete-time plant model defined in Eq. (4.7), to estimate the state of the vibration modes. The two design parameters of the Kalman filter are the covariance matrix $\mathbf{W}$ of the disturbance vector $\mathbf{w}$ and the noise variance V_2 of the PZT sensor output y_2. The disturbance covariance matrix $\mathbf{W}$ can be estimated from the PSD of the PZT sensor output (see Fig. 4.2), since the disturbance input matrix $\mathbf{B_w}$ and the output matrix $\mathbf{C_w}$ are normalized. The measurement noise variance V_2 can be tuned as a design parameter to set the bandwidth of the observer.

The design of the feedback gain matrix was based on the discretization with computational delay t_d of the control plant model defined in Eq. (4.1). The feedback damping controller gain $\mathbf{K}$ was generated by a DLQR which minimizes

$$\sum_k \{y_1^2(k) + \mathbf{u}^T(k)\mathbf{R}\mathbf{u}(k)\}\,, \tag{4.13}$$

where y_1 is the head displacement output. The design parameter in the DLQR design is the control action weight matrix $\mathbf{R}$, which can be tuned to obtain desired system responses.

Simulation results

As briefly described in the previous section, the choice of the process noise weights was based on the PSD of the open-loop PZT sensor output. The remaining parameters, the measurement noise variance V_2 and the control action weight matrix $\mathbf{R}$, can be set/tuned to obtain a desired damped system. A Simulink model was used to tune these parameters, which also allowed us to test the effects of the computational delay and the noise induced by the single-precision floating point arithmetic on the damping controller. Figs. 4.3 and 4.4 show the simulation results of the damped transfer functions from the VCM and PZT actuator to the head displacement, respectively.

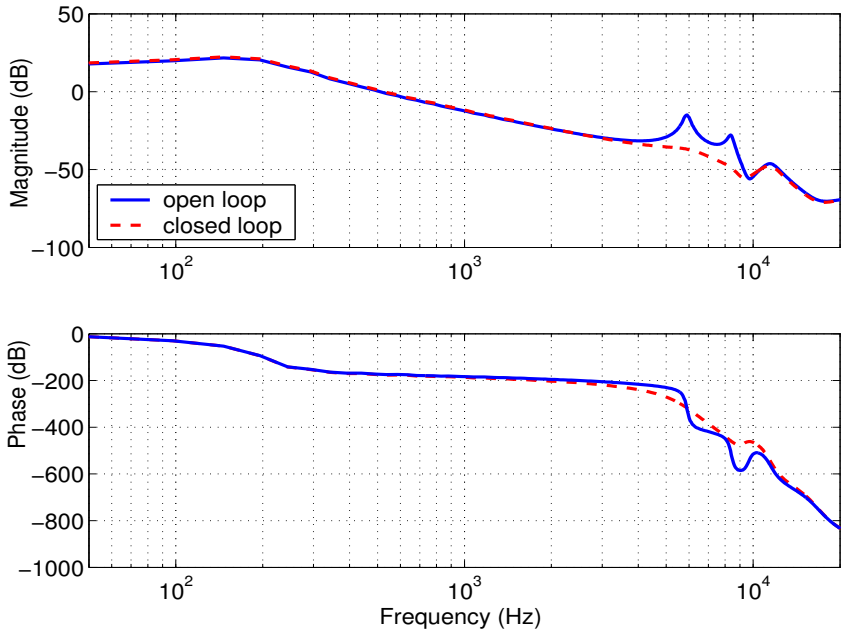

Figure 4.3: Simulated frequency response from the VCM to the head displacement.

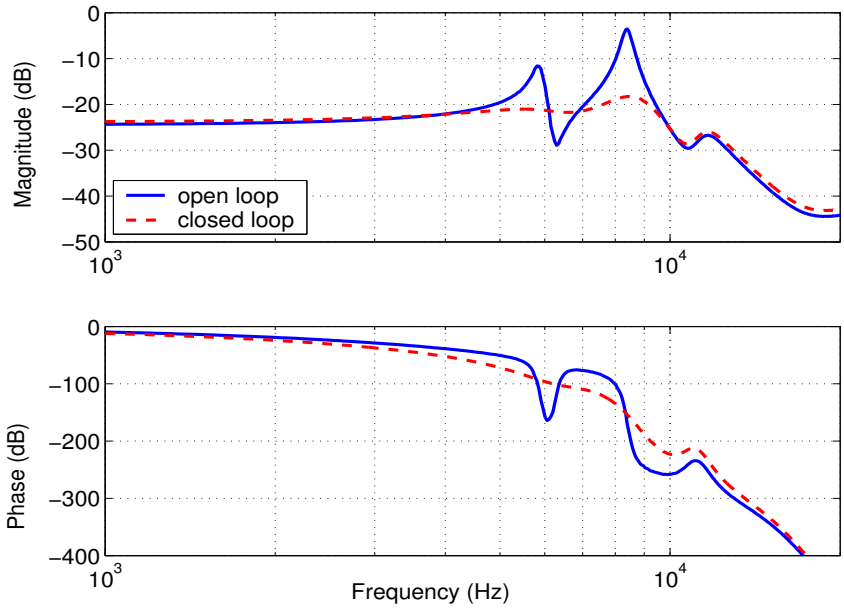

Figure 4.4: Simulated frequency response from the PZT actuator to the head displacement.

4.2.3 Track-Following Control with Active Damping

The proposed overall control structure, which includes a vibration damping control loop and a track-following control loop, is based on the block diagram shown in Fig. 4.5. The damping controller is implemented using the PZT sensor output y_2, so that its sampling frequency will not be limited by that of the PES. The sampling frequency used for the damping controller is 50 kHz, while that for the track-following controller is 25 kHz. The inner-loop vibration damping controller is designed first. Then, the outer-loop track-following controller is designed based on the damped actuator model. A decoupled control design similar to the one presented in section 3.2 is used. The gain crossover frequency, gain margin and phase margin of the open-loop transfer function of the control system are 2425 Hz, 3.4 dB and 37^o, respectively.

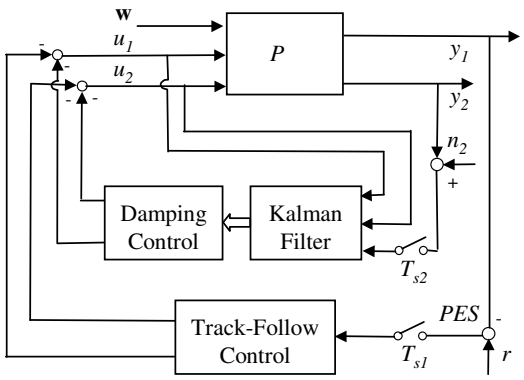

Figure 4.5: Overall control structure of track-following control with active damping.

4.3 Experimental Results

First, the inner-loop damping controller was tested. Figs. 4.6 and 4.7 compare the frequency responses of the damped system to those of the open-loop system, from the VCM and PZT actuator to the head displacement, respectively. Both the butterfly mode and the suspension sway mode are attenuated by damping control. Fig. 4.8 shows the PSD of the head lateral motion measured by the LDV and the HP digital analyzer when damping control is and is not applied. As shown in the figure, the air turbulence excited high-frequency structural vibrations are attenuated by damping control. The RMS value of the PSD from 2 kHz to 14 kHz is reduced by 35% when damping control is applied.

Second, the outer-loop track-following controller with the inner-loop damping control was tested. Fig. 4.9 shows the FFT of the head-off track motion with track-following control. The solid line is the result with combined track-following and vibration damping control. The dashed line is the result of traditional decoupled design presented in Chapter 3, which does not have a damping control loop. With damping control, the high-frequency

vibrations can be greatly attenuated. The track-following controller with damping control also has a larger disturbance attenuation in the low-frequency range because of the increased bandwidth. The standard deviation of the position error of the damping control design is 4.8 nm, while that of the traditional notch filter design is 6.1 nm.

The use of one PZT element as a vibration sensor provides a simple and effective solution to active vibration control of the PZT-actuated suspension dual-stage servo system. However, there are also some limitations to this scheme since the PZT element was not originally designed to be a sensor. It cannot sense some off-track modes, while it picks up some non-off-track modes. This makes the vibration controller complicated. The damping controller design can be simplified if an optimally designed vibration sensor is available.

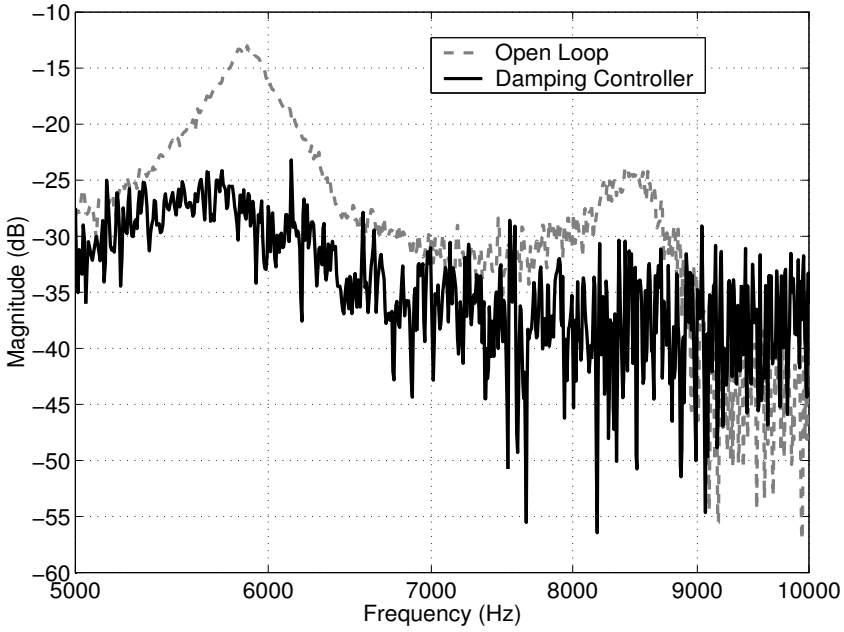

Figure 4.6: Measured frequency response from the VCM to the head displacement.

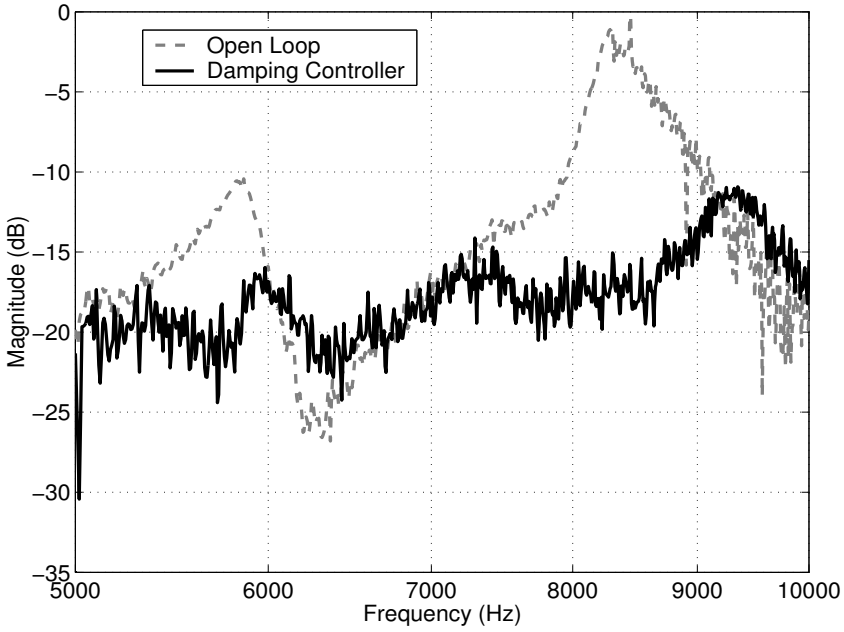

Figure 4.7: Measured frequency response from the PZT actuator to the head displacement.

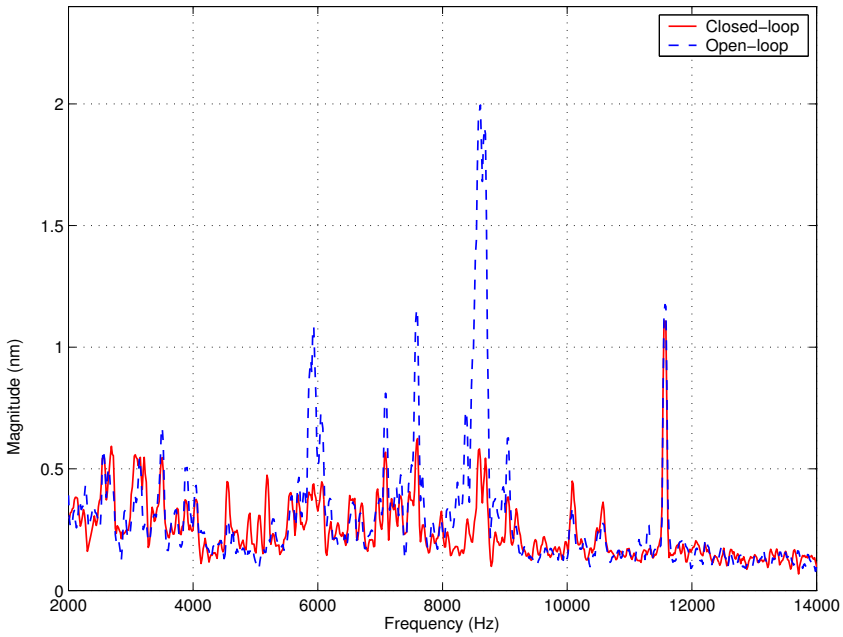

Figure 4.8: Measured PSD of head off-track motion with damping control.

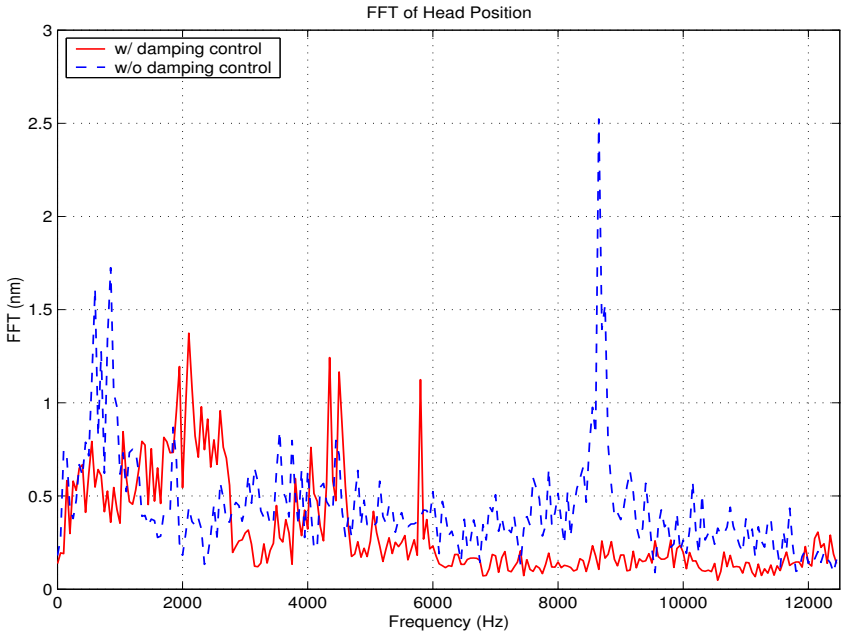

Figure 4.9: FFT of the head off-track motion with both damping and track-following control.

Chapter 5

Adaptive Control of the MEMS Microactuator Dual-Stage Servo System

MEMS microactuator dual-stage systems using the actuated-slider approach can achieve higher bandwidth than PZT-actuated suspension dual-stage systems. However, the resonance frequency of the lightly damped resonance mode of the MEMS microactuator can have large variations due to fabrication processes. Adaptive control can be used to enhance the stability and performance robustness of MEMS microactuator dual-stage servo systems. In this chapter, a self-tuning control scheme to compensate for the variations in the MEMS microactuator's resonance mode is presented. Active vibration compensation using adaptive feedforward control of the MEMS microactuator is proposed.

5.1 MEMS Microactuator Dual-Stage Actuator Model

5.1.1 Electrostatic MEMS Microactuators

MEMS electrostatic microactuators usually consist of a fixed stator element and a moving shuttle supported by a flexure. The moving shuttle can be actuated by electrostatic force generated by applying a voltage difference between the shuttle and stator [21]. There are two categories of electrostatic microactuators depending on the moving direction of the shuttle relative to the stator: comb-drive and parallel-plate, as illustrated in Fig. 5.1.

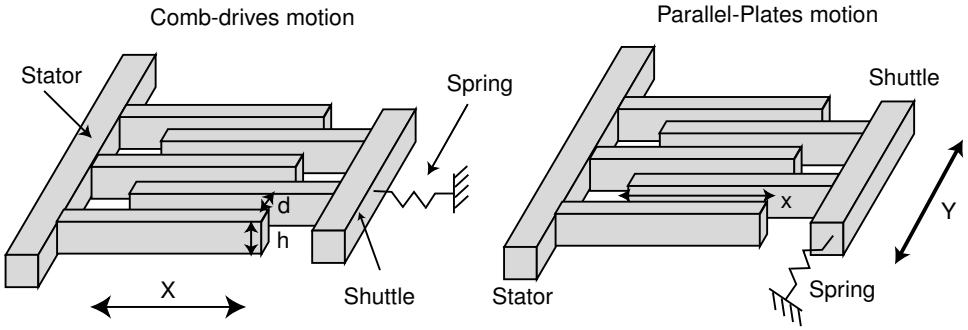

Figure 5.1: Electrostatic microactuators: comb-drive vs. parallel-plate

The electrostatic forces of comb-drive and parallel-plate actuators are

$$F_{comb} = \frac{\epsilon h}{2d} V^2 , \tag{5.1}$$

$$F_{parallel} = \frac{\epsilon x h}{2d^2} V^2 , \tag{5.2}$$

respectively, where ϵ is the permittivity of air, x is the overlap between two adjacent plates, h is the plate thickness and d is the gap between two parallel plates. As indicated in these equations, the electrostatic force of comb-drive actuators is independent of the displacement of the moving shuttle, while the electrostatic force of parallel-plate actuators is a nonlinear

function of its shuttle motion ($\propto 1/d^2$). Control of comb-drive actuators is much easier since they are linear systems. On the other hand, parallel-plate actuators can generate a larger force than the comb-drive actuator.

Electrostatic microactuators can also be categorized as rotational and translational microactuators. When using a translational microactuator in a dual-stage servo system in hard disk drives, there exists a large force coupling between the VCM and the microactuator. The acceleration of the VCM translates to an inertial force acting on the microactuator. This coupling force can be quite large during seek operations since the acceleration of the VCM can be as large as hundreds of G. The coupling force to a rotational microactuator from the VCM is much smaller.

Capacitive position sensing can be used to measure the relative position between the moving shuttle and the fixed stator in electrostatic MEMS microactuators [22], [60]. Shuttle movement causes a capacitance change between the shuttle and the stator. By measuring the change in capacitance, the shuttle location relative to the stator can be determined.

In a MEMS microactuator dual-stage system, a slider is attached on top of the MEMS microactuator. It rotates the slider relative to the suspension in the lateral direction. Usually folded beams are used as a flexure to support the moving shuttle. The stiffness of the flexure must be soft in the lateral direction in order to have enough DC gain. On the other hand, since the slider flies on top of the disk on an air bearing, the microactuator must support a vertical load with minimum deflection. Thus, the microactuator's flexure must be very stiff in the vertical direction, while soft in the lateral direction. Given the

aspect ratio of the fabrication process, MEMS microactuators used in disk drive dual-stage servo systems are usually designed to have a nominal resonance frequency of 1-2 kHz to satisfy these two constraints [22], [13].

The in-plane stiffness of a beam flexure is expressed as

$$k = \frac{Yhw^3}{l^3}\,, \tag{5.3}$$

where Y is Young's modulus, h, w, l are the height, width, and length of the beam, respectively. The stiffness is a strong function of the beam's geometric parameters. Thus, variations in the flexure's width caused by lithographic misalignments and variations present in the etching processes will have a large effect on the stiffness of the flexure, (or equivalently the natural frequency of the microactuator's resonance mode). It is estimated that the resonance frequency can have as much as $\pm 15\%$ variations from the designed nominal value.

5.1.2 IBM MEMS Microactuator Model

In this dissertation, the system configuration is based on a comb-drive, rotational electrostatic MEMS microactuator developed by IBM Almaden Research Center [13]. The microactuator is fabricated using a high-aspect-ratio etching and electroplating multi-layer fabrication technology. The process includes high-aspect-ratio Transformer-Coupled Plasma (TCP) reactive-ion etching (RIE), which achieves a 20:1 height-to-width aspect ratio on 40 μm thick polymers. The etched polymers are in turn used as molds to fabricate, through a metal electroplating process, high-aspect ratio Invar (a nickel-iron-based alloy) microstructures. Fig. 1.9 shows a photograph of such a device mounted on an integrated lead

suspension.

The microactuator has a single resonance mode, whose natural frequency was designed to have a nominal value of 1.5 kHz. The microactuator does not have other appreciable structural dynamics up to 40 kHz frequency range except this single flexure resonance mode [13]. Thus, its dynamics can be described by a mass-spring-damper 2nd-order transfer function

$$G_M(s) = \frac{A_M}{s^2 + 2\zeta_{MO}\omega_{MO}\, s + {\omega_{MO}}^2}\,. \tag{5.4}$$

Table 5.1 provides values for the parameters in Eq. (5.4) and some other parameters of the IBM microactuator model.

Table 5.1: IBM's electrostatic microactuator parameters

Res. Freq. ω_{MO}	Damping Coeff. ζ_{MO}	Stroke limit	Acc. Gain A_M	Max. Voltage
1.5 kHz ($\pm$15%)	0.015	$\pm$1 μm	2 G/V	$\pm$40 V

5.1.3 Decoupled MEMS Microactuator Dual-Stage Actuator Model

Assuming the VCM as a rigid body, the equations of motion of the dual-stage system with a rotational microactuator are:

$$J_V^*\ddot{\theta}_V = \tau_V - J_M\ddot{\theta}_M\,, \tag{5.5}$$

$$J_M\ddot{\theta}_M + B_M\dot{\theta}_M + K_M\theta_M = \tau_M - J_M\ddot{\theta}_V\,, \tag{5.6}$$

where the equivalent inertia

$$J_V^* = J_V + J_M + M_M l^2\,, \tag{5.7}$$

and J_V and J_M are the moments of inertia of the VCM and the microactuator, respectively. M_M is the mass of the microactuator and slider assembly. l is the distance between the mass

center of the microactuator and the pivot of the VCM. θ_V and θ_M are the angular positions of the VCM and the microactuator relative to the VCM, respectively. τ_V and τ_M are the torques generated by the VCM and the microactuator, respectively. K_M and B_M are the stiffness and damping coefficient of the microactuator, respectively. Given the fact that the inertia of the microactuator is very small compared to that of the VCM ($\frac{J_M}{J_V} = 1.1e-7$ for the model we used), the coupling term $J_M\ddot{\theta}_M$ in Eq. (5.5) can be neglected and the motion of the microactuator can be assumed to have no effect on the motion of the VCM. Eq. (5.6) can be rewritten as:

$$J_M^*\ddot{\theta}_M + B_M\dot{\theta}_M + K_M\theta_M = \tau_M^* \,, \tag{5.8}$$

where

$$J_M^* = J_M(1 - \frac{J_M}{J_V^*}) \,,\; \tau_M^* = \tau_M - \frac{J_M}{J_V^*}\tau_V \,. \tag{5.9}$$

The above equation shows that the motion of the microactuator can be decoupled from the VCM by feeding τ_V to the microactuator with a proper gain. As a consequence, for controller design purposes, the dual-stage system can be approximated by a decoupled model by adding the outputs of the VCM and the microactuator, as shown in Fig. 5.2. In Fig. 5.2, G_V and G_M represent the VCM and microactuator models, respectively. x_p and x_v denote the absolute positions of the read/write head and the tip of the suspension respectively. $RPES$ denotes the position of the microactuator relative to the suspension,

$$x_p = x_v + RPES \,. \tag{5.10}$$

The following controller designs are based on this decoupled dual-stage model. For

implementation, the actual control torque to the microactuator is given by

$$\tau_M = \tau_M^* + \frac{J_M}{J_V^*}\tau_V \,, \tag{5.11}$$

where τ_M^* and τ_V are generated from the designed controller.

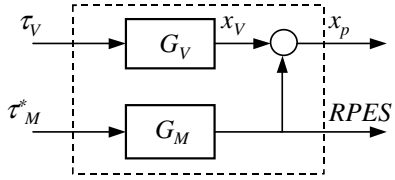

Figure 5.2: Decoupled MEMS microactuator dual-stage control plant.

5.2 Decoupled Discrete-Time Pole Placement Track-Following Controller Design

5.2.1 Decoupled Control Design Structure

A block diagram for MIMO decoupling control design is shown in Fig. 5.3.

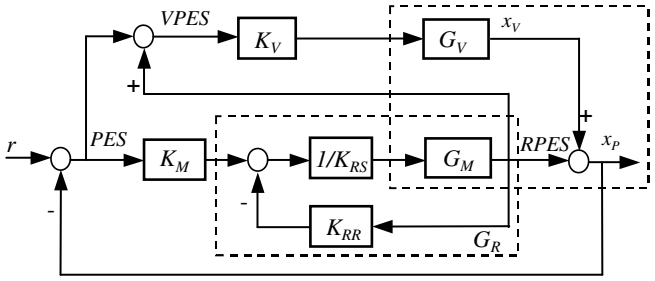

Figure 5.3: Decoupled dual-stage control design block diagram.

The part enclosed in the dashed box on the upper-right corner of Fig. 5.3 is the open-loop system depicted in Fig. 5.2. In Fig. 5.3, r represents the runout, PES is the

position error signal of the head relative to the data track center (i.e., $PES = r - x_P$), and $RPES$ is the position error signal of the head relative to the tip of the suspension (i.e., $RPES = x_P - x_v$).

As shown in the block diagram, there are three compensators that need to be designed: the VCM loop compensator K_V; the microactuator PES loop compensator K_M; and the microactuator $RPES$ inner-loop compensator $K_{MM} = K_{RR}/K_{RS}$. The microactuator inner-loop compensator is used to damp the microactuator's flexure resonance mode. The damped microactuator closed-loop transfer function G_R, shown in the lower-middle dashed box, is defined by

$$G_R = \frac{G_M}{K_{RS} + G_M\, K_{RR}}\,. \tag{5.12}$$

The control structure in Fig. 5.3 uses the same sensitivity function decoupling technique described in section 3.2. Following the same derivation, the total dual-stage open-loop transfer function from r to x_P, G_T, is

$$G_T = K_V\, G_V + K_M\, G_R + K_M\, G_R\, K_V\, G_V\,. \tag{5.13}$$

The total closed-loop sensitivity function from r to PES equals the product of the VCM and microactuator loop sensitivity functions, S_V and S_M, respectively:

$$S_T = \frac{1}{1 + G_T} = S_V\, S_M\,, \tag{5.14}$$

where

$$S_V = \frac{1}{1 + K_V\, G_V} \quad , S_M = \frac{1}{1 + K_M\, G_R}\,. \tag{5.15}$$

The microactuator loop sensitivity function can be designed by a two-step pole placement design process which will be introduced in the next section.

5.2.2 Closed-Loop Sensitivity Function Design by Pole Placement

The zero-order-hold (ZOH) discrete-time transfer function of a 2nd-order system, as shown in Fig. 5.4, can be written as

$$G_o(q^{-1}) = \frac{q^{-1}\, B_o(q^{-1})}{A_o(q^{-1})}\,, \tag{5.16}$$

where q^{-1} is the one-step delay operator, $B_o(q^{-1})$ and $A_o(q^{-1})$ are the plant zero and pole polynomials, respectively.

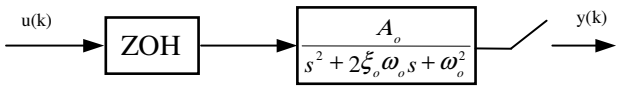

Figure 5.4: Zero-order-hold of a 2nd-order system.

The closed-loop sensitivity function of the system can be designed by pole placement, solving the following Diophantine equation [4]:

$$A_c(q^{-1}) = A_o(q^{-1})S(q^{-1}) + q^{-1}B_o(q^{-1})R(q^{-1})\,, \tag{5.17}$$

where $A_c(q^{-1})$ is the desired closed-loop characteristic polynomial. The discrete-time controller $C(q^{-1})$ is

$$C(q^{-1}) = \frac{R(q^{-1})}{S(q^{-1})}\,. \tag{5.18}$$

The closed-loop sensitivity function, G_S, is

$$G_S(q^{-1}) = \frac{1}{1 + G_o(q^{-1})C(q^{-1})} = \frac{A_o(q^{-1})\, S(q^{-1})}{A_c(q^{-1})}\,. \tag{5.19}$$

The open-loop and closed-loop pole polynomials, $A_o(q^{-1})$ and $A_c(q^{-1})$, determine the shape of the sensitivity function.

$A_c(q^{-1})$ can be chosen such that the required bandwidth and system response are satisfied. Usually it is more intuitive to describe it with its continuous-time equivalent parameters: the damping ratio, ζ, and the natural frequency, ω_n. The damping ratio is directly related to the phase margin of the open-loop transfer function. For a typical design, it can be chosen to be equal to or greater than 1, in order to ensure adequate phase margin. ω_n is related to the control bandwidth.

5.2.3 Dual-Stage Sensitivity Function Design

The three compensators in the dual-stage servo system depicted in Fig. 5.3 can be designed by a two-step design process, as illustrated in Fig. 5.5.

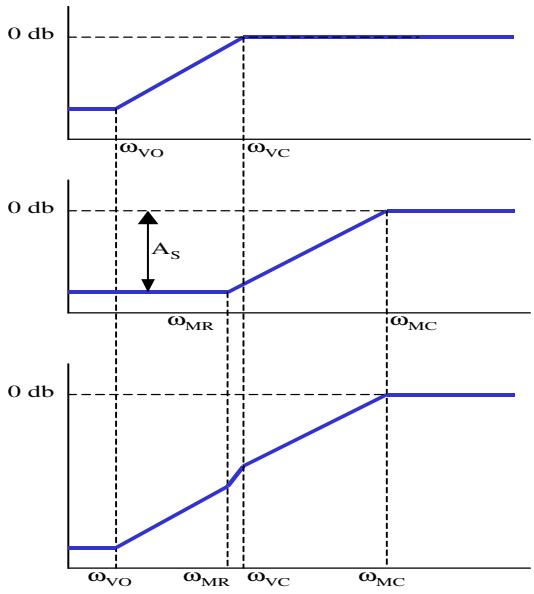

Figure 5.5: Illustration of the dual-stage sensitivity function design.

First, the VCM loop compensator, K_V, is designed to attain a desired VCM closed-loop sensitivity, S_V, as shown in the top part of Fig. 5.5. Its bandwidth, ω_{VC} in Fig. 5.5, is

generally limited by the E-block and suspension resonance modes.

The second step of the design process involves the design of the microactuator loop compensators to attain additional attenuation S_M, as shown in the middle part of Fig. 5.5. This step is itself accomplished in two steps. First, the inner $RPES$ loop compensator, K_{RR}/K_{RS}, is determined to damp the microactuator resonance mode and place the poles of G_R, or equivalently ω_{MR} in Fig. 5.5, at desired locations. The compensator can be obtained by solving a Diophantine equation by pole placement as described in the previous subsection. The poles of G_R will become the zeros of the microactuator loop sensitivity function, S_M.

Finally, the PES loop compensator, K_M, is designed to place the poles, or equivalently ω_{MC} in Fig. 5.5, of the microactuator outer-loop closed-loop sensitivity function S_M. ω_{MC} is mainly limited by the PES sampling frequency and computational time delay since the microactuator has very clean dynamics up to 40 kHz frequency [57].

The total dual-stage sensitivity function is shown in the bottom part of Fig. 5.5. For a given ω_{MC}, the additional attenuation A_S in the low-frequency region, provided by the microactuator loop, will be determined by ω_{MR}. In our proposed procedure, the initial value of ω_{MR} can be chosen to be the same as ω_{VC}. It is then adjusted so that the desired attenuation and phase margin requirements of the overall dual-stage system are satisfied. Decreasing ω_{MR} increases the low-frequency attenuation of the closed-loop sensitivity function S_T, but also reduces the phase margin of open-loop transfer function G_T.

5.2.4 Design and Simulation Results

For comparison purposes, the same VCM model and VCM loop controller design of the PZT-actuated suspension dual-stage system presented in Chapter 3 were used, and the PZT actuator loop was replaced by the MEMS microactuator loop. The sampling frequency is also the same at 25 kHz.

The natural frequency and damping ratio for the microactuator inner-loop pole placement design were chosen to be $\omega_{MR} = 200$ Hz and $\zeta_{MR} = 1$, and for the outer-loop pole placement design chosen to be $\omega_{MC} = 6000$ Hz and $\zeta_{MC} = 1$. Fig. 5.6 shows the Bode plots of the microactuator open-loop transfer function G_M, inner $RPES$ loop closed-loop transfer function G_R and outer PES closed-loop sensitivity function S_M.

Fig. 5.7 shows the Bode plots of the dual-stage closed-loop sensitivity functions. Fig. 5.8 shows the Bode plots of the dual-stage open-loop transfer functions. The solid lines in these two figures are the results of the MEMS microactuator dual-stage system, while the dashed lines are the results of the PZT-actuated suspension dual-stage system. MEMS microactuator dual-stage system can achieve a much higher bandwidth than the PZT-actuated suspension dual-stage system. Table 5.2 compares the design results of these two kinds of dual-stage servo systems. Fig. 5.9 shows the open-loop Nyquist plot of MEMS microactuator dual-stage servo system.

Table 5.2: Comparison of control design results of the PZT-actuated suspension and the MEMS microactuator dual-stage servo systems

	PZT-actuated suspension	MEMS microactuator
Open-loop gain c/o freq. (Hz)	2104	3780
Gain margin (dB)	7.4	6.4
Phase margin (°)	50.2	38.3
Sensitivity unity freq. (Hz)	1361	2480
Sensitivity max peaking (dB)	6.3	6.1

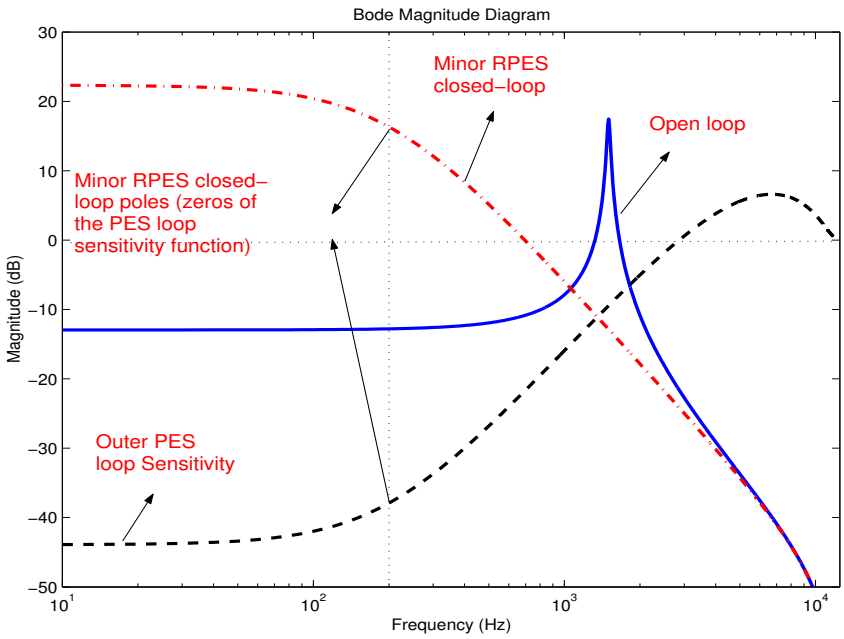

Figure 5.6: Bode plots of the MEMS microactuator open-loop and closed-loop transfer functions.

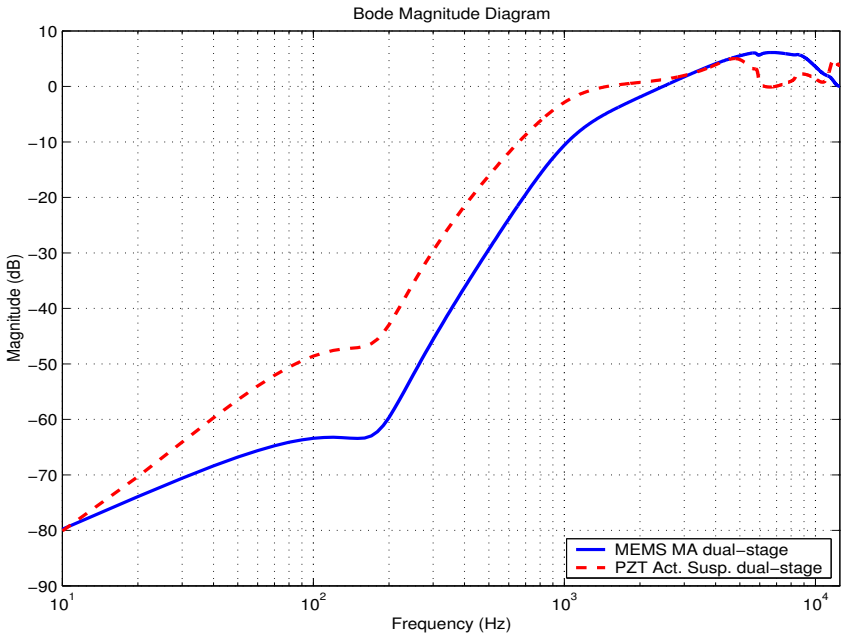

Figure 5.7: Bode plots of the dual-stage closed-loop sensitivity functions.

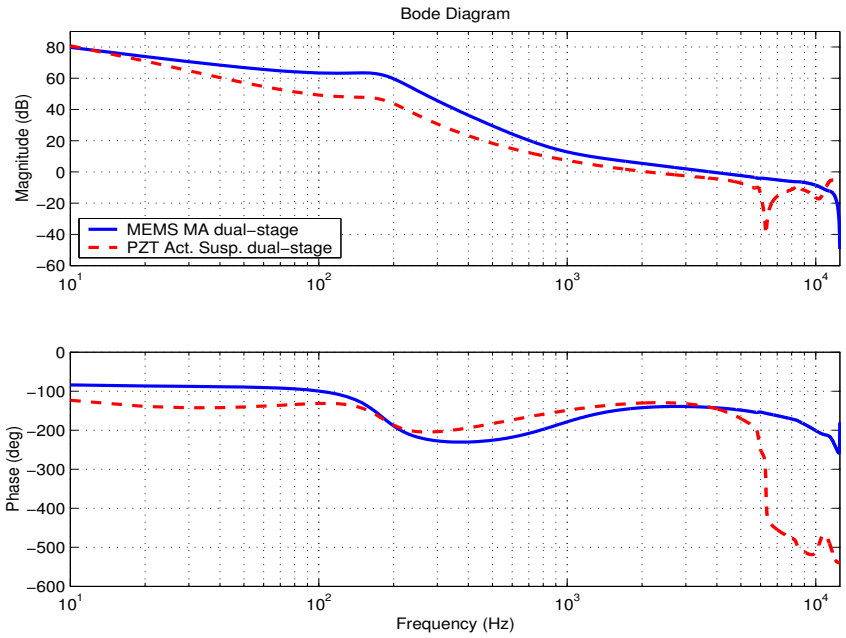

Figure 5.8: Bode plots of the dual-stage open-loop systems.

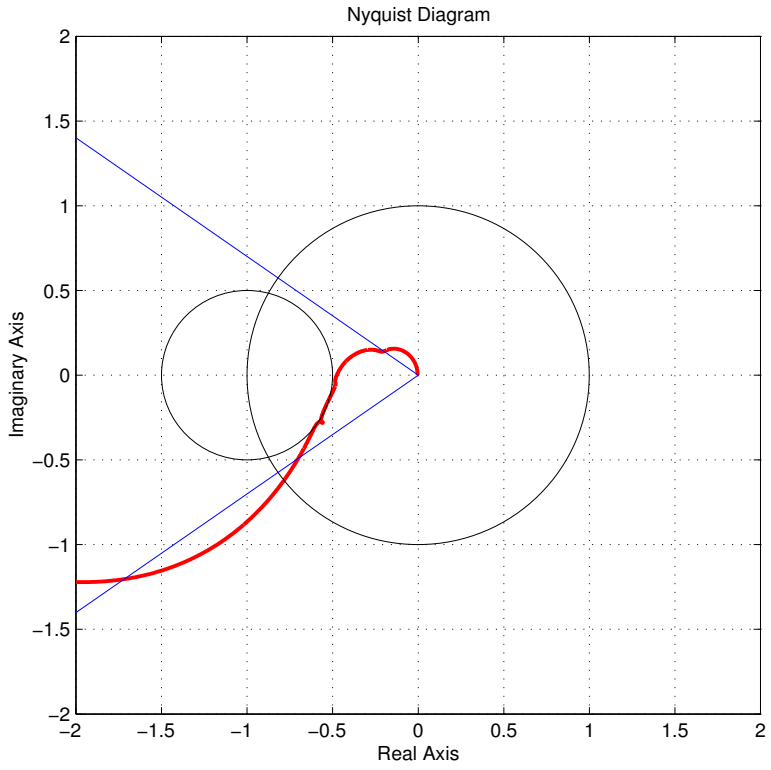

Figure 5.9: Nyquist diagram of the dual-stage open-loop system.

5.3 Self-tuning Control of the MEMS Microactuator

An adaptive control scheme can be combined with the decoupled discrete-time pole placement design methodology described above to compensate for the variations in the microactuator's resonance mode by tuning the microactuator $RPES$ inner-loop compensator.

A block diagram for the microactuator inner-loop self-tuning control is shown in Fig. 5.10. The parameter adaptation algorithm (PAA) is a direct self-tuning algorithm, based on the microactuator inner-loop pole placement design.

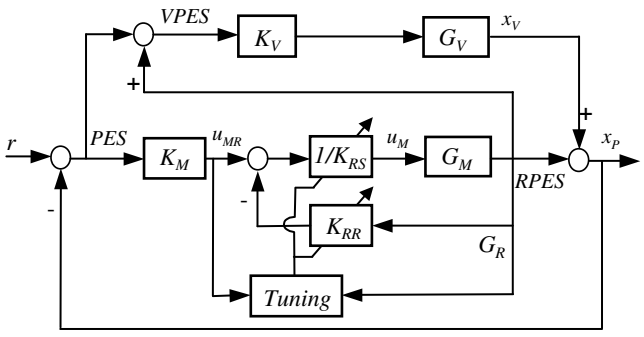

Figure 5.10: Self-tuning control of the microactuator.

Consider the microactuator open-loop transfer function in Eq. 5.16. Since the microactuator's resonance mode is lightly damped, the zero of the microactuator's discrete-time transfer function is very close to 1 ($z_o \approx 1$). Thus, it is possible to factor out the "known" term $(1 + z_o q^{-1})$ from the Diophantine equation (5.17). The resulting $RPES$ inner-loop closed-loop dynamics is given by

$$A_c(q^{-1})y(k) = q^{-1}b_0(1 + z_o q^{-1})\left[K_{RS}(q^{-1})u_M(k) + K_{RR}(q^{-1})y(k)\right] ,$$

where u_M is the control input to the microactuator. y denotes the position of the microactuator relative to the VCM, i.e., $y = RPES$.

Let

$$S(q^{-1}) = b_0 K_{RS}(q^{-1}) = s_0 + s_1 q^{-1}\,, \tag{5.20}$$

$$R(q^{-1}) = b_0 K_{RR}(q^{-1}) = r_0 + r_1 q^{-1}\,. \tag{5.21}$$

Define the control parameters vector

$$\theta = [s_0\ s_1\ r_0\ r_1]^T\,, \tag{5.22}$$

and the regressor vector, $\phi(k)$ and the filtered regressor vector, $\phi_f(k)$,

$$\phi(k) = [u_M(k)\ u_M(k-1)\ y(k)\ y(k-1)]^T\,, \tag{5.23}$$

$$A_c(q^{-1})\phi_f(k) = (1 + z_o q^{-1})\phi(k)\,. \tag{5.24}$$

The closed-loop $RPES$ dynamics can be written as

$$y(k) = \theta^T \phi_f(k-1)\,. \tag{5.25}$$

From Eq. (5.25), the controller parameter vector estimate $\hat{\theta}(k) = [\hat{s}_0(k)\ \hat{s}_1(k)\ \hat{r}_0(k)\ \hat{r}_1(k)]^T$ can be updated using a standard recursive least squares algorithm (RLS) [3]:

$$\hat{\theta}(k) = \hat{\theta}(k-1) + P(k)\phi_f(k)e^o(k)\,, \tag{5.26}$$

$$e^o(k) = y(k) - \hat{\theta}^T(k-1)\phi_f(k-1)\,, \tag{5.27}$$

$$P(k) = P(k-1) - \frac{P(k-1)\phi_f(k-1)\phi_f^T(k-1)P(k-1)}{1 + \phi_f^T(k-1)P(k-1)\phi_f(k-1)}\,. \tag{5.28}$$

The control law is

$$\hat{S}(k, q^{-1}) u_M(k) = \hat{s}_0(k) u_{MR}(k) - \hat{R}(k, q^{-1})\, y(k)\,, \tag{5.29}$$

with

$$\hat{S}(k, q^{-1}) = \hat{s}_0(k) + \hat{s}_1(k) q^{-1}\,, \tag{5.30}$$

$$\hat{R}(k, q^{-1}) = \hat{r}_0(k) + \hat{r}_1(k) q^{-1}\,, \tag{5.31}$$

and $u_{MR}(k)$ being the output of the microactuator fixed outer-loop compensator K_M, $u_M(k)$ being the control input to the microactuator.

Fig. 5.11 shows the simulation results of the control parameters estimates using the RLS algorithm. In the simulation, simulated runout, VCM and MA torque disturbances, PES and $RPES$ measurement noises were injected into the dual-stage system. A white noise with RMS value of 10 nm was used for the $RPES$ sensing signal. This noise is mainly due to thermal noise and feedthrough in the capacitive sensing electronics [60] [22]. The simulation in Fig. 5.11 is for the case when the real microactuator resonance frequency is 1.2 times its nominal value. The controller parameters converge to their desired values. Similar responses were obtained when the real resonance frequency is 0.8 times the nominal value. After the control parameters converge, the closed-loop poles of the $RPES$ inner-loop transfer function G_R converge to the desired nominal values, and nominal stability and performance can be achieved for the dual-stage control system.

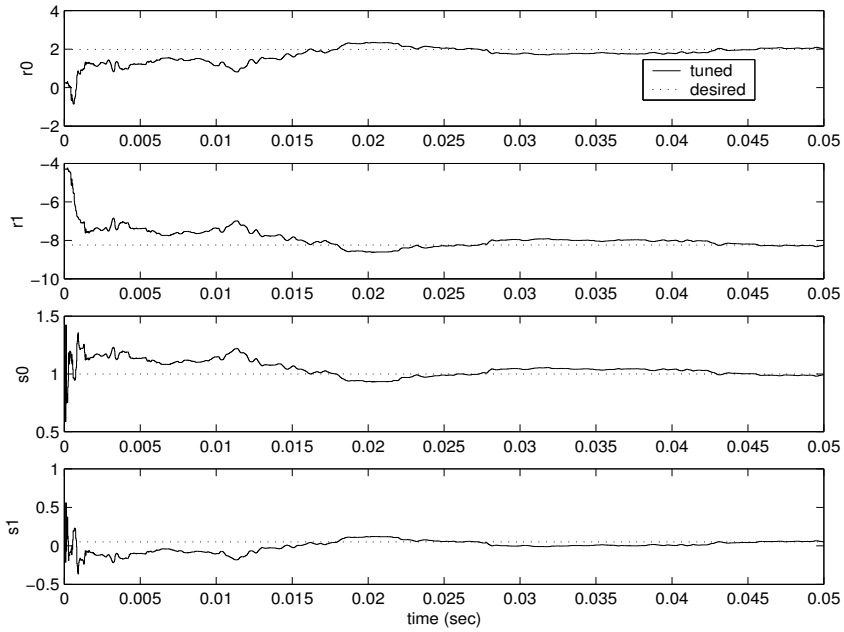

Figure 5.11: Control parameters adaptation simulation.

5.4 Adaptive Feedforward Vibration Compensation using the MEMS Microactuator Dual-Stage Servo System

In Chapter 4, vibration compensation using feedback damping control of the PZT-actuated suspension dual-stage system was discussed. In this section, vibration compensation using the MEMS microactuator dual-stage servo system is presented. In this case, the piggy-back MEMS microactuator is positioned at the end of the suspension. Assuming that the excitation to the suspension resonance modes by the reaction force of the microactuator is negligible, the vibration compensation scheme is a feedforward control scheme. The feedforward controller uses vibration sensor information and controls the microactuator to cancel head motion resulting from suspension vibrations.

5.4.1 Adaptive Feedforward Vibration Compensation

An adaptive feedforward control structure for vibration cancellation using the microactuator is shown in Fig. 5.12 (dual-stage feedback part is not shown in the figure). In the figure, w represents the airflow excitation to the suspension. d denotes the head motion due to suspension vibration, and G_{wd} is the transfer function from w to d. z denotes the strain sensor output, and G_{wz} is the transfer function from w to z. Ideally we would like z and d to have the biggest possible correlation. However, since z and d are measured at different locations on the suspension, even though G_{wz} and G_{wd} have the same poles, they usually have different zeros. Therefore, d and z will probably have a dynamic relationship. Define the transfer function from z to d to be

$$G_{zd} = \frac{G_{wd}}{G_{wz}}\,. \tag{5.32}$$

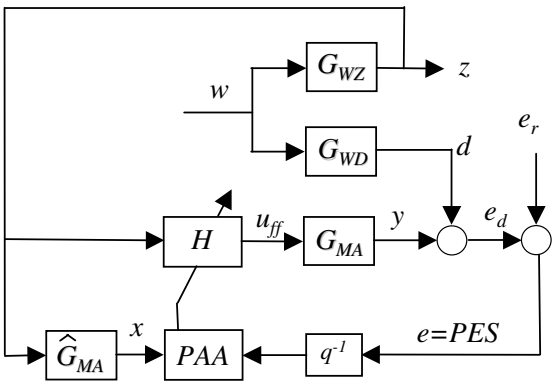

Figure 5.12: Adaptive feedforward control for vibration cancellation.

G_{MA} in Fig. 5.12 represents the model of the microactuator. H is the feedforward

filter, which needs to be designed, in order to cancel d. Intuitively, an expression for H can be

$$H = (G_{MA})^{-1} G_{zd} \,. \tag{5.33}$$

However, H as given by Eq. (5.33) may not be causal and the transfer function of G_{zd} is not precisely known. Furthermore, the strain gauge factor usually is sensitive to temperature. Thus, the optimal filter H needs to be estimated and tuned using an adaptive scheme. H can be approximated by a finite impulse response (FIR) filter

$$H(q^{-1}) = h_0 + h_1 q^{-1} + ... + h_M^{-M} \,, \tag{5.34}$$

where q^{-1} is the one-step delay operator and M is the order of the FIR filter. The output of the microactuator is

$$\begin{aligned} y(k) &= G_{MA}(q^{-1}) u_{ff} \\ &= G_{MA}(q^{-1}) H(q^{-1}) z(k) \\ &= H(q^{-1}) G_{MA}(q^{-1}) z(k) \,. \end{aligned} \tag{5.35}$$

Let

$$x(k) = G_{MA}(q^{-1}) z(k) \,, \tag{5.36}$$

and define the regressor vector,

$$\phi(k) = [x(k)\, x(k-1) \,...\, x(k-M)]^T \,, \tag{5.37}$$

and the FIR tap weight vector,

$$\theta = [h_0\, h_1 \,...\, h_M]^T \,. \tag{5.38}$$

The output equation of the microactuator can be written as

$$y(k) = \theta^T \phi(k)\,. \tag{5.39}$$

The vibration compensation error is defined by

$$e_d(k) = y(k) + d(k)\,. \tag{5.40}$$

A parameter adaptation algorithm (PAA) can be used to estimate the coefficients of $H(q^{-1})$, $\hat{\theta}$, to minimize the mean square value of e_d, $E[|e_d(k)|^2]$. However, e_d is not available, and the error signal that we have access to is the PES, which can be written as

$$e(k) = e_d(k) + e_r(k)\,, \tag{5.41}$$

where e_r represents the position error due to other sources, such as runout, after compensated for by the feedback controller. Assuming that d is uncorrelated with e_r, we have

$$E[|e(k)|^2] = E[|e_d(k)|^2] + E[|e_r(k)|^2]\,. \tag{5.42}$$

Thus, minimizing $E[|e(k)|^2]$ is equivalent to minimizing $E[|e_d(k)|^2]$. Therefore, the PES, e, can be used as a corrupted error signal for the PAA, and e_r acts as a noise to the adaptation process.

The regressor defined in Eq. (5.36) will be estimated by filtering z with the microactuator model, $\hat{G}_{MA}$,

$$\hat{x}(k) = \hat{G}_{MA}(q^{-1}) z(k)\,. \tag{5.43}$$

In next section, we will discuss how $\hat{G}_{MA}$ can be identified.

The recursive least squares (RLS) PAA for tuning the tap weights of H is [3]

$$\hat{\theta}(k) = \hat{\theta}(k-1) + P(k)\phi(k)e(k-1)\,, \tag{5.44}$$

$$P(k) = P(k-1) - \frac{P(k-1)\phi(k-1)\phi^T(k-1)P(k-1)}{1+\phi^T(k-1)P(k-1)\phi(k-1)} \tag{5.45}$$

Other simplified algorithms, such as the LMS algorithm, also can be used.

5.4.2 Microactuator Model Identification

The damped microactuator model can be estimated using the self-tuning control scheme presented in section 5.3. It is also possible to identify the microactuator model using an off-line identification scheme since the variations in the microactuator's resonance frequency are due to the fabrication processes, and usually do not change after the microactuator is fabricated.

The discrete-time transfer function of the microactuator model can be written as

$$G_{MA}(q^{-1}) = \frac{q^{-1}B_o(q^{-1})}{A_o(q^{-1})}\,, \tag{5.46}$$

where $B_o(q^{-1})$ and $A_o(q^{-1})$ are respectively the microactuator open-loop zero and pole polynomials:

$$B_o(q^{-1}) = b_0 + b_1 q^{-1}\,, \tag{5.47}$$

$$A_o(q^{-1}) = 1 + a_1 q^{-1} + a_2 q^{-1}\,. \tag{5.48}$$

Depending on the availability of the $RPES$ signal, different estimation schemes can be used to identify the model parameters. When the $RPES$ is available, the open-loop microactuator dynamics can be identified by feeding to the microactuator a white excitation

input signal. The parameters can be identified directly using the microactuator dynamics

$$A_o(q^{-1})y(k) = q^{-1}B_o(q^{-1})u_M(k) + w(k)\,, \tag{5.49}$$

where $u_M(k)$ is the input excitation signal to the microactuator, $y(k)$ is the $RPES$ and $w(k)$ is the $RPES$ measurement noise.

When the $RPES$ signal is not available and the only measurement is the PES, it is still possible to identify the microactuator open-loop dynamics by closing the VCM loop with the PES, and feeding an excitation input signal of sufficiently large magnitude to the microactuator, as shown in Fig. 5.13.

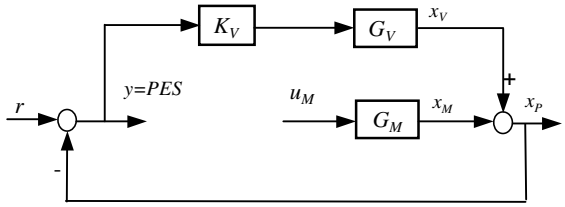

Figure 5.13: Microactuator model identification without $RPES$ sensing

Defining $y(k)$ to be the PES, we have

$$y(k) = r(k) - G_M u_M(k) - K_V G_V y(k)\,, \tag{5.50}$$

where r represents the runout, $u_M(k)$ is the input excitation signal to the microactuator, G_M and G_V are the transfer functions of the microactuator and the VCM, respectively. Defining the closed-loop sensitivity transfer function of the VCM,

$$S_V = \frac{1}{1 + K_V G_V}\,, \tag{5.51}$$

and defining the filtered excitation to the microactuator by

$$u_M^f(k) = -S_V\, u_M(k)\,, \tag{5.52}$$

we obtain,

$$y(k) = G_M\, u_M^f(k) + S_V r(k)\,. \tag{5.53}$$

In the above equation, the term $S_V r(k)$ represents the PES due to the runout after it has been rejected by the VCM sensitivity function. It is small as compared to the PES due to the excitation of the microactuator, since we choose u_M to be sufficiently large. Eq. (5.53) can be rewritten as

$$A_o(q^{-1})y(k) = q^{-1}B_o(q^{-1})u_M^f(k) + C(q^{-1})w(k)\,, \tag{5.54}$$

where A_o, B_o are the microactuator open-loop pole and zero polynomials, which need to be identified, $w(k)$ is a fictitious white noise, and $C(q^{-1})$ represents the combined effect of runout, VCM and microactuator torque disturbances, and the PES measurement noise, after being rejected by the VCM control loop.

Fig. 5.14 shows the simulated responses of the microactuator parameters estimates $\hat{a}_1$, $\hat{a}_2$, $\hat{b}_o$, $\hat{b}_1$, using the extended recursive least square (ERLS) algorithm [3]. Simulated runout, VCM and microactuator torque disturbances, PES measurement noise were injected into the dual-stage system in the simulations. The noise model $\hat{C}(q^{-1})$ was chosen to be fourth order. As shown in Fig. 5.14, the parameters estimates converged to their true values.

5.4.3 Simulation Results

Simulations were conducted to verify the proposed adaptive feedforward vibration compensation scheme. The MEMS microactuator dual-stage model and the feedback controller system presented in sections 5.1 and 5.2 are used in the simulations. The windage

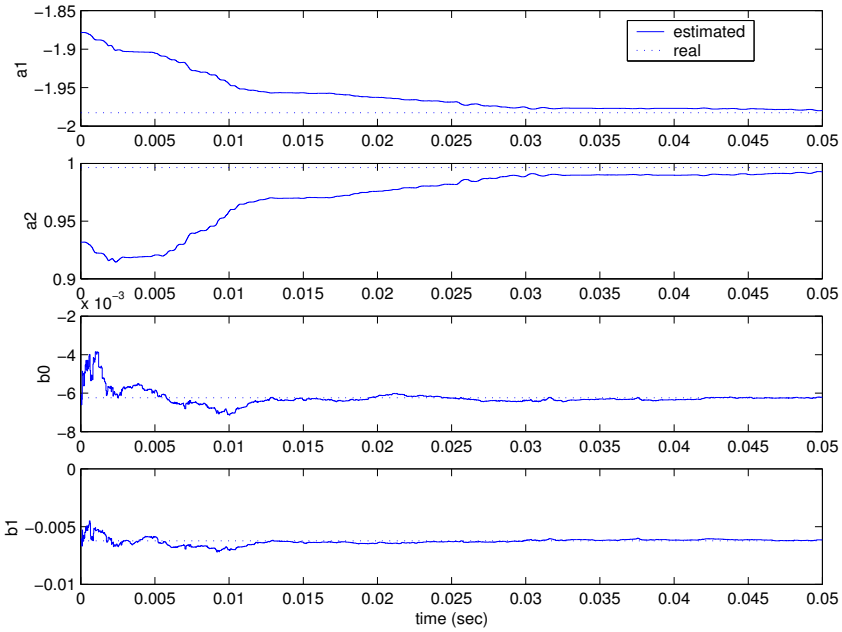

Figure 5.14: Control parameters adaptation responses

disturbance and vibration sensor models were estimated using the experimental data of the PZT-actuated suspension, as shown in Fig. 4.2.

A 6-tap FIR was used as the feedforward controller in the simulation. The feedforward control loop runs at 50 kHz, while the track-following control loop and the parameters adaptation loop run at 25 kHz. Fig. 5.15 shows the FFT of the simulated PES. The solid and dashed lines are when adaptive feedforward control is and is not applied, respectively. The PES is reduced by 36% when adaptive feedforward control is applied.

Fig. 5.16 shows the simulated adaptation of the FIR filter tap weights. Notice that the adaptation convergence is slow. This is because the error signal used in the adaptation is the PES, which is corrupted by the position error due to other sources. This can be improved by incorporating an additional plant and noise model identification PAA [46].

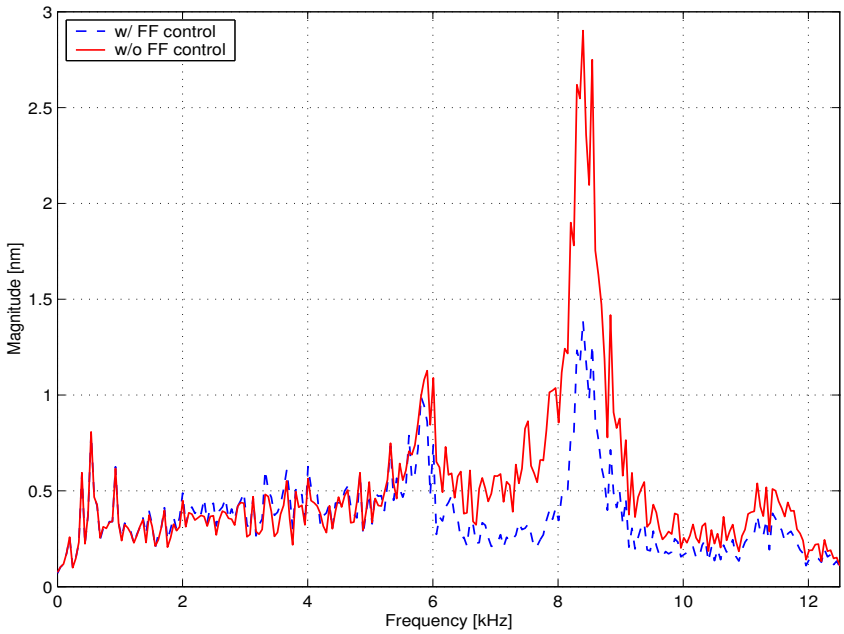

Figure 5.15: Simulation of feedforward vibration compensation.

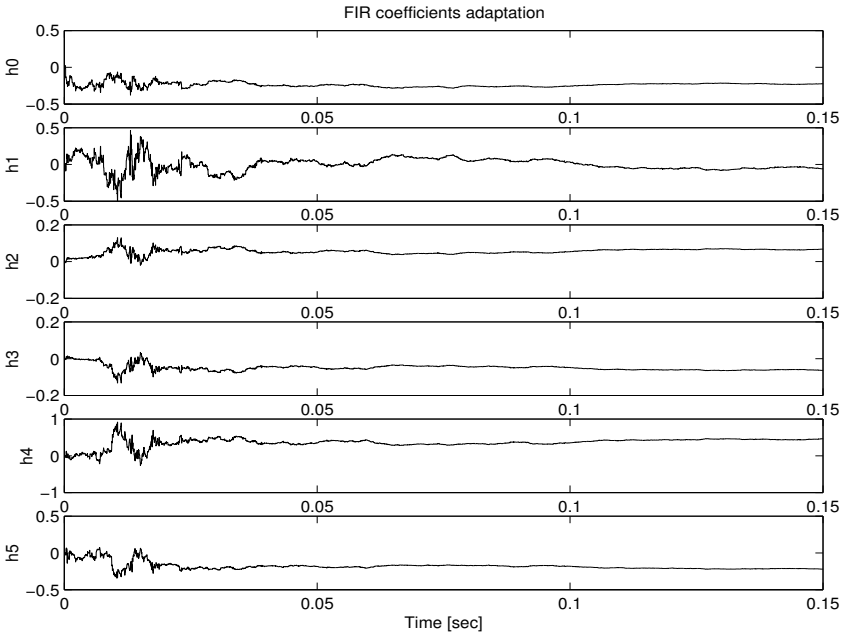

Figure 5.16: FIR tap weights adaptation.

Chapter 6

Conclusions

6.1 Conclusions

In this dissertation, robust and adaptive controller design methodologies and algorithms, and active vibration suppression control techniques were developed for dual-stage servo systems in hard disk drives.

In the control design of the PZT-actuated suspension dual-stage servo system, robust control design and analysis methodology using μ-synthesis was developed. A plant model including dynamic coupling effects of the dual-stage actuator was identified using modal testing. A structured uncertainty model was established to represent both parametric uncertainty and unmodeled dynamics of the dual-stage servo system. The use of μ-synthesis has been shown to be an effective method to design robust optimal dual-stage track-following controllers. Robustness of the controller designed using the popular decoupled master-slave method was also analyzed using μ. Even though the stability robustness is achieved for the decoupled design, there might be a large performance degradation under the worst-case

perturbation. The μ-synthesis design can achieve almost twice the stability margin of the decoupled design with only a small nominal performance degradation.

Active damping control of the resonance modes of the PZT-actuated suspension dual-stage actuator utilizing one PZT element as a vibration sensor was proposed. The vibration damping controller was designed using Kalman filter based state feedback damping control techniques. The effectiveness of the proposed control scheme in suppressing turbulence excited structural vibrations of the actuator and suspension assembly was experimentally demonstrated. The proposed active damping control technique for the PZT-actuated suspension dual-stage actuator overcomes the fundamental limitation in its dynamic response, and makes it a viable alternative high performance solution to dual-stage actuation in HDDs. Head off-track motion of less than 5 nanometers in 1-σ value has been achieved for track-following control with active damping in the experimental testing.

In the controller design of a MEMS microactuator dual-stage servo system, a decoupled design structure with microactuator minor-loop damping and a pole placement design methodology were proposed. The main advantage of the proposed scheme is that it can be combined with a self-tuning loop to compensate for the variations in the microactuator's resonance mode. A direct self-tuning control algorithm was developed and the convergence of control parameters was verified in the simulations. An adaptive feedforward control scheme was developed to cancel the head off-track motion caused by airflow excited suspension vibrations using the MEMS microactuator.

6.2 Future Work

A number of interesting topics related to the research in this dissertation remain to be explored in the control design of dual-stage multi-sensing servo systems in HDDs.

Mixed H_2/H_∞ Optimization

Disk drives are stochastic systems and their performance is represented by the statistical distribution of the PES. Thus, disk drive servo control is an H_2 optimal control problem in terms of achieving the best performance. On the other hand, disk drives are uncertain dynamic systems with both model parameters variations and unmodeled dynamics. The robust control problem is best formulated and solved using the H_∞ control theory. Robust optimal control of disk drive systems is a mixed H_2/H_∞ optimization problem, which has not fully been solved for MIMO output feedback systems. One possible solution to this problem is using linear matrix inequality (LMI) optimization techniques [7].

One topic of future work is to investigate how to formulate the robust and optimal dual-stage track-following control and vibration suppression control design problem as a multi-objective multi-constraint H_2/H_∞ optimization problem that can be solved using LMI techniques.

Simultaneous Sensing and Actuation using PZT Actuators

In this dissertation, a vibration damping control scheme using one PZT element as a sensor and the other as an actuator was proposed. There are two main disadvantages of this scheme. First, the actuator gain is reduced by half. Second, the sensor output signal is

corrupted by big contributions from the out-of-the-plane bending modes vibrations. If both PZT elements are used as sensors, the common-mode component due to bending modes vibrations can be rejected. As a result, the damping controller design can be simplified and the performance can be improved.

Thus, investigation of the feasibility of simultaneous sensing and actuation using both PZT elements is a very interesting research topic. One possible solution is to use a bridge-matching circuit to pick up the vibration sensing output signal [2].

Sensor Fabrication, System Integration and Control Testing

Adaptive feedforward vibration compensation using the MEMS microactuator was proposed in this dissertation. There remains a lot of work to be done in sensor fabrication and system integration to implement such a control scheme. MEMS microactuators and instrumented suspensions with piezoelectric thin-film vibration sensors are being designed and fabricated in our research group. New robust, adaptive MIMO control architectures and algorithms remain to be developed and tested for such a multi-sensing multi-actuation servo system.

Bibliography

[1] D. Abramovitch and G. Franklin. A brief history of disk drive control. *IEEE Control System Magazine*, 22:28–42, July 2002.

[2] E.H. Anderson and N.W. Hagood. Simultaneous piezoelectric sensing/actuation: analysis and application to controlled structures. *Journal of Sound and Vibration*, 174(5):617–39, July 1994.

[3] K. J. Åström and B. Wittenmark. *Adaptive Control*. Addison-Wesley, 2nd edition, 1995.

[4] K. J. Åström and B. Wittenmark. *Computer Controlled System*. Prentice-Hall, Inc, 3rd edition, 1997.

[5] G. J. Balas, J. C. Doyle, K. Glover, A. Packard, and R. Smith. *μ-Analysis and Synthesis Toolbox User's Guide*. MUSYN Inc. and The MathWorks, 1995.

[6] H.W. Bode. *Network Analysis and Feedback Amplifier Design*. Van Nostrand, New York, USA, 1945.

[7] S. Boyd, L. El Ghaoui, E. Feron, , and V. Balakrishnan. *Linear Matrix Inequalities in*

System and Control Theory. Society for Industrial and Applied Mathematics (SIAM), 1994.

[8] T.-L. Chen. *Ph.D. Dissertation: Design and Fabrication of PZT-Actuated Silicon Suspensions for Hard Disk Drives*. University of California, Berkeley, CA, USA, 2001.

[9] R.Y. Chiang and M.G. Safonov. *Robust Control Toolbox User's Guide*. MathWorks Inc., Natick, MA, USA, 1997.

[10] J. Doyle, K. Zhou, and K. Glover. *Robust and Optimal Control*. Prentice-Hall, Inc, 1996.

[11] R. Ehrlich and D. Curran. Major HDD TMR sources, and projected scaling with TPI. *IEEE Transactions on Magnetics*, 35:885–91, March 1999.

[12] D. Ewins. *Modal Testing: Theory, Pratice and Application*. Research Studies Press, Bladock, Hertfordshire, UK, 2nd edition, 2000.

[13] L.-S. Fan, T. Hirano, J. Hong, P. R. Webb, W.H. Juan, W. Y. Lee, S. Chan, T. Semba, W. Imaino, T.S. Pan, S. Pattanaik, F.C. Lee, I. McFadyen, S. Arya, and R. Wood. Electrostatic microactuator and design considerations for HDD application. *IEEE Transactions on Magnetics*, 35:1000–5, 1999.

[14] G.F. Franklin, J.D. Powell, and M. Workman. *Digital Control of Dynamic Systems*. Addison Wesley Longman, Inc, Menlo Park, CA, USA, 3rd edition, 1998.

[15] H. Fujita, K. Suzuki, M. Ataka, and S. Nakamura. A microactuator for head positioning system of hard disk drives. *IEEE Transactions on Magnetics*, 35:1006–10, March 1999.

[16] H. Gross. *Ph.D. Dissertation: Off-Track Vibrations of the Read-Write Heads in Hard Disk Drives*. University of California, Berkeley, CA, USA, 2003.

[17] L. Guo and Y.-J. Chen. Disk flutter and its impact on HDD servo performance. *IEEE Transactions on Magnetics*, 37:866–70, March 2001.

[18] D. Hernandez, S.-S. Park, R. Horowitz, and A.K. Packard. Dual-stage track-following servo design for hard disk drives. In *Proceedings of American Automatic Control Conference*, pages 4116–21, San Diego, California, USA, June 1999.

[19] T. Hirano, L.-S. Fan, T. Semba, W. Lee, J. Hong, S. Pattanaik, P. Webb, W.-H. Juan, and S. Chan. High-bandwidth HDD tracking servo by a moving-slider micro-actuator. *IEEE Transactions on Magnetics*, 35:3670–72, september 1999.

[20] T. Hirano, L.-S. Fan, T. Semba, W.Y. Lee, J. Hong, S. Pattanaik, P. Webb, W.-H. Juan, and S. Chan. Micro-actuator for tera-storage. In *IEEE Int'l MEMS 1999 Conference*, Jan. 1999.

[21] D. Horsley. *Ph.D. Dissertation: Microfabricated electrostatic actuators for magnetic disk drives*. University of California, Berkeley, CA, USA, 1998.

[22] D. Horsley, N. Wongkomet, R. Horowitz, and A. Pisano. Precision positioning using a microfabricated electrostatic actuator. *IEEE Transactions on Magnetics*, 35:993–99, 1999.

[23] T. Howell, R. Ehrlick, and M. Lippman. TPI growth is key to delaying superparamagnetism's arrival. *Data Storage*, pages 21–30, September 1999.

[24] X. Hu, W. Guo, T. Huang, and B.M. Chen. Discrete time LQG/LTR dual-stage controller design and implementation for high track density HDDs. In *Proceedings of American Automatic Control Conference*, pages 4111–15, San Diego, CA, USA, June 1999.

[25] M.Y. Huang, T. Semba, W. Imaino, and F. Lee. Active damping in HDD actuator. *IEEE Transactions on Magnetics*, 37:847–49, March 2001.

[26] Y. Huang, M. Banther, P. Mathur, and W. Messner. Design and analysis of a high bandwidth disk drive servo system using an instrumented suspension. *IEEE/ASME Transations on Mechatronics*, 4:196–206, June 1999.

[27] T. Imamura, M. Katayama, Y. Ikegawa, T. Ohwe, R. Koishi, and T. Koshikawa. MEMS-based integrated head/actuator/slider for hard disk drives. *IEEE/ASME Transansactions on Mechatronics*, 3:166–74, 1998.

[28] T. Imamura, T. Koshikawa, and M. Katayama. Transverse mode electrostatic microactuator for MEMS-based HDD slider. In *Proceedings of IEEE MEMS Workshop*, pages 216–21, San Diego, CA, USA, 1996.

[29] F. Jorgenson. *Complete Handbook of Magnetic Recording*. McGraw-Hill, 1995.

[30] B.-C. Kim and C.D. Mote. Suppressing turbulence induced vibration of the head suspension assembly in a hard disk drive. In *CML Technical Report*, number 99-015, University of California, Berkeley, USA, 1999.

[31] M. Kobayashi, T. Yamaguchi, T. Yoshida, and H. Hirai. Multi-sensing servo with

carriage-acceleration feedback for magnetic disk drives. In *Proceedings of American Automatic Control Conference*, pages 3038–42, Philadelphia, PA, USA, June 1998.

[32] S. Koganezawa, K. Takaishi, Y. Mizoshita, Y. Uematsu, , and T. Yamada. Development of integrated piggyback milli-actuator for high density magnetic recording. In *International Conference on Micromechatronics for Information and Precision Equipment*, pages 20–23, 1997.

[33] H. Kuwajima and K. Matsuoka. Thin film piezoelectric dual-stage actuator for HDD. In *InterMag Europe, Session BS04*, April 2002.

[34] S.-H. Lee, S.-E. Baek, and Y.-H. Kim. Design of a dual-stage actuator control system with discrete-time sliding mode for hard disk drives. In *Proceedings of the 39th IEEE Conference on Decision and Control*, pages 3120–25, December 2000.

[35] Y. Lou, P. Gao, B. Qin, G. Guo, E.-H. Ong, A. Takada, and K. Okada. Dual-stage servo with on-slider PZT microactuator for hard disk drives. In *InterMag Europe, Session BS03*, April 2002.

[36] J.S. McAllister. The effect of disk platter resonances on track misregistration in 3.5 inch disk drives. *IEEE Transactions on Magnetics*, 32:1762–66, May 1996.

[37] W. Messner and R. Ehrlich. A tutorial on controls for disk drives. In *Proceedings of American Automatic Control Conference*, pages 408–419, Arlinton, VA, USA, June 2001.

[38] D.K. Miu. *Mechatronics: Electromechanics and Contromechanics*. Springer-Verlag, Berlin, Germany, 1992.

[39] C. Mohtadi. Bode's integral theorem for discrete-time system. *Proceedings of IEE*, 137:57–66, March 1990.

[40] K. Mori, T. Munemoto, H. Otsuki, Y. Yamaguchi, and K. Akagi. A dual-stage magnetic disk drive actuator using a piezoelectric device for a high track density. *IEEE Transactions on Magnetics*, 27:5298–300, November 1991.

[41] MSI. *Piezo Film Sensor Technical Manual*. Measurement Specialties, Inc, Norristown, PA, USA, 1999.

[42] L. Muller. *Ph.D. Dissertation: Gimballed Electrostatic Microactuators with Embedded Interconnects*. University of California, Berkeley, CA, USA, 2000.

[43] S. Nakamura, K. Suzuki, M. Ataka, and H. Fujita. An electrostatic micro actuator for a magnetic head tracking system of hard disk drives. In *Transducers '97*, pages 1081–84, Chicago, IL, USA, June 1999.

[44] I. Naniwa, S. Nakamura, S. Saegusa, and K. Sato. Low voltage driven piggy-back actuator of hard disk drives. In *IEEE International MEMS 99 Conference*, pages 49–52, Orlando, FL, USA, 1999.

[45] A. Packard and J. Doyle. The complex structured signular value. *Automatica*, 29:71–109, 1993.

[46] S. Pannu. *Ph.D. Dissertation: Adaptive Servo Schemes using Micromachined Accelerometers for Increased Disturbance Rejection for Magnetic Hard Disk Drives*. University of California, Berkeley, CA, USA, 1998.

[47] S. Pannu and R. Horowitz. Increase disturbance rejection for hard disk drives using accelerometers. *Journal of Information Storage and Processing Systems*, 1:95–103, 1999.

[48] J.S. Griesbach R.B. Evans and W.C. Messner. Piezoelectric microactuator for dual-stage control. *IEEE Transactions on Magnetics*, 35:977–81, March 1999.

[49] M. Rotunno and R.A de Callafon. Fixed order H_∞ control design for dual-stage hard disk drives. In *Proceedings of the 39th IEEE Conference on Decision and Control*, pages 3118–19, Sydney, NSW, Australia, December 2000.

[50] M. Sasaki, T. Suzuki, E. Ida, F. Fujisawa, M. Kobayashi, and H. Hirai. Track-following control of a dual-stage hard disk drive using a neuro-control system. *Engineering Applications of Artificial Intelligence*, 11:707–16, 1998.

[51] S.J. Schroeck, W.C. Messner, and R.J. McNab. On compensator design for linear time-invariant dual-input single-output systems. *IEEE/ASME Transactions Mechatronics*, 6:50–57, March 2001.

[52] T. Semba, T. Hirano, and L.-S. Fan. Dual-stage servo controller for HDD using MEMS actuator. *IEEE Transactions on Magnatics*, 35:2271–73, September 1999.

[53] Y. Soeno, S. Ichikawa, T. Tsuna, Y. Sato, and I. Sato. Piezoelectric piggy-back microactuator for hard disk drive. *IEEE Transactions on Magnetics*, 35:983–87, March 1999.

[54] S.-M. Suh, C.C. Chung, and S.-H. Lee. Design and analysis of dual-stage servo system for high track density HDDs. *Microsystem Technologies*, 8:161–68, 2002.

[55] T. Suzuki, T. Usui, M. Sasaki, F. Fujisawa, T. Yoshida, and H. Hirai. Comparison of robust track-following control systems for a dual stage hard disk drive. In *Proceedings of International Conference on Micromechatronics for Information and Precision Equipment*, pages 101–18, Tokyo, Japan, July 1997.

[56] M. Tomizuka. Zero phase error tracking algorithm for digital control. *Transactions of ASME, Journal of Dynamical Systems, Measurements, and Control*, 109:65–68, May 1987.

[57] M. T. Whilte and W.-M. Lu. Hard disk drive bandwidth limitations due to sampling frequency and computational delay. In *Proceedings of the 1999 IEEE/ASME International Conference on Intelligent Mechatronics*, pages 120–25, September 1999.

[58] M. White. *Ph.D. Dissertation: Control Techniques for Increased Disturbance Rejection and Tracking Accuracy in Magnetic Disk Drives.* University of California, Berkeley, CA, USA, 1997.

[59] M.T. White and M. Tomizuka. Increased disturbance rejection in magnetic disk drives by acceleration feedfoward control. In *Proceedings of the 13th World Congress of IFAC*, pages 489–494, San Francisco, CA, USA, July 1996.

[60] N. Wongkomet. *Ph.D. Dissertation: Position Sensing for Electrostatic Micropositioners.* University of California, Berkeley, CA, USA, 1998.

[61] T. Yamaguchi. Modelling and control of a disk file head-positioning system. *Proceedings of the Institution of Mechanical Engineers, Part I (Journal of Systems and Control Engineering)*, 215:549–567, 2001.

[62] Y. Yamaguchi, K. Takahashi, H. Fujita, and K. Kuwahara. Flow induced vibration of magnetic head suspension in hard disk drive. *IEEE Transactions on Magnetics*, 22(5):1022–24, 1986.

[63] J.Y. Yen, K. Hallamasek, and R. Horowitz. Track following controller design for a compound disk drive actuator. *Transactions of ASME, Journal of Dynamical Systems, Measurements, and Control*, 112(3):391–402, September 1990.

[64] K. Zhou and J. Doyle. *Essentials of Robust Control*. Prentice-Hall, Inc, 1998.